Ludwig-Maximilians University Munich
Faculty of Physics

Master thesis

Search for Scalar Top Quarks in Final States with Two Hadronically Decaying Tau Leptons

(Suche nach skalaren Top-Quarks in Endzuständen mit zwei hadronisch zerfallenden Tau-Leptonen)

Author: Ferdinand Krieter
Supervisor: Prof. Dr. Dorothee Schaile

Munich, May 12, 2017

Abstract

Supersymmetry can resolve several shortcomings of the Standard Model, one of them being the hierarchy problem. Due to its large contribution to radiative corrections of the Higgs boson mass, the top squark, the supersymmetric partner of the top quark, is expected to be relatively light and thus within the reach of the LHC. A search for direct pair production of top squarks in final states with two tau leptons, b-jets and missing transverse momentum is presented. The analysis uses $36.1\,\mathrm{fb}^{-1}$ of proton-proton collision data at a center of mass energy of $\sqrt{s} = 13\,\mathrm{TeV}$, recorded with the ATLAS detector at the LHC in 2015 and 2016. The investigated class of simplified signal models considers top squarks decaying exclusively via a three-body decay into a neutrino, a b-quark and a scalar tau lepton. The latter is then assumed to decay into a tau lepton and a gravitino, which represents the lightest supersymmetric particle in this model. Top squark candidates are searched for in events where both tau leptons decay hadronically and no light leptons are present. The signal region is optimized for signal models considering scalar taus that are relatively light compared to the top squarks. Background contributions are estimated using Monte Carlo and semi-data-driven methods. As the signal region is still blinded, two possible results are discussed: In case a significant excess in data is observed discovery significance for top squark masses up to approximately 850 GeV can be reached. In the absence of signal the exclusion limits already set by previous analyses are expected to be pushed up top squark masses of about 1 GeV. The unblinded results are aimed to be presented in combination with those of the analyses considering also leptonically decaying taus.

Zusammenfassung

Supersymmetrie kann zahlreiche Defizite des Standardmodells, wie das Hierarchieproblem, beheben. Aufgrund seiner hohen Beträge zu den Strahlungskorrekturen der Higgsmasse erwartet man, dass das Top-Squark, das supersymmetrische Partnerteilchen des Top-Quarks, relativ leicht ist und somit in der Reichweite des LHCs liegt. Es wird eine Suche nach direkter Paarproduktion von Top-Squarks in Endzuständen mit zwei Tau-Leptonen, b-Jets und fehlender transversaler Energie vorgestellt. Die Analyse gebraucht Daten aus Proton-Proton-Kollisionen bei einer Schwerpunktsenergie von $\sqrt{s} = 13\,\text{TeV}$, welche mit dem ATLAS Detektor in den Jahren 2015 und 2016 aufgezeichnet wurden und einer integrierten Luminosität von $36.1\,\text{fb}^{-1}$ entsprechen. Die untersuchte Klasse vereinfachter Signalmodelle betrachtet Top-Squarks, welche ausschließlich über einen Dreiköperzerfall zu einem Neutrino, einem b-Quark und einem skalaren Tau-Lepton zerfallen. Von letzterem wird dabei angenommen, dass es anschließend in ein Tau-Lepton und ein Gravitino, das leichteste supersymmetrische Teilchen in diesem Model, zerfällt. Es werden Ereignisse, in denen beide Tau-Leptonen hadronisch zerfallen und keine weiteren leichten Leptonen anwesend sind, nach Kandidaten für Top-Squarks untersucht. Die Signalregion ist für Modelle optimiert in denen das skalare Tau-Lepton, verglichen mit dem Top-Squark, relativ leicht ist. Untergrundbeiträge werden mittels Monte-Carlo-Simulationen und mit Hilfe echter Daten abgeschätzt. Da die Signalregion noch verblindet ist werden zwei mögliche Ausgänge behandelt: Falls ein signifikanter Datenüberschuss beobachtet werden sollte, so kann ein Signifikanzniveau mit Entdeckungspotential für Top-Squarkmassen von bis etwa 850 GeV erreicht werden. In Abwesenheit eines Signals wäre es möglich die bereits durch vorherige Analysen ermittelten Ausschlussgrenzen zu erweitern bis einschließlich Top-Squarkmassen von etwa 1 TeV. Ziel ist es die unverblindeten Ergebnisse in Kombination mit denen der anderen Analysen, welche leptonisch zefallende Tau-Leptonen miteinbeziehen, zu präsentieren.

Contents

1 Introduction

The successful history of finding experimental evidence for the fundamental building blocks of nature reached another milestone with the discovery of a Higgs boson in 2012. It was hence the last undiscovered particle predicted by the Standard Model of particle physics. In the second run of the Large Hadron Collider (LHC) the goal was set to not only enhance the precision of existing measurements but to explore possible extensions of the Standard Model. Although it provides an excellent description of the fundamental particles and their interactions, it leaves several questions unanswered. Why is gravity so weak compared to the other three fundamental forces? How can one explain the huge discrepancy between the visible and the gravitationally interacting mass at astronomical length scales? The unification of the electromagnetic and weak force at the electroweak scale motivates furthermore the conjecture that a unification with the other fundamental interactions might be possible at even higher energy scales. The resulting theory would possibly allow for a simultaneous, all-encompassing description of all fundamental particles and interactions — the ultimate but also ambitious dream of natural science ever since.

> *"Based only on a proper respect for the power of Nature to surprise us, it seems nearly as obvious that new physics exists in the 16 orders of magnitude in energy between the presently explored territory near the electroweak scale and the Planck scale."*
>
> – Stephen P. Martin [1]

A promising step in this direction involves the introduction of a new symmetry, which relates spacetime and internal degrees of freedom with one another: Supersymmetry postulates the existence of a bosonic or fermionic mirror image for each fermion and boson, respectively. Spontaneous breaking of this symmetry allows these new particles to have a mass that is not identical with that of their Standard Model partners. Motivated by the strong coupling to the Higgs field, the top squark, the supersymmmetric partner of the top quark, might nonetheless be sufficiently light to be within the grasp of the LHC, which now collides protons with a center of mass energy of 13 TeV.

This thesis is dedicated to the search of exactly such a top squark. Therefore, data recorded with the ATLAS detector at the LHC in 2015 and 2016 is analyzed. The results are interpreted using simplified models of Supersymmetry.

The thesis begins with a motivation and a general introduction of the principles of Supersymmetry, targeted for readers familiar with essentials of the Standard Model. Followed by a description of the experimental setup and structure of the analyzed data,

the main part focuses on the various methods for extracting events with potential top squark pair production from the recorded data.

2 Theory

The Standard Model (SM), extended with neutrino masses, provides a consistent, renormalizable quantum field theory of the fundamental interactions and has been confirmed by experimental data to high precision. However it also features a series of shortcomings and is generally incomplete as it fails to include a quantum description of gravity. One possible next step towards a unified 'theory of everything' might be given by a proposed fundamental symmetry relating boson to fermions and vice versa.

A few illustrations how this so-called supersymmetry (SUSY) can fix the inherent limitations of the SM are given in section 2.1. Section 2.2 aims to give a summary of the core features and mathematical implementation of SUSY. The particular SUSY model studied in this thesis is laid out in section 2.3.

2.1 Motivation

By introducing bosonic and fermionic superpartners to the known fermions and bosons, respectively, SUSY naturally solves many of the most urgent open questions in particle physics. Three examples for this are briefly reviewed in the following.

2.1.1 The Hierarchy and Fine-Tuning Problem

At the energy (or length) scales probed by today's collider experiments gravity does not play any role and so it is comprehensible to not include it in the framework of the SM. Nevertheless this is about to change near the Planck scale, defined by $m_{\mathrm{P}} = \sqrt{\hbar c/G} \approx 10^{19}\,\mathrm{GeV}$, where gravity and the other forces are expected to become alike in their strength. Thus a new, more complete theory that includes a description of quantum gravity is required at this scale. A similar phenomenon is observed for the electromagnetic and weak force, which become unified at the electroweak scale at $\sim 100\,\mathrm{GeV}$. This large discrepancy of the order of $10^{17}\,\mathrm{GeV}$ between the Planck scale and the electroweak scale is denoted as the hierarchy problem.

The origin of electroweak symmetry breaking is due to the W and Z bosons acquiring mass through the Higgs mechanism. The mass of the scalar Higgs boson is especially prone to quantum corrections as opposed to fermions or gauge bosons, which are largely protected by chiral or local gauge invariance, respectively. Figure 2.1 shows an example for second order virtual loop corrections to the Higgs propagator. Unitarity demands

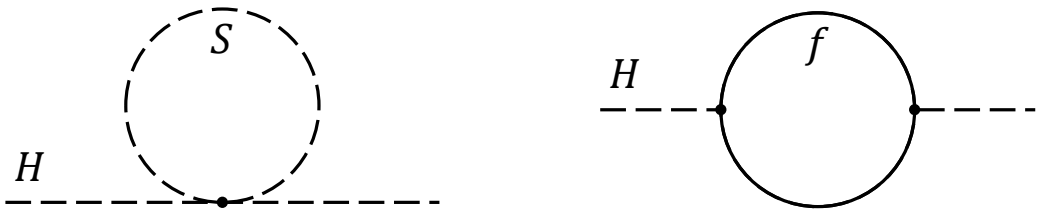

Figure 2.1: Second order radiative corrections to the Higgs boson propagator for a boson loop (left) and a fermion loop (right).

to consider all possible corrections and add their contributions. A loop containing a Dirac fermion of mass m_f modifies the Higgs boson mass by

$$\Delta m_H = -\frac{|\lambda_f|^2}{8\pi^2}\,\lambda_{UV}^2 + \dots \tag{2.1}$$

with $\lambda_f \sim m_f$ the coupling strength to the fermion and λ_{UV} the ultraviolet momentum cutoff used in the regularization scheme [1]. This cutoff scale should be interpreted as a lower bound on the energy scale at which new physics are expected to enter. The cutoff scale is then at the order of the Planck scale, if one assumes the SM to remain valid up to this energy scale. A scalar boson loop gives the following correction to the Higgs boson mass:

$$\Delta m_H = \frac{\lambda_S}{16\pi^2}\,\lambda_{UV}^2 + \dots\,, \tag{2.2}$$

where λ_S is the coupling strength to the scalar field [1]. In both cases the magnitude of the corrections to the Higgs mass is given by the cutoff scale $\lambda_{UV}^2 \sim (10^{19}\,\mathrm{GeV})^2$. However, the scalar boson discovered at the Large Hadron Collider in 2012, which qualifies as a Higgs particle, has been measured to have a mass of only 125 GeV [2]. It would then require an unnatural amount of manual 'fine-tuning' to adjust all initial parameters of the theory as functions of the cutoff to retain the observed Higgs boson mass.

A very pleasing way to resolve this fine-tuning problem is presented by SUSY: As fermionic and bosonic loops contribute with opposite sign, these correction terms would cancel each other naturally independent of the cutoff scale and as a result the Higgs mass would be stable.

2.1.2 Dark Matter

Further evidence showing that the particle content of the SM does not suffice a complete description of nature is given by astrophysical observations.

The distribution of visible matter in a galaxy can be derived from the relative brightness across it. For spiral galaxies it is observed that most of their luminous matter is concentrated in the central region, or bulge. Via spectral analysis the Doppler shift and consequently the rotational velocities across the disc of a spiral galaxy can be deduced. When plotted versus the distance r to the center of the galaxy, the tangential velocity is expected have a $1/\sqrt{r}$ dependence according to Kepler's laws of motion. However, such a behavior is not observed. Instead the tangential velocity seems to take a constant value after a certain distance from the galaxy's center, indicating the presence of a huge amount of non-luminous 'dark matter' [3]. To fit the observed motion of the galaxy's disc this additional dark matter is postulated to be distributed across the halo, the sphere surrounding the galaxy.

Another evidence for the presence of dark matter stems from gravitational lensing effects. Light emitted from a distant source located behind a cluster of galaxies for example is deflected as it travels towards the observer: The mass of the galaxy cluster causes the spacetime to curve forcing the photons to travel on non-straight geodesics. If all three objects are aligned, then the light source, e. g. a galaxy, appears as a distorted image of itself, often in the shape of arcs or rings around the galaxy cluster in the foreground. It is observed that the mass of the visible luminous matter of the cluster alone cannot account for the lensing effects [4].

Dark matter does not emit or interact with electromagnetic radiation nor does it couple via the strong interaction. The SM offers only neutrinos as a possible candidate. However, due to their low masses and thus relativistic character, neutrinos are unlikely to be capable of forming the dense dark matter structures suggested by astrophysical observations and simulations. In the Lambda-CDM (cold dark matter) model [5], it is therefore assumed that dark matter is composed mainly of so far undiscovered weakly interacting massive particles (WIMPs). Many SUSY models naturally provide a dark matter candidate in the form of an electrically neutral and colorless, stable supersymmetric particle, as will be discussed in section 2.2.2.

2.1.3 Unification of Coupling Constants

The unification of the electromagnetic and weak force raised the question whether the same can be achieved also with the strong force. The long sought-after idea of a Grand Unified Theory (GUT) combining all three fundamental gauge interactions is characterized by one universal coupling constant. The strength of the electromagnetic, weak and strong interaction, given by their respective coupling constants, depends on the squared momentum transfer in the interaction. Indeed their energy dependence, the so-called 'running' of the coupling constants, leads to a scale where all three eventually come quite close. However, in the SM they do not meet precisely at the same point as shown in the left plot in figure 2.2. If instead the minimal supersymmetric extension of the SM is used, the coupling constants do converge in a single point naturally. The corresponding energy scale at $\sim 10^{16}$ GeV is however still far beyond the reach of todays

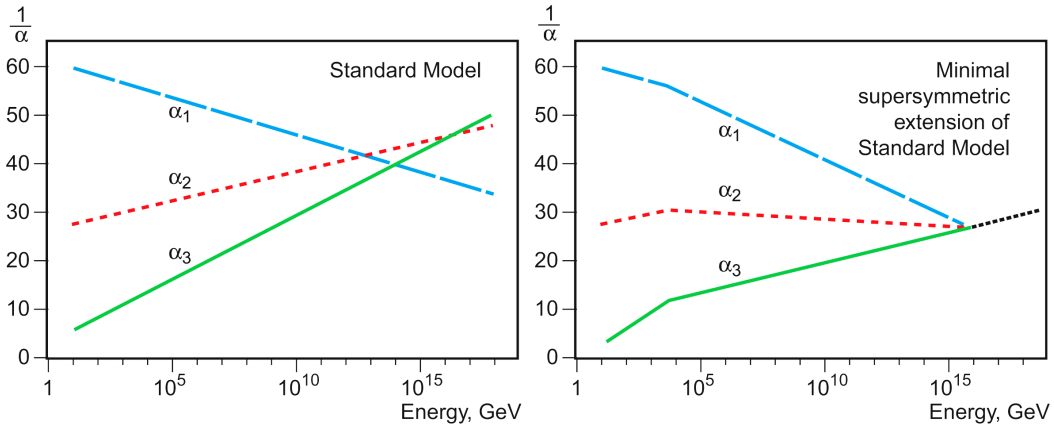

Figure 2.2: Running of the gauge couplings in the SM (left) and the minimal supersymmetric extension of the SM (right) [6]. Here α_1, α_2 and α_3 denote the coupling constants of the $U(1)_Y$, $SU(2)_L$ and $SU(3)_C$ gauge group, respectively.

collider experiments.

2.2 The Principle of Supersymmetry

This section aims to convey basic understanding of the mathematical implementation of SUSY, the particle content of the Minimal Supersymmetric SM (MSSM) , R-parity and its consequences and the mechanism of SUSY breaking. It follows therefore closely the pedagogical introductions provided by Stephen P. Martin [1] and Mauricio Bustamante et al [7]. Further instructive references include [8, 9, 10].

SUSY does not differentiate between fermions, the constituents of matter, and bosons, the mediators of the fundamental interactions. With respect to the SM the particle content is then (more than) doubled, as each known particle is associated with a supersymmetric partner, which differs in spin by 1/2.

Consider a fermionic operator Q as the generator for SUSY transformations:

$$Q\,|\text{fermion}\rangle = |\text{boson}\rangle\,, \quad Q\,|\text{boson}\rangle = |\text{fermion}\rangle\,, \tag{2.3}$$

with the spinor Q and its hermitian conjugate $\bar{Q}$, taken in the Weyl representation[1]. While it is in principle possible to introduce more generators, only the approach with one generator is considered here. This is called $N = 1$ SUSY and presents the only direct extension of the SM with phenomenological relevance [9].

[1]Weyl spinors have two components and represent particles of spin 1/2. The component with left (right) chirality is denoted by ψ_α ($\bar{\psi}^{\dot{\alpha}}$) with $\alpha \in \{1, 2\}$. The matrix $\epsilon_{\alpha\beta} = \epsilon_{\dot{\alpha}\dot{\beta}} = i\sigma_2$ and $\epsilon^{\alpha\beta} = \epsilon^{\dot{\alpha}\dot{\beta}} = -i\sigma_2$ can be used to raise and lower the spinorial indices.

The SUSY algebra can be summarized with the following (anti-)commutation relations [7, 8]:

$$[Q_\alpha, P^\mu] = 0\,, \qquad [\bar{Q}^{\dot{\alpha}}, P^\mu] = 0\,, \tag{2.4}$$

$$[Q_\alpha, M^{\mu\nu}] = i(\sigma^{\mu\nu})_\alpha{}^\beta Q_\beta\,, \qquad [\bar{Q}_{\dot{\alpha}}, M^{\mu\nu}] = i(\sigma^{\mu\nu})^{\dot{\alpha}}{}_{\dot{\beta}} \bar{Q}^{\dot{\beta}}\,, \tag{2.5}$$

$$\{Q_\alpha, Q_\beta\} = 0\,, \qquad \{\bar{Q}^{\dot{\alpha}}, \bar{Q}^{\dot{\beta}}\} = 0\,, \tag{2.6}$$

$$\{Q_\alpha, \bar{Q}_{\dot{\beta}}\} = 2\,(\sigma^\mu)_{\alpha\dot{\beta}} P_\mu\,, \tag{2.7}$$

where P^μ denotes the generator for spacetime translations and $M^{\mu\nu}$ the generator for Lorentz transformations, with $\mu, \nu \in \{0, 1, 2, 3\}$. The Minkowski metric is defined as $\eta_{\mu\nu} = \mathrm{diag}(+, -, -, -)$ while $\sigma^\mu = (\mathbb{1}_2, \sigma^i)$ and $\bar{\sigma}^\mu = (\mathbb{1}_2, -\sigma^i)$ with $i \in \{1, 2, 3\}$ contain the Pauli matrices and $\sigma^{\mu\nu} = \frac{i}{4}[\gamma^\mu, \gamma^\nu]$ with the Dirac matrices γ^μ taken in the Weyl basis.

From equation 2.4 it follows that also the squared mass operator $P^2 = P^\mu P_\mu$ commutes with Q, implying that superpartners must have the same mass. This is however not observed and thus SUSY has to be a broken symmetry such that superpartners acquire more mass than the SM particles. Possible realizations of SUSY breaking are explored in section 2.2.3. Equation 2.5 simply means that Q transforms as a spinor under spacetime rotations and that SUSY transformations are global, i. e. independent of the position in spacetime. Furthermore it can be shown that Q also commutes with the generators of gauge transformations. Thus all quantum numbers of the superpartners, with the exception of spin, match those of the associated SM particles [1].

Maybe the most striking statement is implied by equation 2.7: The anticommutator of a SUSY generator and its hermitian conjugate connects to a local coordinate translation. Therefore, if SUSY is promoted to a local symmetry, it naturally unifies the spacetime symmetry of general relativity with local SUSY transformations [11]. The resulting locally supersymmetric theory is called supergravity.

SUSY is thus not only an internal symmetry of bosons and fermions but is also inherently related to the isometries of Minkowski spacetime represented by the Poincaré group. By adjoining the anticommuting, fermionic SUSY generator to the generators of translation and Lorentz transformations, as shown above, Haag, Lopuszański and Sohnius showed that this gives the most general (but non-trivial) extension of the Poincaré algebra [12]. This relation can only be achieved with fermionic SUSY generators, as a bosonic ones are excluded by the fundamental Coleman-Mandula theorem [13].

An extension of the SM, which introduces the least amount of new SUSY particles, is outlined in section 2.2.1. The notion of R-parity and possible mechanisms for SUSY breaking are discussed in section 2.2.2 and 2.2.3, respectively.

2.2.1 Particle Content of the Minimal Supersymmetric Standard Model (MSSM)

The MSSM is the supersymmetric extension of the SM containing the minimal set of new particles and interactions consistent with phenomenology [9]. A representation of the SUSY algebra is given by supermultiplets combining fermion and boson states with the same quantum numbers apart from spin. In each supermultiplet the number of fermionic degrees of freedom must be equal to the number of bosonic ones.

In the MSSM all gauge bosons and gauge eigenstates of the fermions reside in such supermultiplets. The simplest realization is via chiral and gauge supermultiplets: A chiral supermultiplet contains a Weyl fermion of spin 1/2 and its superpartner (**s**fermion) represented by a complex scalar field (spin 0). A massless spin 1 gauge boson together with its spin-1/2 superpartner (gaug**ino**) forms a gauge supermultiplet.

From this it is clear that the scalar Higgs field has to be integrated into a chiral supermultiplet. To avoid gauge anomalies and provide all particles (except the Higgs bosons) with a possibility to become massive at least two chiral Higgs supermultiplets and thus two complex weak isospin doublets $H_u = (H_u^+, H_u^0)$ and $H_d = (H_d^0, H_d^-)$ with weak hypercharge $Y = +1/2$ and $-1/2$, respectively, are required [1]. The superscripts of the individual weak isospin components ($T_3 = \pm 1/2$) indicate their electrical charge[2].

In the following some general remarks are given along with a short overview, showing how the superpartners of the SM gauge eigenstates mix to form the mass eigenstates of the MSSM [1, 14, 15]:

- Left- and right-handed fermions have different scalar superpartners. The interaction of sfermions with the gauge bosons must be the same as for SM fermions. The superpartner of left-handed up-quark $\tilde{u}_L$ couples to the W boson, while the superpartner of the right-handed up-quark $\tilde{u}_R$ does not. Note that $\tilde{u}_L$ and $\tilde{u}_R$ do not exhibit chirality as they are scalars.
- In analogy to the SM, where the gauge bosons W^0 and B^0 mix to Z and γ via electroweak symmetry breaking, the corresponding gauginos (winos, bino) mix to 'zino' $\tilde{Z}$ and 'photino' $\tilde{\gamma}$.
- H_u can couple only to up-type quarks, while H_d only couples to down-type quarks. The two complex Higgs doublets have in total eight degrees of freedom, three of them are absorbed by the weak gauge bosons making them massive. This leaves five degrees of freedom that appear as physical particles:
  - h^0, H^0: One light and one heavy, neutral, CP-even Higgs, respectively. The former is usually identified with the SM Higgs boson.
  - A^0: A neutral, CP-odd Higgs.
  - H^+, H^-: Two oppositely charged Higgs bosons.

[2] Confer Gell-Mann-Nishijima formula: $Q = T_3 + Y$

- The superpartners of the Higgs bosons, the Higgsinos, will mix with the neutral zino and photino or with the charged winos to form mass eigenstates called neutralinos $\tilde{\chi}_i^0$ or charginos $\tilde{\chi}_j^{\pm}$, respectively, with $i \in \{1,2,3,4\}$ and $j \in \{1,2\}$ ranking them with respect to their mass from light to heavy.
- Color conservation prevents gluinos, the superpartners of the gluons, from mixing with higgsninos and the other gauginos, although they can aquire mass via SUSY breaking (see section 2.2.3).
- In principle, any sfermions with the same electric charge, R-parity (see section 2.2.2), and color can mix with each other to form a mass eigenstate. However, many SUSY models predict the third-generation squarks and sleptons to have substantial mixing angles with the superpartner of their chiral counterpart [1], e. g. $\tilde{t}_L$ and $\tilde{t}_R$ will mix to form two stop mass eigenstates. Likewise the superpartners of the charged left- and right-handed tau, $\tilde{\tau}_L$ and $\tilde{\tau}_R$, mix to form two stau mass eigenstates. The lighter of the two eigenstates is denoted as $\tilde{t}_1$ or $\tilde{\tau}_1$, respectively.

As mentioned before gravity can be included into the MSSM by making the SUSY generator local. The gravitino, the hypothesized massless, spin 2 mediator of the gravitational force, together with its spin 3/2 superpartner, the gravitino, are then resembled in a gravity supermultiplet. If SUSY is not broken, the graviton and the gravitino are both massless, each with two spin helicity states.

2.2.2 R-Parity

In the SM processes the baryon number B and lepton number L are conserved. Within the SM the proton, being the lightest baryon, is thus stable, which has been experimentally verified to high precision [16, 17, 18]. By introducing SUSY new interaction vertices can occur, which would allow for the proton to decay.

To guarantee baryon and lepton number conservation within the MSSM a new conserved, multiplicative quantum number, called R-parity, is introduced:

$$R = (-1)^{3(B-L)+2S} = \begin{cases} +1 & \text{for SM particles} \\ -1 & \text{for SUSY particles} \end{cases} \tag{2.8}$$

where S is the spin and $B = \frac{1}{3}(N_q - N_{\bar{q}})$, with N_q ($N_{\bar{q}}$) the number of (anti-)quarks or (anti-)squarks, and $L = N_\ell - N_{\bar{\ell}}$, with N_ℓ ($N_{\bar{\ell}}$) the number of (anti-)leptons or (anti-)sleptons.

The conservation of R-parity implies that the decay products of a supersymmetric particle must contain an odd number of supersymmetric particles and that the lightest one (LSP) has to be stable. An uncharged, colorless, massive LSP, would consequently serve as an excellent candidate for dark matter [19]. Furthermore, since the final state

must have even R-parity like the initial state, colliders can produce supersymmetric particles only in pairs.

2.2.3 The Mechanism of SUSY Breaking

From observations it is clear that the SM particles are not degenerate with their superpartners. SUSY must therefor be a broken symmetry. To preserve its features SUSY must be spontaneously broken, rather than explicitly, meaning that the underlying Lagrangian density is supersymmetric but the vacuum state is not [20]. In addition the breaking is desired to be 'soft', which means that it should not spoil the renormalizabilility of the theory. A consequence of the spontaneous SUSY breaking is the existence of a massless Goldstone fermion, the goldstino, which is absorbed by the gravitino if SUSY is defined to be local. The gravitino then becomes massive with two transverse (helicity $\pm 3/2$) and two longitudinal (helicity $\pm 1/2$) modes. Moreover it inherits the non-gravitational interactions of the goldstino and thus the longitudinal modes of the gravitino can be of relevance in collider experiments [1].

Nevertheless the mechanism for spontaneous SUSY breaking is not yet fully understood. It is postulated that SUSY breaking occurs in some 'hidden' sector and is then mediated via messenger fields to the 'visible' sector containing all MSSM particles. Different approaches exist to descibe the interaction between these two sectors. Two of the most extensively studied mechanisms are:

- **Gauge-mediated symmetry breaking** [21]**:** Here the ordinary gauge fields of the SM couple to the messenger fields propagating SUSY breaking to the visible sector. The gravitino is then very light and often takes the role of the LSP.
- **Gravity-mediated symmetry breaking** [22]**:** In scenarios where gravity meditates SUSY breaking the gravitino usually has a large mass and is thus of little relevance for collider experiments. In many of these models the LSP is then the neutralino $\tilde{\chi}_1^0$.

2.3 Investigated Signal Model

The search for SUSY presented in this thesis studies a class of R-parity conserving MSSM models motivated by gauge mediated SUSY breaking. In particular the benchmark model features natural gauge mediation, specifically targeting the fine-tuning problem described in section 2.1.1 [23]. This requires that the superpartners of the third generation SM fermions are sufficiently light to allow for a natural stabilization of the Higgs mass.

The light top squark (stop) $\tilde{t}_1$ is assumed to be pair-produced via the strong interaction in the proton-proton collisions and subsequently decays via an off-shell chargino $\tilde{\chi}_1^{\pm}$ to a b-quark, a tau neutrino ν_τ and a light tau slepton (stau) $\widetilde{\tau}_1$. The stau then decays

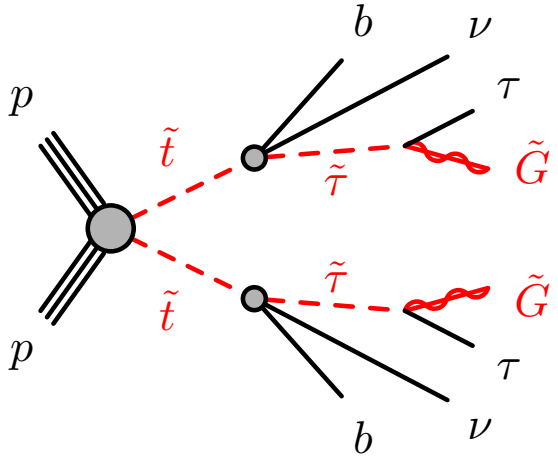

Figure 2.3: The simplified signal model targeted by the analysis presented in this thesis.

into its SM partner, the tau lepton, and a gravitino $\tilde{G}$, which is assumed to be nearly massless, hence making it the LSP in this scenario. In the following indices labeling the mass eigenstates of a SUSY particle are sometimes neglected, as only the lightest one is considered.

Figure 2.3 shows the corresponding simplified Feynman diagram. The off-shell decay of the stop via the assumed to be much heavier chargino is modeled as an effective three-body decay. Furthermore, all other SUSY particles are assumed to be too massive to be relevant for the observable kinematics. As an additional simplification all decays in figure 2.3 are assumed to have a branching ratio of 100%.

The search for top squark pair production in this benchmark scenario can be divided with respect to the decay mode of the tau:

- Both taus decay hadronically (had-had channel). The analysis presented in this thesis focuses only on this decay mode.
- One leptonically and one hadronically decaying tau (lep-had channel). A dedicated analysis targeting this final state is currently being performed in parallel.
- Both tau decay leptonically (lep-lep channel). No dedicated search is ongoing, but the possibility of reinterpreting the results of a different top squark search in ATLAS with a similar final state is currently evaluated.

The signal model features two free parameters: $m_{\tilde{t}}$ and $m_{\tilde{\tau}}$, the masses of the stop and stau, respectively. The analysis uses signal samples which have been generated using Monte Carlo simulation (see section 4.2) for a range of different combinations of discrete values (e. g. in steps of 50 GeV) of $m_{\tilde{t}}$ and $m_{\tilde{\tau}}$. Details on the analysis strategy are given in chapter 4. No samples are generated for combinations excluded by previous searches: A lower limit of 87 GeV has been set on the mass of the stau by the LEP

experiment [24]. The analysis of the lep-had channel with $13.2\,\mathrm{fb}^{-1}$ of proton-proton collision data at a center of mass energy of 13 TeV, recorded with the ATLAS detector at the LHC, excluded masses of the stop up to 870 GeV and of the stau up to 730 GeV [25].

SUSY models with gravity-mediated symmetry breaking and the neutralino $\tilde{\chi}_1^0$ as LSP would suggest a high branching ratio of $\tilde{t}_1 \to t\,\tilde{\chi}_1^0$. Searches for top squark pair production in SUSY models of this kind have been studied elsewhere [26, 27, 28, 29, 30, 31].

3 Experimental Setup

The European Organization for Nuclear Research (CERN) has been host to a variety of pioneering high energy physics experiments since its foundation more than 60 years ago. With the discovery of numerous fundamental particles researchers at CERN not only accomplished huge achievements in particle physics, but also contributed to advancements in the fields of engineering, medical physics and computer science. Since the discovery of the Higgs boson in 2012 [2], the Large Hadron Collider (LHC) is now hoped to give access to new physics beyond the Standard Model (SM).

The data analyzed for this thesis was produced in proton-proton (pp) collisions with a center-of-mass energy of $\sqrt{s} = 13\,\text{TeV}$ and recorded with the ATLAS detector in 2015 and 2016.

Section 3.1 aims to give a concise overview of the LHC and its preaccelerators. In section 3.2 and 3.3 the main elements of the ATLAS detector and its data aquisition system are introduced. The latest upgrades for Run II are briefly introduced in section 3.4.

3.1 The Large Hadron Collider

The LHC [32, 33] is circular accelerator designed to collide two counter-circuiting hadron beams at very high energies. It is located near Geneva, Switzerland, in a tunnel complex 27 km in circumference up to 175 m beneath the ground. This infrastructure was formerly used by the Large Electron Positron Collider (LEP) between 1989 and 2000. In 2010 LHC started operation with pp collisions at $\sqrt{s} = 7\,\text{TeV}$ until 2011 and 8 TeV in 2012. After this first data taking phase ('Run I') and a maintenance and upgrade shut down, Run II started in 2015 with $\sqrt{s} = 13\,\text{TeV}$.

Protons are produced by ionizing hydrogen atoms and then accelerated in several steps before being injected as clockwise and counter-clockwise beams into the evacuated beam tubes of the LHC. Figure 3.1 sketches the scheme of the various accelerators and detectors.

The proton beam is first accelerated to 50 MeV with the linear accelerator LINAC2 before being injected into the BOOSTER synchrotron and subsequently the Proton Synchrotron (PS). Upon reaching an energy of 25 GeV the protons are then transferred to the Super Proton Synchrotron (SPS) accelerating them to 450 GeV before they are injected into the LHC. Superconductive dipole magnets generating field strengths of

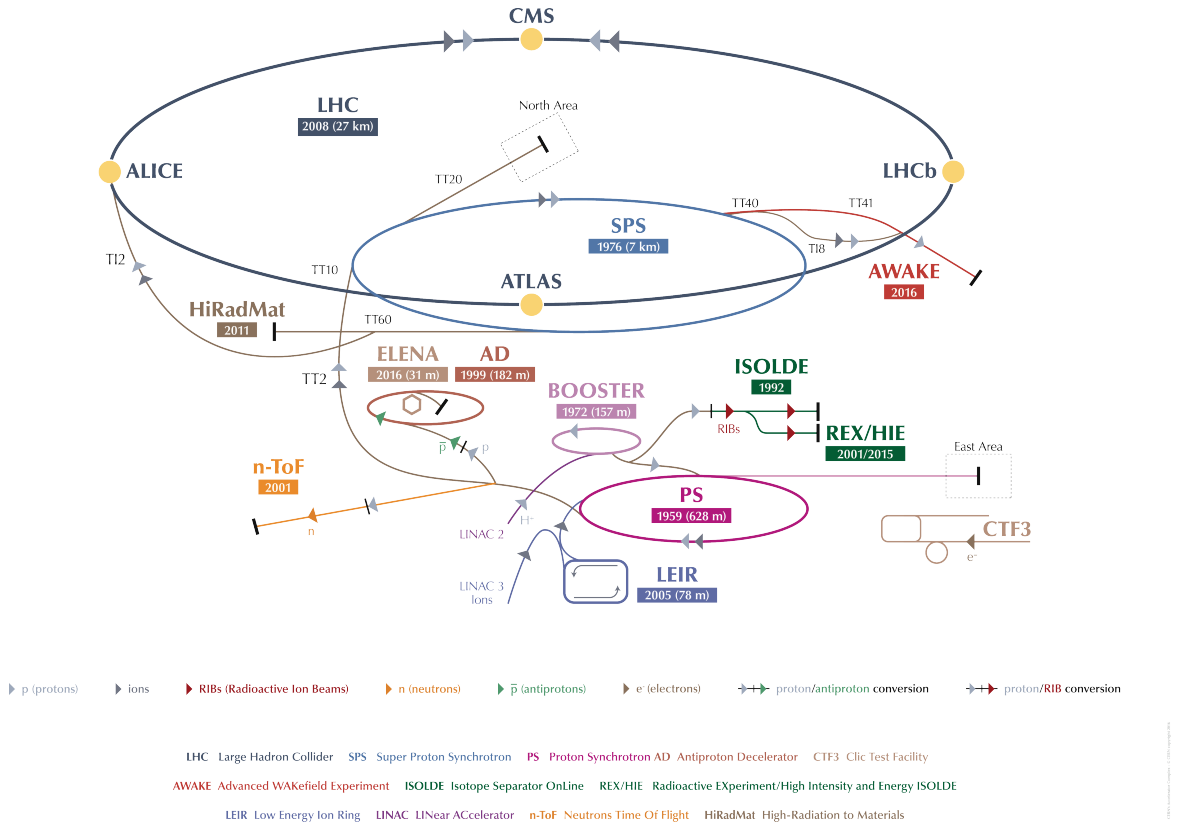

Figure 3.1: Schematic overview of the CERN accelerator complex [34].

up to 8.3 T force the protons, which are gathered in bunches with a designed spacing of 25 ns, onto nearly circular paths. After further acceleration to 6.5 TeV, resulting in a center-of-mass energy of 13 TeV, the two beams are focused and brought to collision at four interaction points, where the four major detectors ATLAS, CMS, LHCb and ALICE record the collisions. Under nominal operating conditions each beam consists of almost 3000 bunches containing at the order of 10^{11} protons leading to about 30 million bunch crossings per second [33].In 2016 on average about 24 collisions occured per bunch crossing [35]. This effect is called 'pile-up', giving in total at the order of 700 million interactions per second.

3.2 The ATLAS Detector

The central element of the ATLAS ('A Toroidal LHC ApparatuS') detector [36] consists of multiple layers of complementary subsystems concentrically arranged around the beam axis. This cylindrical part, called barrel region, is encompassed on both sides by two groups of subdetectors ordered in discs orthogonal to the beam axis. These so-called end-caps are used to detect and track particles scattered in the forward or backward direction. In total ATLAS measures 44 m in length and 25 m in diameter

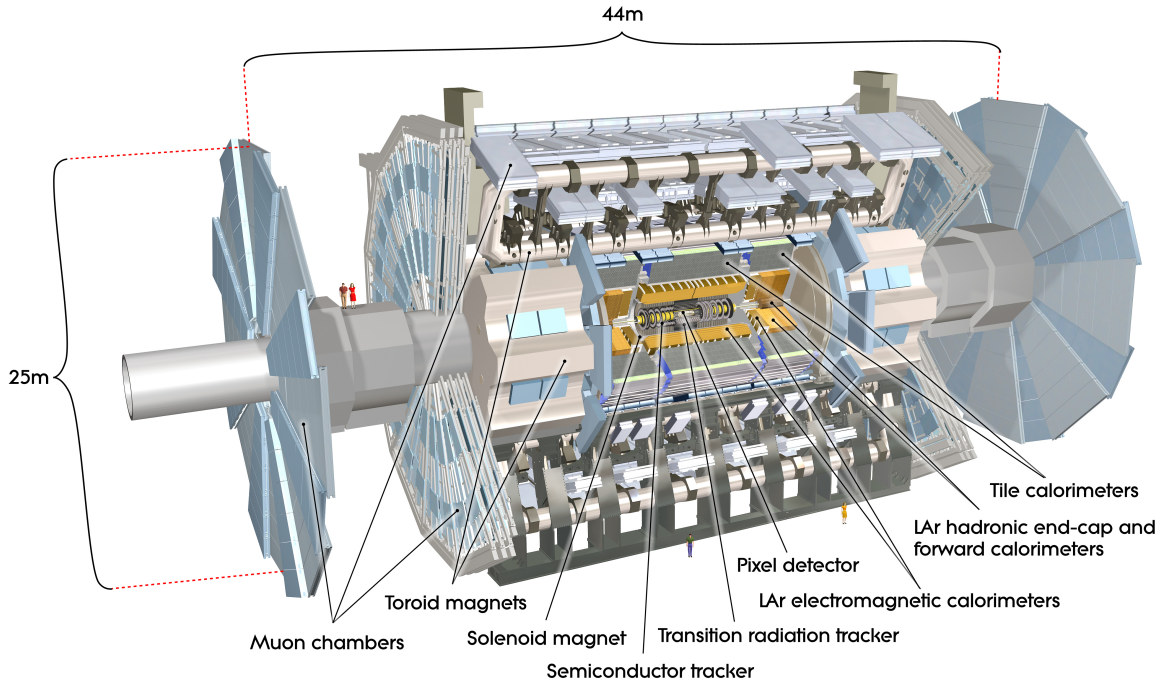

Figure 3.2: Schematic layout of the ATLAS detector [37].

and is designed to have the interaction point located in the very center of the detector. Figure 3.2 shows the schematic layout of the ATLAS detector.

A right-handed Cartesian coordinate system with its origin at the nominal interaction point is defined such that the z-axis points along the beam axis, the y-axis upwards and the x-axis towards the center of the LHC ring. As the initial momentum carried by the proton's constituents involved in the collision is unknown, energy and momentum are conserved effectively only in x-y-plane transverse to the beam axis. Therefore quantities such as the transverse momentum p_T and transverse energy $E_\mathrm{T} = \sqrt{m^2 + p_\mathrm{T}^2}$ of a particle of mass m are naturally of particular interest in hadron-hadron collision experiments. Particles, which cannot be detected with ATLAS, such as neutrinos thus manifest in a non-zero net transverse momentum indicating missing transverse momentum.

The direction of objects in the detector can also be described using the azimuthal angle ϕ around the beam axis and the pseudorapidity[3] $\eta = -\ln\tan\frac{\theta}{2}$, where θ is the polar angle measured from the beam axis. The distance between objects is defined by $\Delta R = \sqrt{\Delta\eta^2 + \Delta\phi^2}$.

The various subsystems of the ATLAS detector can be grouped into three major ele-

[3]This assumes massless particles, which is valid in the ultrarelativistic limit, i. e. if $E \gg m$. For extremely heavy particles, where this assumption does not hold, the rapidity $y = \frac{1}{2}\ln\frac{E+p_z}{E-p_z}$ is used instead.

ments: the Inner Detector (ID), the calorimeters and the Muon Spectrometer (MS), sorted from the inside to the outside of the detector.

The ID is immersed in a homogeneous magnetic field of 2 T generated by a thin superconducting solenoid magnet around it [38]. As a result the trajectory of charged particles is curved, which allows for a computation of the particles momentum and the sign of its electric charge. Similarly eight barrel toroid magnets and two end-cap toroid magnets are installed outside the calorimeter inducing magnetic fields inside the MS [39].

Focusing on the barrel region of the ATLAS detector a brief description of the three major subsystems is given in the following:

- **Inner Detector (ID):** The innermost layer of the ATLAS detector is used to reconstruct the precise position of vertices and to track charged particles allowing for high-precision momentum measurements [40, 41].

  Closest to the interaction point lie in total four cylindrical layers of silicon pixel detectors providing a high spatial resolution measurement of the large number of tracks. This information is crucial for identifying particles such as b-quarks and taus, which distinguish themselves by creating secondary vertices due to their relatively long lifetimes.

  The pixel detectors are surrounded by semiconductor trackers (SCT) [42]. They consist of long, narrow silicon strips arranged parallel to the beam axis allowing for a precise tracking especially in the plane transverse to the beam axis.

  These two high-precision tracking detectors are complemented by a transition radiation tracker (TRT), a combination of gaseous straw trackers and transition radiation detectors [43]. Besides contributing to the momentum measurement, the TRT is capable of generating, detecting and tracking transition radiation photons used to improve the identification efficiency for electrons.

- **Calorimeters:** The ID and solenoid magnets are enclosed by calorimeters measuring the energies of the collision products. Photons and electrons (positrons) are absorbed by the inner electromagnetic calorimeter (ECAL), while strongly interacting particles are stopped by the outer hadronic calorimeter (HCAL) [44, 45].

  The ECAL consists of lead and stainless steel plates as a passive absorber and liquid argon as an active detecting material arranged in an alternating, accordion-like geometry. Electrons, positron and photons deposit all their energy in the ECAL. Energy deposits from photons can be identified due to a missing corresponding track in the ID. While muons do leave a track, they are too heavy to be absorbed in the ECAL. On the other hand taus — due to their short lifetime — decay well before reaching the calorimeters. Their leptonic decay products cannot be distinguished from ordinary light leptons, but hadronically decaying taus can be reconstructed as they often feature a characteristic signature in the detector.

Quarks and gluons produced in the collision hadronize immediately leaving multiple tracks in the ID as they fragment. These showers of strongly interacting, color-neutral mesons and baryons form jets in the detector. While they lose some of their energy in the ECAL, most is deposited in the HCAL, which is composed of alternating layers of iron absorbers and plastic scintillators.

- **Muon Spectrometer (MS):** The MS is the outermost part of the ATLAS detector used to detect and track muons that traversed the previous detector elements with minimal energy losses [46].

  Monitored Drift Tubes (MDTs) provide a high spatial resolution of the muon trajectories [47]. Together with the information of the ID, they enable a precise computation of the muon's momentum and charge on the one hand. On the other hand muons originating from cosmic radiation can be vetoed by requring that their track must go through the primary vertex.

  In addition the MS also contains Resistive Plate Chambers (RPCs) capable of fast particle detection [48]. This precise timing information is required for the trigger system and the identification of the exact bunch crossing producing the muons.

In general the end-cap structure features the same sequence of subdetectors as the barrel region with the exception of the pixel detector. Nevertheless, due to high rate of collisions with low scattering angles, the technical realization of the specific detector elements differs to cope with the high particle flux.

3.3 Trigger System

As mentioned in section 3.1 roughly 700 million pp collisions are expected to occur every second under nominal operating conditions. With approximately 2 MB of data per event ATLAS would be required to store more than 1 PB of data per second. Besides no readout or storage capacity being able to handle this tremendous stream of data, only a fraction of the events are actually of interest from a physics perspective.

A two-level trigger system is deployed to filter out events irrelevant for the analysis [49]. In the first step, hardware-based trigger (L1) system determines whether a collision should be temporarily recorded. Only a subset of the information of the total detector is used to guarantee a low latency and reduce the rate to about 100 kHz. The L1 triggers searche for interesting event topologies, such as events with specific, highly energetic particles or with large missing transverse momentum. It defines regions of interest (RoIs) in the ϕ-η-plane for the selected events, which are used as input for the software-based high-level trigger (HLT) system. These RoIs are then further processed by the corresponding HLT using the complete event information from the ATLAS detector and refining the L1 search criteria or adding new ones.

Different combinations (chains) of HLTs and L1 triggers, targeting various signatures,

are used simulteously. The selection criteria of the HLT chains are tuned to reduce the total data rate further to about 1 kHz and the selected events are written to persistent storage.

HLT chains with less stringent selection criteria are operated with a prescale to guarantee a manageable data output. This way only every n-th selected event is then actually recorded, with n being the prescale factor.

3.4 Upgrades for Run II

During the shutdown in the transition period to Run II, the ATLAS detector and its trigger system and reconstruction algorithms have experienced various upgrades [41].

One of the biggest improvements concerning the identification efficiencies of b-jets and taus is thanks to an upgrade of the pixel detector. Here an additional, fourth layer, the so-called Insertable B-Layer (IBL), was included and is now the one closest to the beam. Not only did its insertion greatly benefit the resolution in track and vertex reconstruction but it also ensures a good performance against radiation damage.

The three-level trigger system of Run I was reduced to two stages, with the previous two high-level triggers merged to one. Maintaining or even improving the trigger efficiencies was a major challenge as the trigger rates increased due to the halved bunch spacing and the higher beam energy and luminosity with respect to Run I. By reducing the number of levels the data transfer rates are reduced allowing to run improved HLT algorithms. Moreover older bottle-necks were removed and the data bandwidth for the readout system and associated computing resources were upgraded.

4 Analysis Strategy

This chapter gives a brief overview of the search for stop quark pair production in final states with two hadronically decaying taus and the analyzed data samples analyzed therefor.The analysis aims to supplement sensitivity for those signal models described in section 2.3 with high stop and low stau masses, since other sectors of this parameter space are already well covered by the analysis in the lep-had channel. By targeting distinct regions of the signal parameter space spanned by $m_{\tilde{t}}$ and $m_{\tilde{\tau}}$ the stop-to-stau search is expected to be maximally sensitive for a wide range of signal models as already proven by the Run I analysis [50].

4.1 Outline

Compared to SM processes the production of SUSY particles has in general a very low cross section making their detection rather challenging. This analysis follows the commonly used approach of a so-called cut-and-count search:

A region of the phase space of final state particles is defined to reflect the extreme kinematics expected from the hypothesized BSM process. This signal region (SR) is designed to be highly enriched with events from the investigated signal process, while having a low background expectation. If the amount of recorded data events in this region considerably exceeds the expected SM background prediction, this would possibly hint at new physics. It is thus clear that not only a SR with high signal-to-background ratio but also a reliable background prediction are keys element of the analysis. To guarantee the latter a semi-data-driven background estimate is used: Simulations are used to model the kinematics of various SM background processes and predict the expected event counts in a given selection. In corresponding control regions (CR) these predictions are then normalized to fit the observed data. The resulting normalization factors are then used to improve the purely simulated background prediction also in the SR. To eliminate a biasing of the results the SR remains blinded until the background estimate has been finalized. The normalized background predictions are compared to data in dedicated validation regions (VR) to test the fit results.

In chapter 5 the optimal design and trigger strategy for a SR targeting signal models with high stop and low stau masses is worked out using simulated data only. The contributions from the dominant background processes are normalized via a simultaneous likelihood fit in section 6. Chapter 7 presents the resulting expected discovery

significances and exclusion limits for both scenarios, either with or without an observed excess in data.

4.2 Data and Monte Carlo Samples

The presented analysis uses the full set of pp collision data at a center of mass energy of $\sqrt{s} = 13\,\text{TeV}$, recorded with the ATLAS detector in 2015 and 2016. In total this corresponds to an integrated luminosity of $\int L\,dt = 36.1\,\text{fb}^{-1}$ of data eligible for physics analysisafter the event cleaning described in section 5.2.

Simulated data samples are created in several steps using Monte Carlo (MC) methods. The underlying interaction is calculated using theoretical predictions for the matrix element and experimentally measured parton density functions (PDF) describing the momentum distribution among the proton's constituents. The products of this 'hard scatter process' and also the remnants of the protons are then extended in the next step simulating their hadronisation, fragmentation and radiation. Depending on the event generator, matrix elements are calculated to the lowest or higher orders of perturbation theory. This information needs to be propagated to the parton showering generator to avoid simulating initial and/or final state radiation twice. The final particle content of such a simulated event is translated to a signature in the detector via the GEANT4 simulation software [51]. The final output is used for the reconstruction of the individual physical objects. Thus — contrary to real data — MC samples store the information of the particles actually created in the event, allowing for a measurement of the reconstruction efficiency as explained in section 5.1.

As the raw number of simulated events is not identical with the number of expected events in a certain data taking period, MC events are weighted according to the cross-section of the process they are describing and scaled to the integrated luminosity of recorded data. Additional weights include the k-factor, representing generator dependent higher order corrections to the calculation of the matrix element, and a normalization to the total amount of simulated events N_{gen} and including a corresponding filter efficiency ϵ_{filter}. The latter accounts for events that have been discarded already right after the event generation step. This is done to only fully simulate those events, which are eligible for the analysis, and thereby reduce unnecessary computation time.

Consequently, one weighted MC event can be described by either more or less than one 'raw' simulated event. The former case is in general more attractive as it improves the credibility of the MC prediction.

A list of the MC generators used for the various background and signal processes are given in table 4.1. Dedicated signal samples are created for different combinations of the stop and stau mass parameters in steps of 50 GeV. The range of the mass values is adjusted to cover regions of the parameter space, which have not yet been excluded by earlier analyses. A complete list of all the MC samples used for this thesis is given

Process	**MC generators**
Signal	MadGraph [53, 54] + Pythia8 [55] (+ EvtGen [56])
$t\bar{t}$ [57]	Powheg [58, 59, 60] + Pythia6 [61] (+ EvtGen)
Single top [57]	Powheg + Pythia6 (+ EvtGen)
$W+$jets [62]	Sherpa [63, 64, 65, 66]
$Z+$jets [62]	Sherpa
Diboson [67]	Sherpa
$t\bar{t}+V$ [68]	MadGraph + Pythia8 (+ EvtGen)
$t\bar{t}+H$ [68]	aMC@NLO [69, 70, 71] + Herwig++ [72, 73] (+ EvtGen)
Multijet	–

Table 4.1: Overview of the signal and SM processes considered in the analysis and their corresponding MC generators. Contributions from multijet events are estimated using data-driven methods.

in the appendix and a detailed documentation of the corresponding generator versions and tunes, PDFs, cross-sections, k-factors, filter efficiencies etc. can be found in [52].

5 Object and Event Selection

This chapter introduces the objects, kinematic observables and selection criteria in the analysis. After defining so-called physics objects, the reconstructed particles and jets, in section 5.1 as well as the baseline event-based corrections in section 5.2 main focus is to define a signal region for the had-had channel in section 5.6. For this the best possible trigger strategy is studied in section 5.4 and cuts on the variables, introduced in section 5.3, are optimized for a high signal-to-background ratio. A preselection for all events considered in the signal region and for the background estimation methods in given in section 5.5.

5.1 Object Definitions

The analysis investigates events with exactly two hadronically decaying tau leptons and vetoes those containing electrons and muons. Furthermore events are expected to contain jets and a large amount of missing transverse momentum $E_{\mathrm{T}}^{\mathrm{miss}}$. It is therefor necessary to give a clear definition of these objects:

- **Jets:** Jets are reconstructed using three-dimensional topological calorimeter cell clusters and the anti-k_T jet finder algorithm [74] with the distance parameter R set to 0.4. The EM+JES+GSC (electro-magnetic; jet energy scale; global sequential calibration) scheme described in [75] is used to calibrate the jet energy measurements, by correcting for the detector response and subtracting contributions from jets of simultaneous pp collisions ("pile-up"). Jets are required to have $p_{\mathrm{T}} > 20\,\mathrm{GeV}$ and $|\eta| < 2.8$. To further mitigate contamination due to pile-up interactions the majority of tracks inside a jet with $p_{\mathrm{T}} < 60\,\mathrm{GeV}$ and $|\eta| < 2.4$ are required to originate from the primary vertex by demanding a jet-vertex-tagger [76, 77] score larger than 0.59.
- ***b*-jets:** Among those jets fulfilling the criteria described above, those originating from decays of b-quarks are identified using the `MV2c10` algorithm [78]. Besides a displacement from the primary vertex due to the relatively long lifetime of the b-quark, also characteristic jet topologies are utilized to achieve a tagging efficient of more than 77% [79, 80, 78]. For b-jets the upper bound on $|\eta|$ is lowered to 2.5, while the $p_{\mathrm{T}} > 20\,\mathrm{GeV}$ remains the same as for all jets. In the analysis jets and b-jets are treated inclusively by decorating jet objects with a corresponding tag in case they were identified to originate from a decay of a b-quark.

- **Taus:** Here the term (hadronic) tau exclusively refers to the jet containing the hadronic decay products of the actual tau lepton. The tau reconstruction is seeded by anti-k_T jets with $R = 0.4$ as the distance parameter, $p_{\mathrm{T}} > 10\,\mathrm{GeV}$ and $|\eta| < 2.5$. Corrections to the reconstructed energy are based on simulation and derived independently from the jet calibration and the dedicated tau-vertex association algorithm then links tau candidates to a primary vertex [81]. Tau candidates are required to have $p_{\mathrm{T}} > 20\,\mathrm{GeV}$ and $|\eta| < 2.47$. Furthermore also the interval $1.37 < |\eta| < 1.52$, marking the transition from barrel to end-cap calorimeters, is excluded. Tau jets must have one or three tracks (prongs) associated with a primary vertex with a total electric charge of the tracks of ± 1 [82]. Using multivariate identification algorithms (MVA) based on boosted decision trees [83], a discrimination between taus and jets can be achieved. The efficiency of the MVAs can be chosen from three working points, 'loose', 'medium' and 'tight', each with higher quality criteria than the previous. In [84] a description of the tau reconstruction in ATLAS is given.
- $\boldsymbol{E}_{\mathrm{T}}^{\mathrm{miss}}$**:** The missing transverse momentum, denoted as $E_{\mathrm{T}}^{\mathrm{miss}}$, is defined as the negative vector sum of the transverse momenta of all reconstructed objects after overlap removal and includes additional soft term [85, 86]. Soft terms refer to calorimeter energy clusters with tracks leading to the primary vertex that are not associated with any of the reconstructed objects. Hence $E_{\mathrm{T}}^{\mathrm{miss}}$ gives a good representation of the total transverse momentum carried away by invisible particles such as neutrinos and potential SUSY ord dark matter particles. Its magnitude, for convenience also referred to as $E_{\mathrm{T}}^{\mathrm{miss}}$, gives thus a handle to separate SM background from signal processes as will be shown later in section 5.6.1. A detailed description of the $E_{\mathrm{T}}^{\mathrm{miss}}$ calculation can be found in [87].

These definitions follow the recommendations of the ATLAS SUSY group given in [88]. Similar ones exist for electrons, muons and photons. Since they are not part of the events selected for the analysis of the had-had channel, as discussed later in section 5.5, it is refrained from giving also a detailed definition of these objects.

As all dedicated reconstruction algorithms run independently from one another, it can happen that the detector signature of one physical object is labeled as more than one object. A dedicated overlap removal algorithm, that defines which object is to be favored in such cases, makes sure that these ambiguities are resolved. The overlap removal procedure checks if two reconstructed objects lie within a cone of a certain size $\Delta R = \sqrt{\Delta\eta^2 + \Delta\phi^2}$ and decides which object is removed by following a given recipe. If more than two object overlap in their spatial separation of ΔR the procedure is repeated. The recommended default settings for the removal procedure provided in [89] are used in the analysis with the exception that taus are treated separately[4]: If a tau and a electron or muon is reconstructed within a cone of radius $\Delta R < 0.2$ the tau is rejected and so is the entire event (due to the veto on light leptons).

[4]By default they would be treated as regular jets in the overlap removal.

For simulation the truth record stores the information about the particles that were actually created in the event. Truth particles have a minimal p_{T} requirement of 10 GeV and $|\eta| < 3.0$. It is then possible to perform a truth-matching by requiring that the reconstructed object is within a cone of $\Delta R < 0.1$ around the 'true' object. This allows a quantification of how often the reconstruction algorithms fail to correctly identify a certain object.

Physics objects of the same type are distinguished with an index, which sorts them with respect to the magnitude of their transverse momentum in descending order, e. g. $p_{\mathrm{T}}(\tau_1) > p_{\mathrm{T}}(\tau_2)$.

5.2 Event Cleaning and Reweighting

Data corruption due to noise bursts, detector problems, software bugs and other issues is accounted for by an event cleaning procedure. This way only events are left over that are suited for a physical analysis. A list of steps relevant for the event cleaning can be found in [90].

For example events are rejected if no primary vertex has been reconstructed or if they contain muon candidates originating from cosmic radiation. Also jets stemming from non-collision backgrounds like cosmic muon showers or detector noise can lead to a rejection of the event [91].

For data samples events not suited for physical analysis are filtered out by a centrally provided 'good run list' (GRL). This affect event recorded in data taking runs where crucial detector components were not fully operational.

For simulation a 'pile-up reweighting' (PRW) has to be done: MC samples are created with pile-up profiles estimated from previously recorded data. If the amount of pile-up changes during data taking with respect to the estimate, events are reweighted such that the simulated profile fits the observed [92].

5.3 Kinematic Variables

For the definition of the signal, control and validation regions various kinematic quantities along with object multiplicities are required. Object multiplicities like N_{jet} simply count how many jets have been observed in the event. Note however that these jets also include those with a b-tag and thus $0 \leq N_{b\text{-jet}} \leq N_{\mathrm{jet}}$.

In the following the more derived kinematic variables are described.

- **Invaraint mass:** The invariant mass $m(\tau_1, \tau_2)$ is computed from the two selected taus in the ultrarelativistic limit ($E \gg m$).
- **Transverse mass:** In the case of a particle decaying into two particles a and b

with one of which being invisible, the mass M of the mother particle cannot be reconstructed via the invariant mass of the daughter system. However a lower bound on M is given by the transverse mass, computed as

$$m_{\mathrm{T}}^2(a,b) = 2\,p_{\mathrm{T}}(a)p_{\mathrm{T}}(b)(1-\cos\Delta\phi) \leq M^2 \tag{5.1}$$

in the ultrarelativistic limit [93]. Here $p_{\mathrm{T}}(a)$ and $p_{\mathrm{T}}(b)$ are the absolute values of the transverse momentum of particle a and b, respectively. Since one of them is invisible its p_{T} is provided by the missing transverse momentum and thus m_{T} usually only takes one argument with the other implicitly being identified as $E_{\mathrm{T}}^{\mathrm{miss}}$. The angle $\Delta\phi = \phi_b - \phi_a$ describes the angle in the transverse plane of the reconstructed daughter particle and $E_{\mathrm{T}}^{\mathrm{miss}}$.

A famous application of this variable is the measurement of the W-boson mass [94]. The m_{T} distribution of the selected leptons is expected to have a sharp cut-off at the W-boson mass. However, due to detector effects and other secondary sources of $E_{\mathrm{T}}^{\mathrm{miss}}$ this value may be smeared out.

- **Stransverse mass:** The stransverse mass is a continuation of the transverse mass for scenarios where a pair of particles with mass M is produced. They decay via two parallel chains 1 and 2, each containing one reconstructed object $a_{1,2}$ and one invisible particle $b_{1,2}$, respectively. Since the contributions from the invisible particles to $E_{\mathrm{T}}^{\mathrm{miss}}$ is unknown, the idea is to calculate $m_{\mathrm{T}}(a_1,b_1)$ and $m_{\mathrm{T}}(a_2,b_2)$ for all possibilities to distribute $E_{\mathrm{T}}^{\mathrm{miss}}$ on $p_{\mathrm{T}}(b_1)$ and $p_{\mathrm{T}}(b_2)$. After performing a minimization of $m_{\mathrm{T}}(a_1,b_1)$ and $m_{\mathrm{T}}(a_2,b_2)$ over all possible distributions one chooses the larger of the two:

$$m_{\mathrm{T2}}^2(a_1,a_2) = \min_{\mathbf{p}_{\mathrm{T}}(b_1)+\mathbf{p}_{\mathrm{T}}(b_2)=\mathbf{E}_{\mathrm{T}}^{\mathrm{miss}}} \left[\max\left\{m_{\mathrm{T}}^2(a_1,b_1), m_{\mathrm{T}}^2(a_2,b_2)\right\}\right] \leq M^2\,, \tag{5.2}$$

which gives by construction an upper bound on the mass M of the mother particle [95, 96]. Again, all daughter particles are assumed to be massless in the ultrarelativistic limit.

For example for $t\bar{t}$ events decaying to taus the $m_{\mathrm{T2}}(\tau_1,\tau_2)$ distribution would then be characterized by a cut-off close to the W-boson mass. As the pair produced particles of SUSY signal models are considerably heavier and produce and additional source of $E_{\mathrm{T}}^{\mathrm{miss}}$ (in the form of the LSP), a much broader distribution is expected for such processes.

The algorithm used for the m_{T2} computation in this analysis is described in [97].

- **Effective mass:** The effective mass $m_{\mathrm{eff}}(\tau_1,\tau_2)$ is defined as the scalar sum of $E_{\mathrm{T}}^{\mathrm{miss}}$, H_{T} and the p_{T} of the two selected taus. Here H_{T} is defined as the scalar sum of the two leading, i. e. highest-p_{T}, jets' transverse momenta.

5.4 Trigger Strategy

As described in section 3.3 triggers are required in order for the available storage capacities and readout electronics to be able to cope with the overwhelming amount and frequency of data created in pp collisions at the LHC. The objective of this section is to determine which trigger is suited best for the given final state under investigation. As the choice of trigger has a significant influence on the events selected for the studies to follow, this decision has to be made at an early step in the analysis. In order to not reject potential signal events only unprescaled triggers are considered, which in return means they need to have relatively high online thresholds. Thus the lowest unprescaled trigger is in particular interesting since it maximizes the recorded data under the given constraints without randomly discarding events due to a prescale.

Based on the signal models' final state containing large $E_{\mathrm{T}}^{\mathrm{miss}}$ along with two hadronically decaying taus the following three lowest unprescaled triggers are well motivated:

- **$E_{\mathrm{T}}^{\mathrm{miss}}$ trigger[5]:** Used to select events with large missing transverse momentum. The HLT online $E_{\mathrm{T}}^{\mathrm{miss}}$ is constructed using a jet-based algorithm with the HLT trigger firing at a threshold of 110 GeV. The associated L1 trigger threshold is at 50 GeV.
- **ditau trigger[6]:** Composite trigger asymmetrically consituted of two single tau triggers with online thresholds of 35 GeV and 25 GeV. In addition taus fulfilling the online p_{T} requirements must at least fulfill the medium online quality criterion. The HLT trigger is seeded by a L1 trigger[7] that fires for events with two tau candidates and three jets. Two of the latter will be identified as hadronically decaying taus in a following step leaving an additional requirement of at least one jet.
- **ditau+$E_{\mathrm{T}}^{\mathrm{miss}}$ trigger[8]:** Similar to the ditau trigger this trigger fires for two taus with an online p_{T} larger 35 GeV and 25 GeV, but requires also an online $E_{\mathrm{T}}^{\mathrm{miss}}$ of at least 50 GeV. Due to a different associated L1 trigger[9] this one does not have a jet requirement. The events recorded by the ditau+$E_{\mathrm{T}}^{\mathrm{miss}}$ trigger are therefore not just a subset of the ditau trigger.

This collection represents the lowest unprescaled triggers of the latest data taking period in 2016 [98]. Due to lower pile-up rates in earlier periods [35] some triggers ran with a lower online threshold.

In the following section 5.4.1 the concept of trigger efficiencies is addressed and evaluated for these three triggers. The trigger strategy of this analysis is then motivated in section 5.4.2 by comparing the signal acceptance for the individual triggers.

[5] HLT_xe110_mht_L1XE50
[6] HLT_tau35_medium1_tracktwo_tau25_medium1_tracktwo
[7] L1_TAU20IM_2TAU12IM_J25_2J20_3J12
[8] HLT_tau35_medium1_tracktwo_tau25_medium1_tracktwo_xe50
[9] L1_TAU20_2TAU12_XE35

5.4.1 Trigger Efficiencies

Triggers are required to make decisions on very short timescales during the data taking. Therefore only a limited amount of detector information and fast algorithms are used. The resolution of the online recommended events has thus only a rough resolution. Consequently this leads to a discrepancy between the online and the offline reconstructed values of the kinematic variables. Nevertheless it is the online thresholds that characterize the triggers. If the online value of the corresponding reference on which the trigger bases its decision is above the threshold, the event will be selected although the offline value might be much lower. On the other hand it can also happen that an event does not pass the online threshold although, with respect to its offline reference value, it should have. This mismatch is identified as an inefficiency of the trigger and the behavior is visualized by turn-on curves when plotted as a function of the offline reference.

To avoid such inefficiencies, where the trigger does not record a potentially interesting event, cuts on the offline reference are applied to ensure that the trigger is approximately fully efficient. This region is referred to as plateau region.

The trigger turn-on for the $E_{\mathrm{T}}^{\mathrm{miss}}$ trigger and the `HLT_xe50` trigger, which is part of the ditau+$E_{\mathrm{T}}^{\mathrm{miss}}$ trigger, is determined using unskimmed MC signal and $t\bar{t}$ background samples in order to guarantee an unbiased event selection. Only the $t\bar{t}$ process is considered, as it presents the largest contribution to the total background in the signal region as shown later in section 5.6.1.

The correct $E_{\mathrm{T}}^{\mathrm{miss}}$ trigger was not available for the simulated signal samples at the time these studies were done. Thus a similar one[10] with a slightly higher L1 threshold is used to calculate the $E_{\mathrm{T}}^{\mathrm{miss}}$ trigger efficiencies for all signal samples. This substitution presents therefore a conservative estimate. For background no substitution had to be made.

Moreover only $t\bar{t}$ background events with leptonic or semi-leptonic top decays are simulated in the given unskimmed sample. However this is sufficient as only final states with two hadronically decaying taus are of interest in this analysis. Events with fully hadronic top decays would only contribute to this selection in the rare case, where two jets are misidentified as taus.

It is assumed here that the efficiency of a combined trigger factorizes, i. e. that for independent trigger components its efficiency is the product of the efficiencies for the respective trigger components. This has been studied and verified, also for the ditau+$E_{\mathrm{T}}^{\mathrm{miss}}$ trigger, in [99].

No further selections are applied, besides a veto on light leptons. The reason for this is that muons are treated as jets or soft terms during the online reconstruction disregarding the muon spectrometer information. Thus for events containing high-energetic muons this leads to a disproportionally large mismatch between the online

[10] `HLT_xe110_mht_L1XE60`

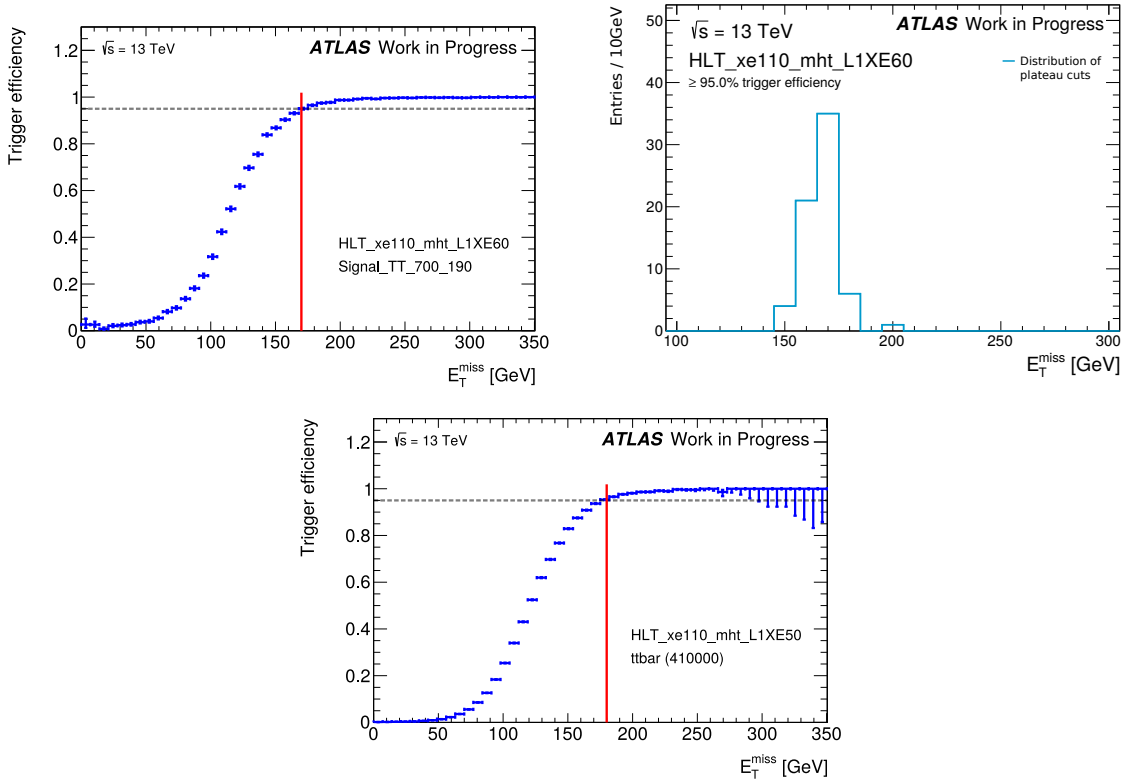

Figure 5.1: Turn-on of the $E_{\mathrm{T}}^{\mathrm{miss}}$ trigger for the signal model with $m_{\tilde{t}} = 700\,\mathrm{GeV}$ and $m_{\tilde{\tau}} = 190\,\mathrm{GeV}$ (top left) and for the (full and semi-leptonic) $t\bar{t}$ process (bottom). The red, vertical lines represent the start of the plateau regions, here defined for $\geq 95\%$ trigger efficiency. The histogram on the top right show the distribution of these lines for all simulated signal models.

and the offline $E_{\mathrm{T}}^{\mathrm{miss}}$. Since both taus are required to decay hadronically no additional light leptons are present in the final state and thus electrons are excluded as well in this step.

The trigger efficiency is then calculated as

$$\epsilon_{\mathrm{trigger}} = \frac{N_{\mathrm{passed}}}{N_{\mathrm{total}}}\,, \tag{5.3}$$

where N_{total} is the total number of selected events and N_{passed} the number of selected events that fired the trigger.

Figure 5.1 shows the turn-on curves for the $E_{\mathrm{T}}^{\mathrm{miss}}$ trigger for a signal and $t\bar{t}$ background sample, while figure 5.2 does so for the `HLT_xe50` trigger. Here the orange line indicates the $E_{\mathrm{T}}^{\mathrm{miss}}$ threshold where the curve reaches the plateau of more than 95% efficiency. This value is extracted and plotted for every available signal point in the mass grid in the range $500\,\mathrm{GeV} \leq m_{\tilde{t}} \leq 800\,\mathrm{GeV}$ and $190\,\mathrm{GeV} \leq m_{\tilde{\tau}} \leq m_{\tilde{t}} - 10\,\mathrm{GeV}$. The offline threshold for signal is then defined as the mean of the resulting distribution.

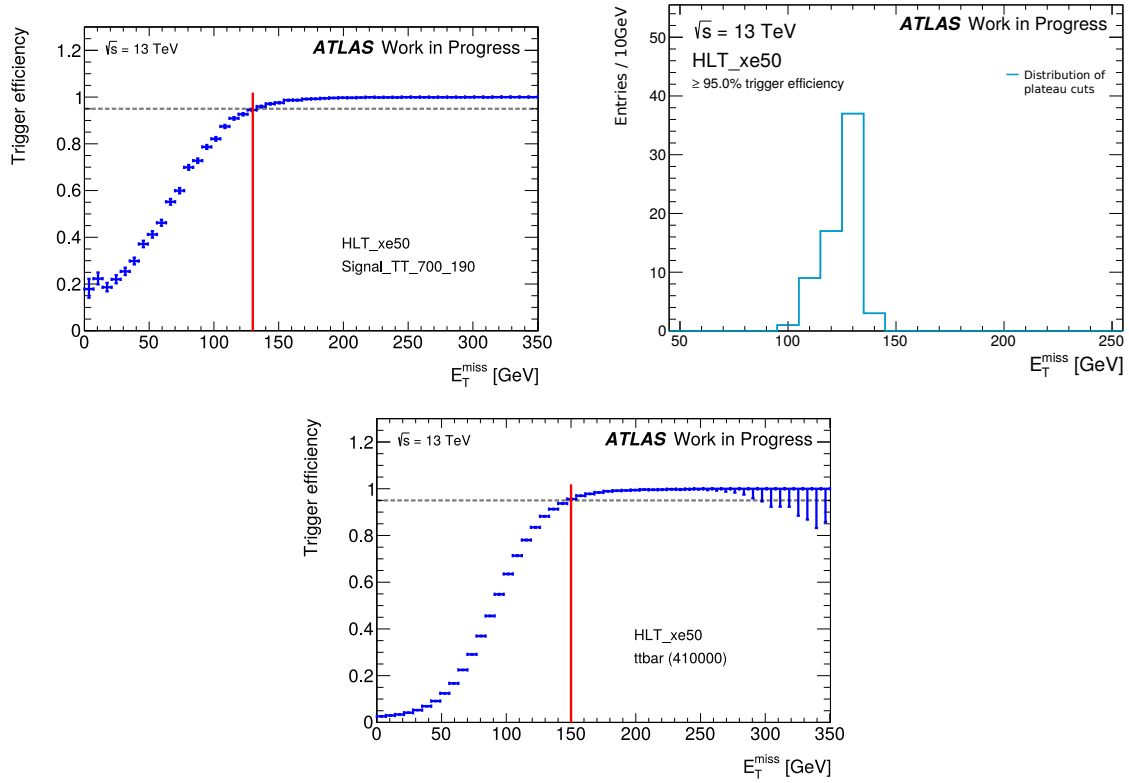

Figure 5.2: Turn-on of the `HLT_xe50` trigger for the signal model with $m_{\tilde{t}} = 700\,\text{GeV}$ and $m_{\tilde{\tau}} = 190\,\text{GeV}$ (top left) and for the (full and semi-leptonic) $t\bar{t}$ process (bottom). The red, vertical lines represent the start of the plateau regions, here defined for $\geq 95\%$ trigger efficiency. The histogram on the top right show the distribution of these lines for all simulated signal models.

For background the plateau cuts are taken directly from the corresponding plots.

In general the turn-on for background is observed to be slightly wider than for signal, thus shifting the plateau region to higher values of $E_{\text{T}}^{\text{miss}}$. In order not to underestimate the background the nominal offline thresholds for the $E_{\text{T}}^{\text{miss}}$ and `HLT_xe50` trigger are defined at 180 GeV and 150 GeV, respectively.

Trigger efficiencies for the `HLT_tau35` and `HLT_tau25` trigger, the components of the ditau and ditau+$E_{\text{T}}^{\text{miss}}$ trigger, are taken from [100]. There the efficiency has been determined in data using a 'tag-and-probe' method and compared to MC simulations.

It is important to stress again that the ditau trigger has an associated L1 trigger item, which requires at least three jets in total. Two of these L1 items will be satisfied by the hadronically decaying taus, thus giving rise to the additional requirement of at least one jet. In order for the ditau trigger to be fully efficient the p_{T} of the leading jet has to be in the plateau region of the `L1_J25` trigger. Plots of the turn-on curves of various L1 jet triggers can be found at [101]. As `L1_J25` is unfortunately not represented the

HLT_xe110_mht_L1XE50	HLT_tau35	HLT_tau25	HLT_xe50	L1_J25
180 GeV	50 GeV	40 GeV	150 GeV	80 GeV

Table 5.1: Offline thresholds for $\geq 95\%$ trigger efficiency of the $E_{\mathrm{T}}^{\mathrm{miss}}$ trigger and the components of the ditau and ditau+$E_{\mathrm{T}}^{\mathrm{miss}}$ trigger. The values for the HLT_tau35 and HLT_tau25 trigger are taken from [100].

offline threshold has been interpolated using the turn-on curves of L1_J20, L1_J50, L1_J75 and L1_J100. Thereby the plateau region has been determined to start at around $p_{\mathrm{T}}(j_1) \geq 80$ GeV.

The offline thresholds for the $E_{\mathrm{T}}^{\mathrm{miss}}$ trigger and the components of the ditau and ditau+$E_{\mathrm{T}}^{\mathrm{miss}}$ trigger are collected in table 5.1. As the triggers studied here represent the latest lowest unprescaled one also those from older data taking period (with lower online thresholds) are expected to be fully efficient with these requirements.

5.4.2 Signal Acceptance

With the efficiencies determined one can now compare the performance of the triggers with respect to the potential signal yields. Therefor the signal acceptance corresponding to the fraction of events passing the trigger along with its offline threshold, is compared in the two-dimensional $m_{\tilde{t}}$ vs. $m_{\tilde{\tau}}$ plane. In order to reject as little potential signal events a trigger with large signal acceptance is favored.

The following triggers or combination of triggers are considered:

- $E_{\mathrm{T}}^{\mathrm{miss}}$ trigger
- ditau trigger
- ditau+$E_{\mathrm{T}}^{\mathrm{miss}}$ trigger
- $E_{\mathrm{T}}^{\mathrm{miss}}$−OR−ditau trigger

The last one uses a logical OR of the $E_{\mathrm{T}}^{\mathrm{miss}}$ and ditau trigger, selecting events that passed either (or both) of them. Furthermore the events are required to pass either the $E_{\mathrm{T}}^{\mathrm{miss}}$ or the ditau trigger plateau cuts depending on which trigger they fired.

In order to compare all these triggers on a common ground some baseline cuts need to be applied:

$$N_{\tau}^{\mathrm{medium}} = 2,\ N_{\ell} = 0,\ N_{\mathrm{jets}} \geq 1\,, \tag{5.4}$$

where N_{ℓ} represents the number of light leptons, i. e. electrons and muons. The reason

Trigger	**Plateau Cuts**
$E_{\mathrm{T}}^{\mathrm{miss}}$ trigger:	$E_{\mathrm{T}}^{\mathrm{miss}} \geq 180$ GeV
ditau trigger:	$p_{\mathrm{T}}(\tau_1) \geq 50$ GeV, $p_{\mathrm{T}}(\tau_2) \geq 40$ GeV, $p_{\mathrm{T}}(j_1) \geq 80$ GeV
ditau + $E_{\mathrm{T}}^{\mathrm{miss}}$ trigger:	$p_{\mathrm{T}}(\tau_1) \geq 50$ GeV, $p_{\mathrm{T}}(\tau_2) \geq 40$ GeV, $E_{\mathrm{T}}^{\mathrm{miss}} \geq 150$ GeV
$E_{\mathrm{T}}^{\mathrm{miss}}$–OR–ditau trigger:	$E_{\mathrm{T}}^{\mathrm{miss}} \geq 180$ GeV OR $p_{\mathrm{T}}(\tau_1) \geq 50$ GeV, $p_{\mathrm{T}}(\tau_2) \geq 40$ GeV $p_{\mathrm{T}}(j_1) \geq 80$ GeV

Table 5.2: Trigger plateau cuts used in the calculation of the signal acceptance.

why taus of medium quality are chosen is explained in section 5.6.1. For events passing the individual triggers also the corresponding plateau cuts, listed in table 5.2, must be fulfilled.

With this one can define the signal acceptance as follows:

$$\text{signal acceptance} = \frac{N_{\text{passed}}\,\big|_{\text{baseline + plateau cuts}}}{N_{\text{total}}\,\big|_{\text{baseline cuts}}} \tag{5.5}$$

Figure 5.3 shows this variable plotted for all available signal points in the $m_{\tilde{t}}$ vs. $m_{\tilde{\tau}}$ plane for each of the four triggers under consideration.

The $E_{\mathrm{T}}^{\mathrm{miss}}$ trigger appears to perform well in regions where the $\widetilde{\tau}$ mass is either much less than the $\tilde{t}$ mass or, near the diagonal, where it is of same order. An opposite behavior can be observed for the ditau trigger: Here the signal acceptance takes the largest values for medium $\widetilde{\tau}$ masses. However, this region is already well-covered by the lep-had analysis. The ditau+$E_{\mathrm{T}}^{\mathrm{miss}}$ trigger on the other hand seems to perform worse than the $E_{\mathrm{T}}^{\mathrm{miss}}$ or the ditau trigger, especially in the low $m_{\tilde{\tau}}$ regime, where the analysis in the had-had channel aims to be significant. Overall it is then easy to see why the combined $E_{\mathrm{T}}^{\mathrm{miss}}-OR-$ditau trigger has the best performance over the whole signal grid, as it combines the strengths of the two individual triggers complementarily.

Taking a closer look at the combined $E_{\mathrm{T}}^{\mathrm{miss}}-OR-$ditau trigger (see figure 5.4), one finds that the gain in signal acceptance comes almost exclusively from events with $E_{\mathrm{T}}^{\mathrm{miss}} < 180\,\mathrm{GeV}$. Note that the gain seen in the right plot in figure 5.4 is not exactly zero. This small residual gain is coming from events, which have $E_{\mathrm{T}}^{\mathrm{miss}} > 180\,\mathrm{GeV}$ and pass the ditau trigger but not the $E_{\mathrm{T}}^{\mathrm{miss}}$ trigger due to the remaining small inefficiency of the $E_{\mathrm{T}}^{\mathrm{miss}}$ trigger above 180 GeV.

While this presents only a small gain in signal acceptance in the signal region, which in section 5.6.1 will be shown to have a $E_{\mathrm{T}}^{\mathrm{miss}} > 200\,\mathrm{GeV}$ requirement, the $E_{\mathrm{T}}^{\mathrm{miss}}-OR-$ditau

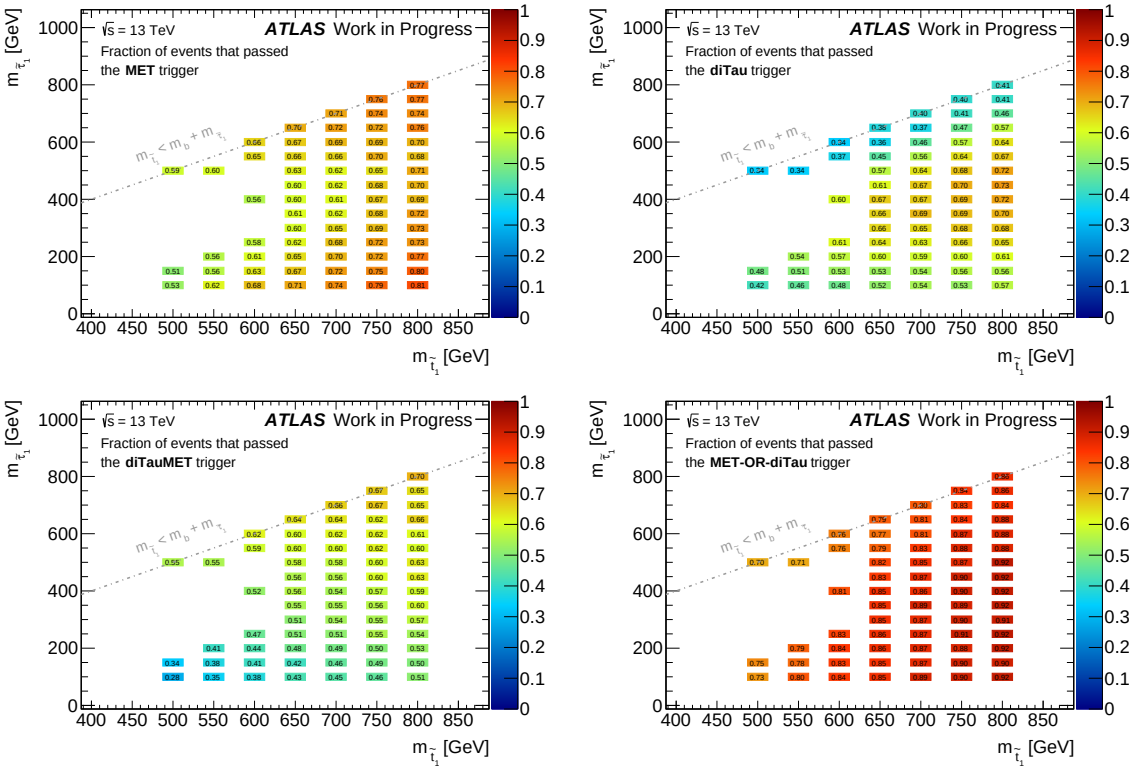

Figure 5.3: Signal acceptance for the $E_{\mathrm{T}}^{\mathrm{miss}}$ (top left), ditau (top right), ditau+$E_{\mathrm{T}}^{\mathrm{miss}}$ (bottom left) and $E_{\mathrm{T}}^{\mathrm{miss}}$−OR−ditau trigger (bottom right).

trigger will be useful in designing the control and validation regions later on in section 6. In order to define a harmonized trigger strategy for all regions the $E_{\mathrm{T}}^{\mathrm{miss}}$−OR−ditau is thus defined as the nominal trigger for this analysis.

5.4.3 Truth–$E_{\mathrm{T}}^{\mathrm{miss}}$ Studies

As seen in figure 5.3 (top left) in the previous section the $E_{\mathrm{T}}^{\mathrm{miss}}$ trigger is expected to perform best especially for model with low and high $m_{\widetilde{\tau}}$. To better understand how the signal acceptance of the $E_{\mathrm{T}}^{\mathrm{miss}}$ trigger depends on the chosen $\widetilde{\tau}$ mass, the kinematics of the invisible particles are studied. This information is only available in the MC truth record and thus this study relies exclusively on simulation. Here the slice of the signal grid with $m_{\tilde{t}} = 700\,\mathrm{GeV}$ and $90\,\mathrm{GeV} \leq m_{\widetilde{\tau}} \leq 690\,\mathrm{GeV}$ is considered and events are required to pass the baseline cuts defined in 5.4.2. Moreover the unskimmed signal samples used for this study are not required to pass any particular trigger.

The left plot in figure 5.5 shows the average absolute value of the missing transverse momentum, calculated in three ways: Once by only taking the visible particles into account (blue), thus giving the default reconstructed $E_{\mathrm{T}}^{\mathrm{miss}}$, and by calculating it from vector sum of all invisible transverse momenta (red), i. e. of all neutrino and gravitino

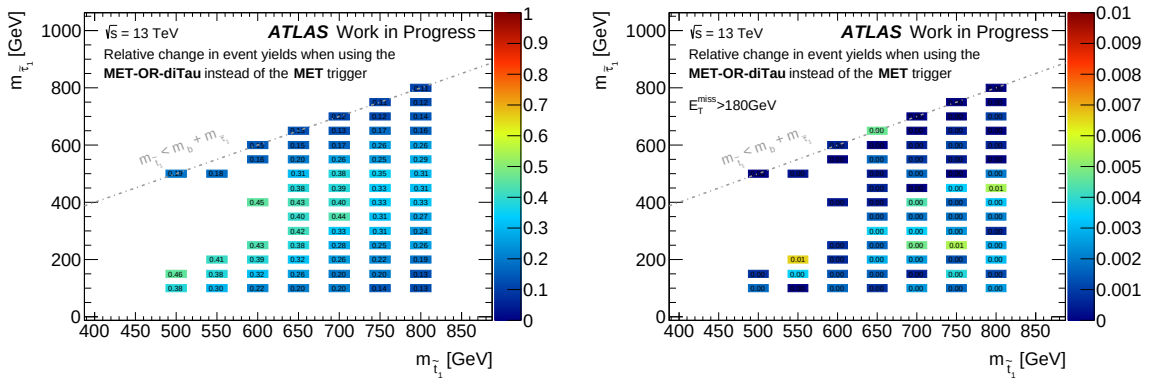

Figure 5.4: Ratio of the amount of signal events triggered by the $E_{\mathrm{T}}^{\mathrm{miss}}$−OR−ditau trigger and one triggered by the $E_{\mathrm{T}}^{\mathrm{miss}}$ trigger only (left: no $E_{\mathrm{T}}^{\mathrm{miss}}$ cut, right: $E_{\mathrm{T}}^{\mathrm{miss}} \geq 180$ GeV). Note that the color ranges are different.

momenta. Also the truth–$E_{\mathrm{T}}^{\mathrm{miss}}$ from the MC truth record is shown in green. The observed dip of the average missing transverse momtentum for models with medium stau masses can directly be translated to the decrease in signal acceptance of the $E_{\mathrm{T}}^{\mathrm{miss}}$ trigger for medium $m_{\tilde{\tau}}$. Also it can be seen that three different variants of $E_{\mathrm{T}}^{\mathrm{miss}}$ agree nicely. The reason the vector sum of all invisible transverse momenta does not exactly match the truth–$E_{\mathrm{T}}^{\mathrm{miss}}$ is due to the invisible objects available in the simulated data samples having minimal p_{T} and η requirements.

The average contributions from the various families of invisible particles is then disentangled for all signal models along the $m_{\tilde{t}} = 700\,\mathrm{GeV}$ slice, as shown in figure 5.5 on the right. To this end the scalar product of the total p_{T} of one of the families

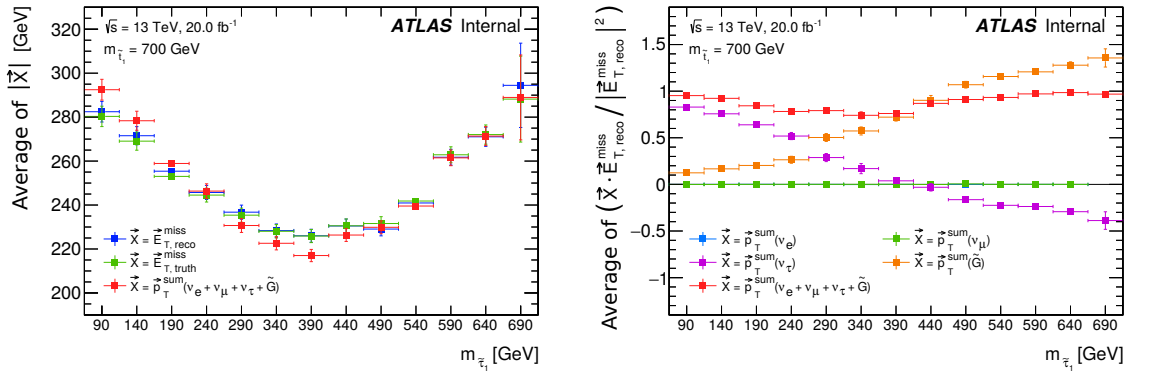

Figure 5.5: Left: Distribution of $E_{\mathrm{T}}^{\mathrm{miss}}$ (blue), truth–$E_{\mathrm{T}}^{\mathrm{miss}}$ (green) and the vector sum of all invisible particle's p_{T} (red), averaged over all events. Right: Average contribution to $E_{\mathrm{T}}^{\mathrm{miss}}$ of the various invisible particles, grouped into families (electron, muon and tau neutrinos and gravitions). In the right plot the blue markers are overlayed by the green ones.

with the reconstructed $E_{\mathrm{T}}^{\mathrm{miss}}$ is calculated. As expected no significant contribution from electron (blue) and muon neutrinos (green) is expected in this selection. For low stau masses the contribution from gravitinos (orange) is consequently also low and increases approximately proportional to $m_{\tilde{\tau}}$. An opposite behavior is observed for the tau neutrinos total p_{T} (purple): Here the tau neutrinos, coming dominantly from the three-body decay of the stop quark, give the largest contribution to $E_{\mathrm{T}}^{\mathrm{miss}}$ for large $\Delta m = m_{\tilde{t}} - m_{\tilde{\tau}}$. As Δm decreases the tau neutrinos become less energetic leading to proportionally decreasing contribution.

The first two plots in figure 5.6 show the averaged transverse angular distributions of the total p_{T} of the tau neutrinos and gravitinos, respectively, with respect to the direction of $E_{\mathrm{T}}^{\mathrm{miss}}$ for several signal models. The average p_{T} of the single invisible particles is shown in the third plot. One observes that for medium stau masses neither tau neutrinos nor gravitinos tend to have a particular strong angular correlation with $E_{\mathrm{T}}^{\mathrm{miss}}$ and that their p_{T} is approximately of the same order. In this regime both the tau neutrino's and the gravitino's p_{T} can cancel each other leading to a lower in $E_{\mathrm{T}}^{\mathrm{miss}}$. For low and high stau masses this cancellation effect becomes weaker as either the tau neutrinos or gravitinos are then the dominant source of $E_{\mathrm{T}}^{\mathrm{miss}}$.

5.5 Preselection

Based on the final state of the given signal model a preselection for events in the had-had channel can be defined. Besides discarding events that are of no particular interest for the analysis, these requirements ensure that there is no overlap with the channels targeting the other combinations of tau decay modes, e. g. with the lep-had or lep-lep channel. All preselection cuts are summarized in table 5.3.

Preselection cuts
Exactly two medium taus
No light leptons
At least two jets
$E_{\mathrm{T}}^{\mathrm{miss}}$−OR−ditau trigger fired
+ trigger requirements (see table 5.2)

Table 5.3: Preselection cuts used for the analysis in the had-had channel.

5.6 Signal Region

The SR is aimed to be highly enriched with events from the signal process, while having a low level of background contamination. One criterion used to find the optimal signal

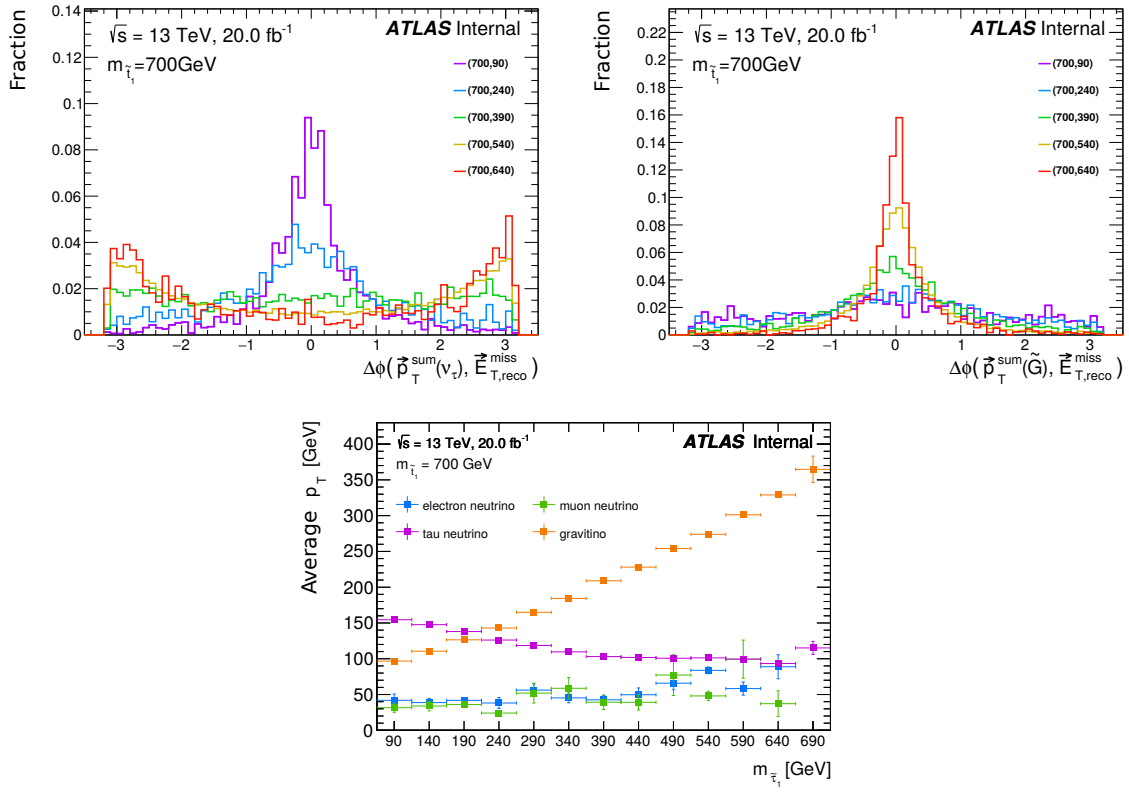

Figure 5.6: Normalized distribution of the angle between the total p_{T} of tau neutrinos (top left) or gravitions (top right) and $E_{\mathrm{T}}^{\mathrm{miss}}$ in the transverse plane, averaged over all events, for several signal models with $m_{\tilde{t}} = 700\,\mathrm{GeV}$. Bottom: Average p_{T} of the single invisible particles.

region (SR) is the significance Z. It measures the probability in units the of standard deviations σ that an observed excess in data would correspond only to a statistical upwards fluctuation of the hypothesized background. For example a deviation of 5σ is referred to as a discovery in field of high energy physics. In case the background contribution is governed by a Gaussian probability density, this would correspond to a chance of less than 0.0001% that the result is purely due to statistical fluctuations of the background.

In the following it will be shown that only low signal and background event rates can be expected in the SR. In this case the background must be described by a Poisson distribution, as the Gaussian limit breaks down. Furthermore systematic uncertainties on the background prediction must be included as well. Under these circumstances the calculation of the significance becomes more complicated. A utility to perform hypothesis tests and calculate significances is given by the `NumberCountingUtils::BinomialExpZ` function of the `RooStats` toolkit provided by the ROOT data analysis framework [102].

In the following section 5.6.1 the procedure used to optimize the SR for a given signal benchmark point is presented.

5.6.1 Signal Region Optimization

To improve the sensitivity of the stop-to-stau search in the high stop and low stau mass sector the signal model with $m_{\tilde{t}} = 850\,\text{GeV}$ and $m_{\tilde{\tau}} = 190\,\text{GeV}$ is chosen as the benchmark point for the SR of the had-had channel. In the following tables and plots different signal models will be abbreviated by their corresponding stop and stau mass, e. g. the benchmark point used for the optimization procedure is thus labeled (850,190).

Events are selected using a $E_{\text{T}}^{\text{miss}}-\text{OR}-\text{ditau}$ trigger as discussed in section 5.4 and must fulfill the preselection requirements listed in table 5.3. As stop quarks are produced in pairs in the given signal process, events are only selected if the two SM taus carry electric charges of opposite sign ($OS = 1$).

A potential SR is requested to fulfill three main criteria:

- A high signal-to-background ratio / significance
- A reliable MC background estimate
- A simple definition

Under this premise a multi-dimensional scan over a vast set of cut combinations is performed[11]. The relative uncertainty on the background is composed of the relative statistical uncertainty and a flat 40 % systematic error, as samples with systematic variations have not yet been processed.

The initial set of variables used in the optimization method is

$$\begin{aligned} &N_{b\text{-jets}},\, E_{\text{T}}^{\text{miss}},\, m_{\text{T2}}(\tau_1,\tau_2),\, m_{\text{eff}}(\tau_1,\tau_2),\, m_{\text{T}}^{\text{sum}}(\tau_1,\tau_2),\, p_{\text{T}}(\tau_1),\, p_{\text{T}}(\tau_2),\\ &\quad p_{\text{T}}(j_1),\, p_{\text{T}}(j_2),\, \Delta\phi_{\text{min}}(j_{1/2}, E_{\text{T}}^{\text{miss}}),\, H_{\text{T}},\, H_{\text{T}}/m_{\text{eff}}\,. \end{aligned} \tag{5.6}$$

The optimization procedure has been rerun multiple times, each time refining the granularity of candidate cuts for those variables, which showed to have the highest discriminating power. In the optimization, it is found that the best sensitivity can also be achieved by a smaller subset of variables that comprises $N_{b\text{-jets}}$, $E_{\text{T}}^{\text{miss}}$, $m_{\text{T2}}(\tau_1,\tau_2)$ and $p_{\text{T}}(\tau_1)$.

In addition the quality criterion of the tau identification has been varied. Figure 5.7 shows the results of the optimization procedure: Each point represents a certain combination of cuts on the subset of variables listed above either using loose (green), medium (red) or tight taus (blue). The plots compare the achievable significance, expected signal yield and raw background statistics of the various cut combinations. It can be observed that with the respect to the other tau qualities only low significances can be achieved by using tight taus. For loose taus the background suppression is relatively

[11] This uses a dedicated tool by Nikolai Hartmann: `https://gitlab.cern.ch/nihartma/arrgh`.

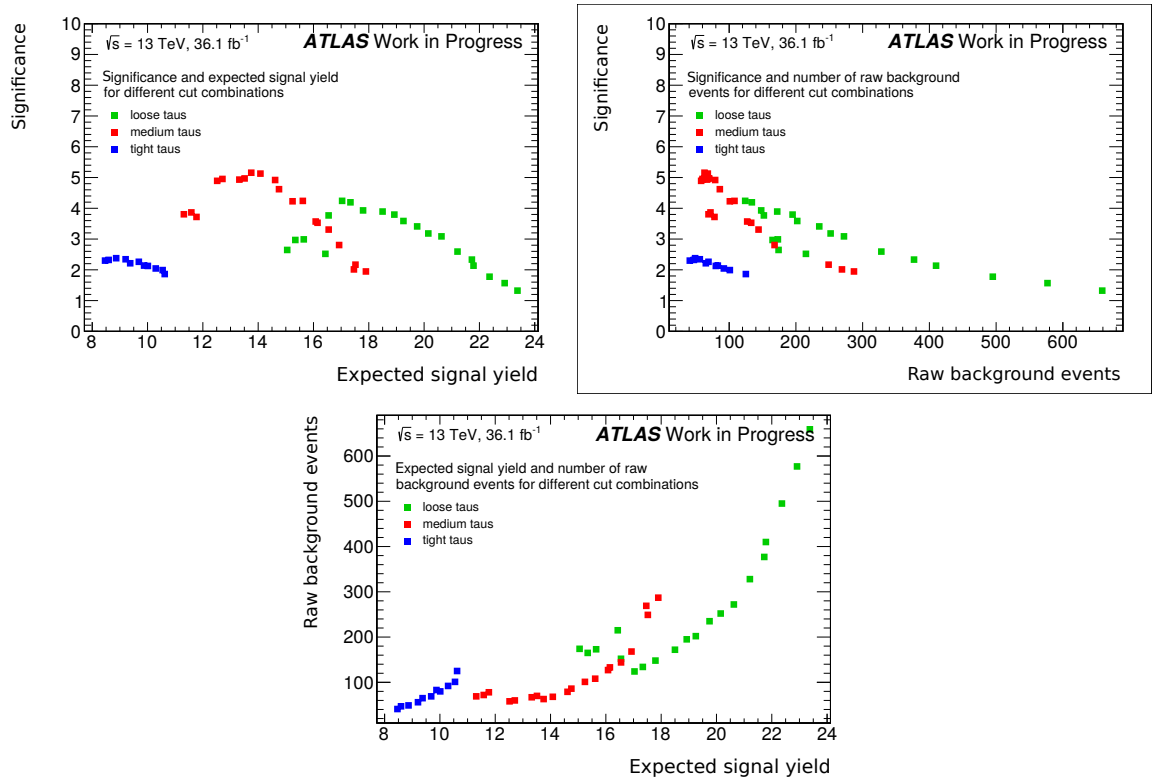

Figure 5.7: Top left: Significance versus expected signal yield. Top right: Significance versus number of raw background events. Bottom: Number of raw background events versus expected signal yield. Each point represents a cut combination.

low which has a negative effect on the achievable significance. In conclusion medium taus are found to deliver the highest possible significance and also present the best compromise between identification efficiency and solid background statistics.

The optimal cut combination using medium taus and satisfying the initial stated design criteria is given in table 5.4. The discrimination power between signal and background of the individual cut is shown in figure 5.8 using $N-1$ plots. There all cuts except the one on the variable, which is being plotted, are applied. The $m_{\mathrm{T2}}(\tau_1, \tau_2)$ variable is observed to serve as an excellent tool to separate the signal contribution from the background.

Overall the significance (in units of σ) for the chosen signal benchmark point amounts to

$$Z = 4.36\,. \tag{5.7}$$

The expected SR yields are listed in table 5.5.

The corresponding cutflow histogram together with a numerical cutflow is presented in the following section 5.6.2. The background is dominated by top quark pair production,

Variable	Cut
OS	$= 1$
$N_{b-\text{jet}}$	≥ 1
$E_{\text{T}}^{\text{miss}}$	≥ 200 GeV
$m_{\text{T2}}(\tau, \tau)$	≥ 80 GeV
$p_{\text{T}}(\tau_1)$	≥ 70 GeV

Table 5.4: Definition of the signal region. Preselection cuts are given in table 5.3.

which can be split up into two categories with respect to the results of the truth-matching described in section 5.1:

- $t\bar{t}$-Real, where both selected taus are truth-matched
- $t\bar{t}$-Fake, where at least one of the selected taus does not have a truth-match

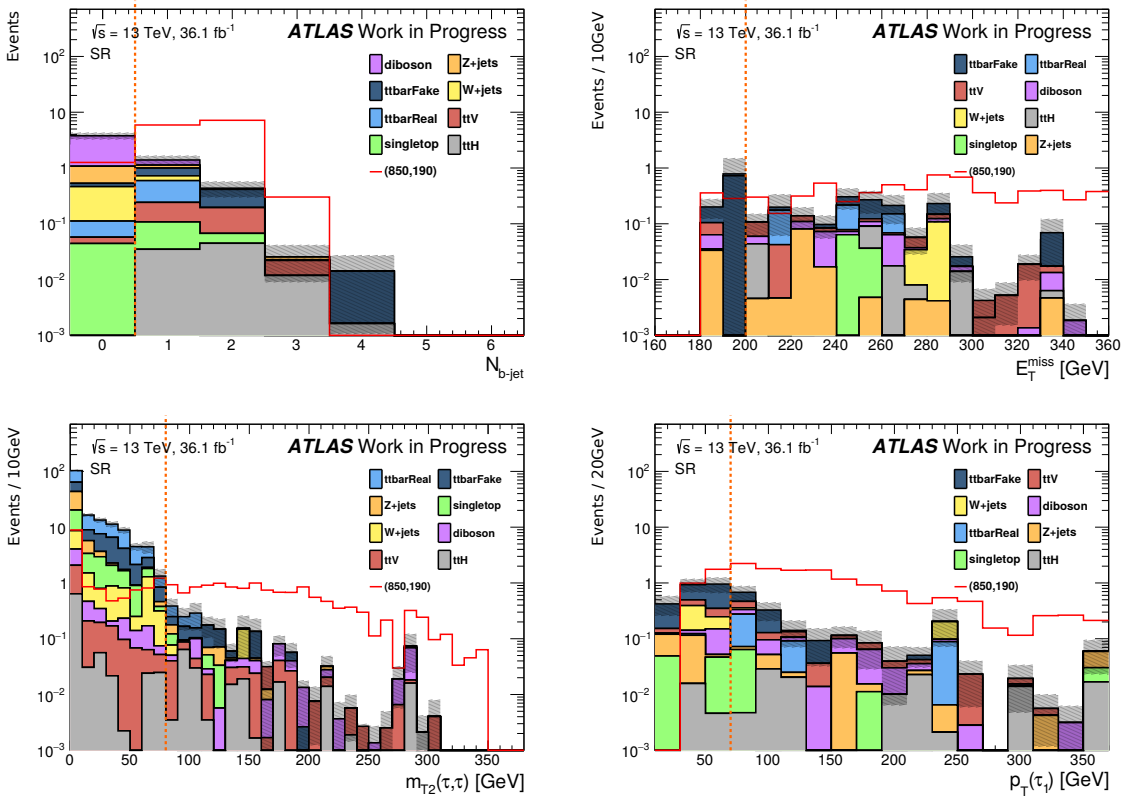

Figure 5.8: $N-1$ plots of $N_{b\text{-jets}}$ (top left), $E_{\text{T}}^{\text{miss}}$ (top right), $m_{\text{T2}}(\tau_1, \tau_2)$ (bottom left) and $p_{\text{T}}(\tau_1)$ (bottom right). The dotted orange lines represent the corresponding lower bound used for the definition of the SR.

Process	Yield	Fraction
$t\bar{t}$-Fake	0.50 ± 0.17	26.9 %
$t\bar{t}$-Real	0.35 ± 0.18	18.8 %
Diboson	0.28 ± 0.07	15.1 %
$t\bar{t} + V$	0.27 ± 0.04	14.5 %
$Z +$ jets	0.14 ± 0.05	7.6 %
$W +$ jets	0.13 ± 0.11	7.0 %
Single top	0.10 ± 0.05	5.1 %
$t\bar{t} + H$	0.09 ± 0.07	5.0 %
Total bkg.	1.87 ± 0.30	100.0 %
(850,190)	13.37 ± 0.73	

Table 5.5: Breakdown of the expected SR yields for background and the signal benchmark point (850,190), scaled to 36.1 fb^{-1}. Only statistical uncertainties are shown and no normalization factors are applied.

The background considered so far is purely estimated from MC simulation. It must therefor be ensured that the predicted background also fits the observed data in phase-space regions, where no signal contribution is expected. This is done in chapter 6. Results for the expected discovery significances over the whole signal grid and with the corrected background estimate are presented in chapter 7.

5.6.2 Cutflow

A breakdown of the event yields after each step of the SR selection, referred to as 'cutflow', is used to reveal the impact of the cuts on the signal and various background predictions. Figure 5.9 illustrates the cutflow with a plot and the corresponding event yields can be found in table 5.6. Again, a strong discrimination between signal and background is observed to arise from the $m_{\mathrm{T2}}(\tau_1, \tau_2) > 80\,\mathrm{GeV}$ requirement. The requirement of at least one b-tagged jet especially helps to suppress contributions from W and $Z +$ jets as well as diboson events.

Process	Preselection	$N_{b\text{-jet}} \geq 1$	$E_{\mathrm{T}}^{\mathrm{miss}} > 200\,\mathrm{GeV}$	$m_{\mathrm{T2}}(\tau_1, \tau_2) > 80\,\mathrm{GeV}$	$p_{\mathrm{T}}(\tau_1) > 70\,\mathrm{GeV}$
$t\bar{t}$-Fake	237.02 ± 6.86	198.69 ± 6.36	125.04 ± 4.31	1.81 ± 0.38	0.50 ± 0.17
$t\bar{t}$-Real	280.89 ± 7.94	248.57 ± 7.62	150.46 ± 4.55	0.36 ± 0.18	0.35 ± 0.18
Diboson	71.01 ± 2.04	8.44 ± 0.72	5.82 ± 0.52	0.40 ± 0.08	0.28 ± 0.07
$t\bar{t} + V$	7.70 ± 0.23	6.81 ± 0.21	4.74 ± 0.18	0.50 ± 0.06	0.27 ± 0.04
Z + jets	591.2 ± 21.52	71.93 ± 3.73	41.49 ± 2.30	0.32 ± 0.11	0.14 ± 0.05
W + jets	222.99 ± 14.33	30.19 ± 3.93	22.68 ± 3.06	0.48 ± 0.24	0.13 ± 0.11
Single top	65.00 ± 2.50	53.16 ± 2.27	39.76 ± 1.75	0.19 ± 0.07	0.10 ± 0.05
$t\bar{t} + H$	2.29 ± 0.33	1.93 ± 0.32	1.40 ± 0.28	0.11 ± 0.07	0.09 ± 0.07
totalBG	1478.10 ± 28.10	619.72 ± 11.57	391.39 ± 7.57	4.17 ± 0.52	1.87 ± 0.30
signal	40.26 ± 1.34	36.98 ± 1.29	34.29 ± 1.25	16.12 ± 0.80	13.37 ± 0.73
Z	-0.20	-0.12	-0.05	3.51	4.36

Table 5.6: Numerical cutflow with expected event yields and significance Z for the signal region scaled to $36.1\,\mathrm{fb}^{-1}$. Only statistical uncertainties are shown and no normalization factors are applied.

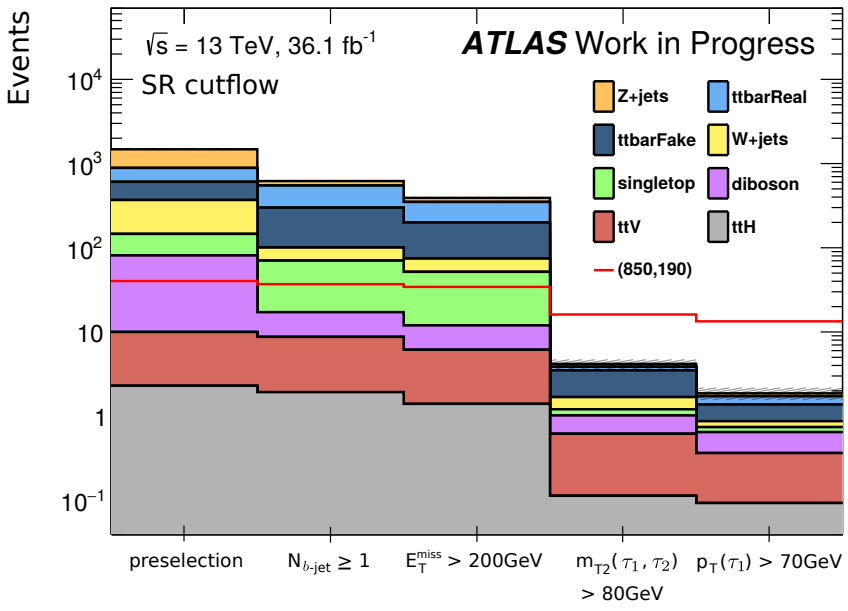

Figure 5.9: Cutflow of the signal region. The first bin represents the total event yield after the preselection described in table 5.3 and the opposite sign requirement ($OS = 1$). A corresponding numerical cutflow is given in table 5.6.

6 Background Estimation

Standard Model processes with the same signature as the investigated SUSY process are called irreducible backgrounds. In order not to depend exclusively on predictions of MC simulation it is advisable to improve the background estimate using data. Therefore control regions are constructed for the backgrounds contributing most to the signal region. The aim is to maximize the "purity" of each region, which is given by the ratio of the desired MC background to the total background, while also preserving decent statistics to calculate a meaningful normalization. The scaled background estimate is then verified by comparing it to the observed data in dedicated validation regions. All regions are required to be orthogonal to one another and the signal region to guarantee an unbiased normalization. The layout of the regions is worked out in sections 6.1 and 6.2 and the procedure of the background fit to data and the results are presented in section 6.4.

The investigated final state containing two hadronic taus is also prone to select misidentified (fake) taus that have similar signatures in the detector. One major source is given by jets produced in QCD interactions faking one ore more taus. Simulations that can model this type of interaction reliably do not exist. Such multi-jet events passing the preselection can thus lead to an underestimation of the background if one relies exclusively on MC. Their contribution is estimated using two independent data-driven methods, described in section 6.3.

6.1 Control Regions

As the background in the had-had signal region is dominated by $t\bar{t}$ events, dedicated control regions are designed to derive a normalization in a global fit. The $t\bar{t}$ background is divided into two categories:

- $t\bar{t}$-Real, where both selected signal taus are truth-matched
- $t\bar{t}$-Fake, where at least one of the selected taus does not have a truth-match

The aim is to define two separate orthogonal control regions, CR-$t\bar{t}$-Real and CR-$t\bar{t}$-Fake, such that each type of $t\bar{t}$ background can be normalized with a specific scale factor. For the control regions to be orthogonal to the signal region and to leave room for validation regions an upper cut on $m_{\mathrm{T2}}(\tau,\tau)$ at 30 GeV is required. Together with the preselection (see table 5.3) and the additional cuts used for the signal region listed

Cuts
Preselection
$N_{b\text{-jet}} \geq 1$
$m_{\mathrm{T2}}(\tau,\tau) < 30\,\mathrm{GeV}$
$p_{\mathrm{T}}(\tau_1) > 70\,\mathrm{GeV}$
$E_{\mathrm{T}}^{\mathrm{miss}} > 120\,\mathrm{GeV}$

Table 6.1: Baseline selection for events in $t\bar{t}$-Real and -Fake control regions.

in table 5.4 one can define a baseline selection for events in the $t\bar{t}$ control regions as presented in table 6.1. With respect to the SR the bound on $E_{\mathrm{T}}^{\mathrm{miss}}$ is lowered to 120 GeV to increase the available statistics. As described later in section 6.3 this cut suffices to reduce the contributions from multi-jet to a negligible amount.

Figure 6.1 shows the distribution of the invariant mass of the two selected signal taus $m(\tau_1, \tau_2)$ after the baseline $t\bar{t}$-CR selection. To suppress the contribution from Z+jets events a cut at $m(\tau_1, \tau_2) > 70$ GeV is imposed.

The next step is now to separate the $t\bar{t}$-Real and -Fake background from one another. For this imagine a $t\bar{t}$ event where the W boson from the decay of the first top quark decays hadronically and the other (from the decay of the second top quark) decays to a neutrino and a tau, the latter then decaying further to another neutrino and a hadronic jet. Such an event topology is sketched in figure 6.2.

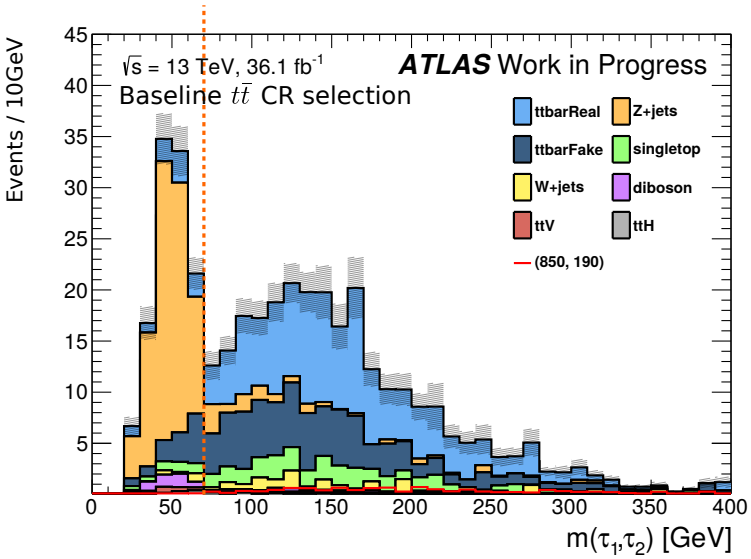

Figure 6.1: Distribution of the invariant mass of the two selected signal taus. A cut at 70 GeV is applied to reduce the contribution of Z+jets events in the $t\bar{t}$ CRs.

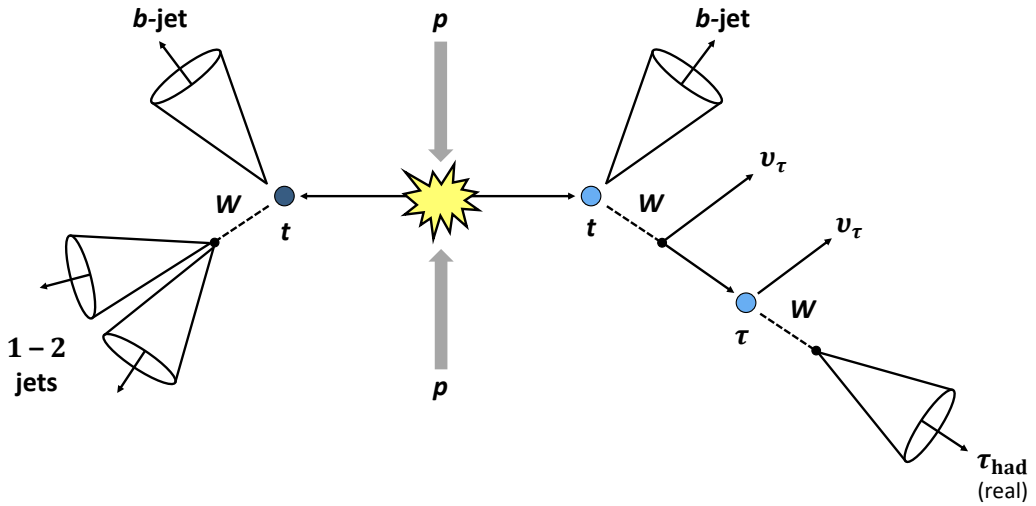

Figure 6.2: Event topology of a top quark pair decaying semi-leptonically. The tau lepton then decays further into a neutrino and a hadronic jet. In this example the latter is then assumed to be correctly matched to true tau in the reconstruction. To pass the preselection one of the other (b-)jets in the event must be misidentified as the second selected signal tau.

For the event to pass the preselection either one of the b-jets or one of the jets from the hadronic W decay needs to be misidentified as a tau. This type of event is expected to give the largest contribution to the $t\bar{t}$-Fake background: At preselection level about 87 % of the $t\bar{t}$-Fake background is given by events with exactly one fake tau. The transverse mass m_{T} of the true tau (not the reconstructed tau-jet) in the decay chain of the second top quark will then be bound from above by the W boson mass m_W (see figure 6.3, left).

However, the tau object used in the analysis is the jet consisting of the true taus hadronic decay products and parts of its momentum are thus carried away by the additional neutrino. This additional neutrino also affects $E_{\mathrm{T}}^{\mathrm{miss}}$ depending on its angle with the other neutrino. As a consequence the shape in m_{T} distribution of the reconstructed real tau can be deformed and the cut-off is smeared out with respect to the true tau's m_{T} shape. In most cases the reconstructed real tau is also the leading tau as shown in figure 6.3 on the right. Hence the transverse mass of the leading tau $m_{\mathrm{T}}(\tau_1)$ is a well motivated variable to be used in creating an orthogonal pair of control regions, CR-$t\bar{t}$-Real and CR-$t\bar{t}$-Fake: One expects $t\bar{t}$ events with one real and one fake tau to have dominantly low values of $m_{\mathrm{T}}(\tau_1)$, while in a scenario with two real (or two fake taus) no value of $m_{\mathrm{T}}(\tau_1)$ is expected to be preferred.

The left plot in figure 6.4 shows the distribution of the transverse mass of the leading selected signal tau after the Z-veto and the baseline $t\bar{t}$-CR selection. Here 70 GeV is chosen as an upper bound for CR-$t\bar{t}$-Fake and as a lower bound for CR-$t\bar{t}$-Real. As a fake tau may have an arbitrary electrical charge with respect to the other selected

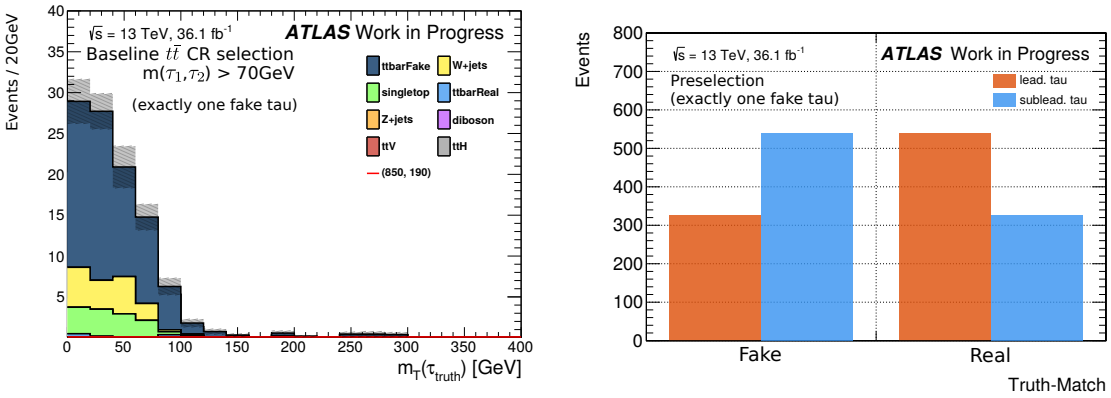

Figure 6.3: Left: Distribution of the transverse mass of the true tau from the hard scatter process in events with exactly one fake tau. For a better comparison with the $m_{\mathrm{T}}(\tau_1)$ distribution shown in figure 6.4 the baseline selection for events in the $t\bar{t}$ CRs together with Z-veto is applied. Right: Truth matching results for the leading and subleading selected signal taus in events with exactly one fake tau at preselection level. The leading tau is dominantly correctly identified in the reconstruction.

signal tau, the $t\bar{t}$-Fake contamination in the $t\bar{t}$-Real CR can be further suppressed by requiring that both taus must carry opposite charge, i.e. $OS = 1$ (see figure 6.4, right plot).

Various other variables, in particular angular distribution between different objects, have been studied to be used for increasing the $t\bar{t}$-Real and -Fake purities in their corresponding CRs. Nevertheless, only small improvements can be achieved by applying further cuts to separate the two backgrounds and they always come at the cost of statistics. Compared to any of the other investigated variables $m_{\mathrm{T}}(\tau_1)$ and the OS requirement showed to have the best separation power.

Variable	**CR-$t\bar{t}$-Real**	**CR-$t\bar{t}$-Fake**	**VR-$t\bar{t}$-Real**	**VR-$t\bar{t}$-Fake**
$N_{b\text{-jet}}$	≥ 1	≥ 1	≥ 1	≥ 1
$E_{\mathrm{T}}^{\mathrm{miss}}$	$> 120\,\mathrm{GeV}$	$> 120\,\mathrm{GeV}$	$> 160\,\mathrm{GeV}$	$> 160\,\mathrm{GeV}$
$p_{\mathrm{T}}(\tau_1)$	$> 70\,\mathrm{GeV}$	$> 70\,\mathrm{GeV}$	$> 70\,\mathrm{GeV}$	$> 70\,\mathrm{GeV}$
$m_{\mathrm{T2}}(\tau_1, \tau_2)$	$< 30\,\mathrm{GeV}$	$< 30\,\mathrm{GeV}$	$> 30\,\mathrm{GeV}$, $< 80\,\mathrm{GeV}$	$> 30\,\mathrm{GeV}$, $< 80\,\mathrm{GeV}$
$m(\tau_1, \tau_2)$	$> 70\,\mathrm{GeV}$	$> 70\,\mathrm{GeV}$	–	–
OS	$= 1$	–	$= 1$	–
$m_{\mathrm{T}}(\tau_1)$	$> 70\,\mathrm{GeV}$	$< 70\,\mathrm{GeV}$	$> 100\,\mathrm{GeV}$	$< 100\,\mathrm{GeV}$

Table 6.2: Summary of the definitions for the $t\bar{t}$ control and validation regions.

A summary of the CR definitions can be found in table 6.2, and a breakdown of the (pre-fit) yields is presented in table 6.3. In their respective CRs the $t\bar{t}$-Real and -Fake

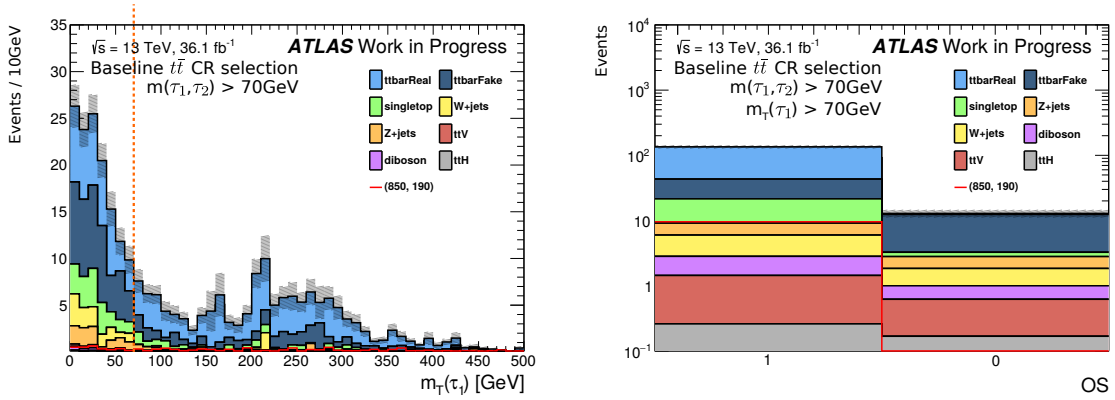

Figure 6.4: Left: Distribution of the transverse mass of the leading selected signal tau after the Z-veto has been applied. A division at 70 GeV gives two regions, one being enriched with $t\bar{t}$ events with at least one fake tau, the other with those with only real taus. Right: Distribution of events with two equally ($OS = 0$) or oppositely charged ($OS = 1$) selected signal taus after the Z-veto and $m_{\mathrm{T}}(\tau_1) > 70$ GeV is applied.

process are dominant with purities of $\sim 68\%$ and $\sim 35\%$. The signal contamination is low, with $\sim 7\%$ for CR-$t\bar{t}$-Real and $\sim 2\%$ for CR-$t\bar{t}$-Fake.

6.2 Validation Regions

The $t\bar{t}$ validation regions are designed to be orthogonal to the signal and control regions. This is achieved by requiring $30\,\mathrm{GeV} < m_{\mathrm{T2}}(\tau,\tau) < 80\,\mathrm{GeV}$. In order to define validation regions that are close to the signal region, only those events are selected which have at least one b-jet and $p_{\mathrm{T}}(\tau_1) > 70$ GeV. Furthermore with respect to the control region the lower bound on $E_{\mathrm{T}}^{\mathrm{miss}}$ is increased to 160 GeV to move closer to the signal region.

Dedicated validation regions, which discriminate real and fake taus in $t\bar{t}$ events, can be defined by choosing $m_{\mathrm{T}}(\tau_1) = 100$ GeV as a lower bound for VR-$t\bar{t}$-Real and as an upper bound for VR-$t\bar{t}$-Fake. Although slightly higher that the m_{T} threshold for the control regions, this value showed to yield the best purities in the respective validation regions. Moreover, the contribution from $t\bar{t}$ events with fake taus to VR-$t\bar{t}$-Real is reduced by requiring that both selected signal taus carry opposite charge, i.e. $OS = 1$.

A summary of the VR definitions can be found in table 6.2 and a breakdown of the (pre-fit) yields is presented in table 6.3. With about 30 events both validation regions have low but still acceptable statistics. For the $t\bar{t}$-Real and $t\bar{t}$-Fake VR purities of about 52% and 41%, respectively, can be achieved, while the signal contamination is acceptable, with $\sim 11\%$ and $\sim 4\%$, respectively.

Process	**CR-$t\bar{t}$-Real**		**CR-$t\bar{t}$-Fake**		**VR-$t\bar{t}$-Real**		**VR-$t\bar{t}$-Fake**	
$t\bar{t}$-Real	91.90 ± 5.70	(68.06 %)	43.79 ± 3.10	(32.92 %)	14.47 ± 1.78	(52.51 %)	10.01 ± 1.71	(31.83 %)
$t\bar{t}$-Fake	21.66 ± 2.43	(16.04 %)	46.59 ± 2.74	(35.03 %)	8.91 ± 1.54	(32.34 %)	12.92 ± 3.07	(41.1 %)
Single top	12.36 ± 1.27	(9.16 %)	18.29 ± 1.40	(13.75 %)	1.55 ± 0.43	(5.61 %)	4.35 ± 0.74	(13.85 %)
$W+$jets	3.15 ± 1.89	(2.33 %)	11.93 ± 1.78	(8.97 %)	1.70 ± 0.87	(6.18 %)	2.44 ± 1.02	(7.76 %)
$Z+$jets	3.14 ± 0.74	(2.32 %)	9.01 ± 1.37	(6.78 %)	0.27 ± 0.09	(0.99 %)	0.98 ± 0.30	(3.13 %)
Diboson	1.38 ± 0.25	(1.02 %)	1.32 ± 0.27	(0.99 %)	0.29 ± 0.08	(1.06 %)	0.32 ± 0.06	(1.03 %)
$t\bar{t}+V$	1.18 ± 0.09	(0.87 %)	1.43 ± 0.10	(1.07 %)	0.33 ± 0.05	(1.18 %)	0.35 ± 0.05	(1.11 %)
$t\bar{t}+H$	0.26 ± 0.08	(0.19 %)	0.66 ± 0.13	(0.5 %)	0.03 ± 0.07	(0.11 %)	0.06 ± 0.07	(0.2 %)
Total bkg.	135.03 ± 6.65	(100.0 %)	133.02 ± 4.92	(100.0 %)	27.56 ± 2.55	(100.0 %)	31.44 ± 3.75	(100.0 %)
(850, 190)	9.57 ± 0.66	(7.09 %)	2.71 ± 0.37	(2.04 %)	3.16 ± 0.43	(11.48 %)	1.10 ± 0.20	(3.51 %)

Table 6.3: Breakdown of the events yields (**pre-fit**) with statistical uncertainties in the $t\bar{t}$ control and validation regions. The values enclosed with brackets represent the fraction of the total background.

6.3 QCD Background Estimate

The absence of a reliable description of the QCD background via simulation makes it necessary to estimate its contribution via data-driven techniques. While it can be assumed that such multi-jet events will not fulfill all selection criteria in most cases, it is nevertheless vital to get a quantitative understanding of their event kinematics. In the following, two approaches for an estimation of the QCD background are presented. The aim is to determine whether its contribution in the control regions can be neglected and, if not, to derive an approximate value for it to be included in the fit.

6.3.1 Same-Sign Method

To get a general impression of the contribution from QCD events right after the preselection, the "same-sign method" is used. In the signal model and most of the background processes passing the preselection, taus are produced in pairs with opposite electrical charge. On the other hand, other objects like jets that are misidentified as taus may have an arbitrary charge. As multi-jet events will predominantly have no real taus, one can assume that the number of QCD events with oppositely charged (OS) taus is approximately equal to the number of those events in the same-sign (SS) selection:

$$N_{\mathrm{QCD}}^{\mathrm{OS}} \approx N_{\mathrm{QCD}}^{\mathrm{SS}} \approx N_{\mathrm{Data}}^{\mathrm{SS}} - N_{\mathrm{MC}}^{\mathrm{SS}}. \tag{6.1}$$

Here the SS multi-jet contribution is estimated as the difference of data and the total MC background, which does not include multi-jet events.

Multi-jet events are unlikely to contain high energetic invisible particles giving rise to large $E_{\mathrm{T}}^{\mathrm{miss}}$. Thus $E_{\mathrm{T}}^{\mathrm{miss}}$ is expected to be a variable in which QCD background has a very distinguished shape that peaks for low values. The left plot in figure 6.5 shows the estimated bin-wise contribution of QCD events after the preselection and with both taus having opposite charge in the $E_{\mathrm{T}}^{\mathrm{miss}}$ spectrum using the approximation described above. For low $E_{\mathrm{T}}^{\mathrm{miss}}$ values this estimatition does not seem to give a good description right away: If one assumes that the data-to-MC discrepancy in the low $E_{\mathrm{T}}^{\mathrm{miss}}$ regime is mainly due to contributions from multi-jet events, then the QCD background calculated with this same-sign approach underestimates the expected QCD background in the opposite-sign selection.

This mismatch can be solved by applying a global normalization factor on the same-sign QCD estimate. For this one defines a selection which is expected to be highly enriched from multi-jet events and then derives a normalization factor for the same-sign estimate such that it — together with the all other MC backgrounds — fits the observed data. Here, the scaling is determined from the first bin ($0\,\mathrm{GeV} < E_{\mathrm{T}}^{\mathrm{miss}} < 50\,\mathrm{GeV}$) of the left plot in figure 6.5. A breakdown of the expected MC yields, the (unscaled) same-sign QCD estimate and the observed data in this particular selection is listed in table 6.4.

Process	**Yield**	**Fraction**
QCD	4202.62 ± 66.45	73.26 %
$Z+$jets	1360.32 ± 47.51	23.71 %
$t\bar{t}$	81.46 ± 7.07	1.42 %
$W+$jets	65.84 ± 11.35	1.15 %
Diboson	21.56 ± 1.38	0.38 %
Single top	3.57 ± 1.06	0.06 %
$t\bar{t}+V$	0.83 ± 0.06	0.01 %
$t\bar{t}+H$	0.62 ± 0.13	0.01 %
Total bkg.	5736.82 ± 82.79	100.0 %
Observed	7639	

Table 6.4: Observed data and expected MC yields for the first bin in figure 6.5 (left), which is used to determine a normalization factor for the contribution of QCD events in the opposite-sign selection. The number of QCD events in this table thus represents the result straight from the same-sign method.

From this, the QCD factor is determined as

$$\mu_{\text{QCD}}^{\text{OS}} = 1.44 \pm 0.02\,. \tag{6.2}$$

The resulting scaled $E_{\text{T}}^{\text{miss}}$ distribution can be found in figure 6.5 on the right. Note that the bin width has been lowered to 20 GeV (previously 50 GeV) to increase the granularity of the distribution. The scaled multi-jet estimate accounts nicely for the discrepancy between data and non-QCD backgrounds over the whole $E_{\text{T}}^{\text{miss}}$ spectrum shown in the plot. A bin-wise breakdown of the distribution is presented in table 6.5. One can see that already for $E_{\text{T}}^{\text{miss}} > 120$ GeV the QCD contribution is of the same order as the statistical uncertainty on the total non-QCD background. Moreover, one finds that beyond that point the scaled multi-jet background adds up to just $(4.2 \pm 1.5)\%$ relative to the total background (MC + QCD estimate). Additional CR requirements, e.g. $N_{b\text{-jet}} \geq 1$ and $p_{\text{T}}(\tau_1) > 70$ GeV, are expected to reduce the multi-jet contribution further. To quantify this statement the corresponding distributions (at preselection level) including the scaled same-sign QCD estimate are presented in figure 6.6.

An additional requirement of at least one b-jet would cut away $\sim 86\%$ of the multi-jet background, while $p_{\text{T}}(\tau_1) > 70$ GeV cuts away $\sim 60\%$.

For the distribution in $m(\tau_1, \tau_2)$ one finds that the same-sign approach fails to give a QCD estimate compatible with data-to-MC discrepancy observed for low values of $m(\tau_1, \tau_2)$. The reason for that is not immediately clear. As for all the other previously described variables the same-sign method seems to give quite reasonable results, this mismatch points to a possible mismodelling of the charge identification in MC in the

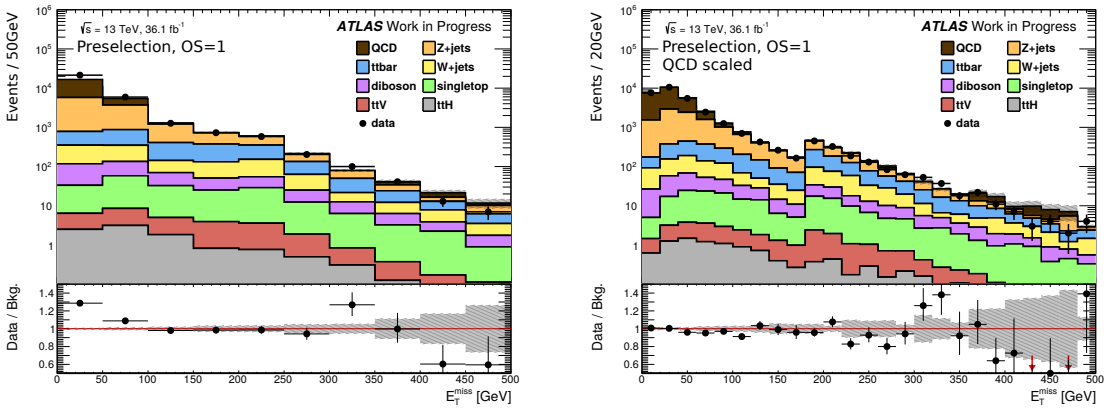

Figure 6.5: Distributions of $E_{\mathrm{T}}^{\mathrm{miss}}$ with an estimate for QCD from the same-sign method in the had-had channel, without (left) and with QCD-normalization applied (right). No other normalization factors are applied but note that the binning is different, making the gain in event yields due to the $E_{\mathrm{T}}^{\mathrm{miss}}$ trigger (in addition to ditau triggered events) especially pronounced in the right plot (bump at 180 GeV).

low $m(\tau_1, \tau_2)$ regime[12]. No further investigation have been conducted to study this behaviour as this interval is cut out by the lower bound on $m(\tau_1, \tau_2)$ at 70 GeV in the control regions anyway, leaving only the tail of the distribution.

Although $N_{b\text{-jet}}$, $p_{\mathrm{T}}(\tau_1)$ and $m(\tau_1, \tau_2)$ are not completely uncorrelated with $E_{\mathrm{T}}^{\mathrm{miss}}$ and one another, it has become clear that the contribution from multi-jet events, which is already low at preselection level for $E_{\mathrm{T}}^{\mathrm{miss}} > 120$ GeV, will be suppressed even further by the additional CR requirements to a negligible amount.

6.3.2 ABCD Method

As an alternative approach an ABCD method is used to verify the result from the same-sign QCD estimate described in the previous section. Since the multi-jet contribution drops off with increasing $E_{\mathrm{T}}^{\mathrm{miss}}$, one expects — compared to the control regions — much less QCD events in the validation and signal region. If one can confirm, that the multi-jet contribution is negligible for the CRs, it is thus also negligible for the VRs and SR. The general concept is to extrapolate the number of multi-jet events from a region of phase-space C to a region D, which is as similar as possible to the control regions. For C the QCD background yield is simply defined as the difference of oberserved data and MC events. The transfer factor TF used for the extrapolation is determined from a pair of C- and D-like regions A and B, respectively, that are enriched with contributions from multi-jet events. As seen in section 6.3.1 the $E_{\mathrm{T}}^{\mathrm{miss}}$ distribtion naturally allows for a separation of those two pairs of regions. In fact it is

[12]Note: Low-$m_{\ell\ell}$ samples for Z+jets are included (DSIDs 364198 − 364215).

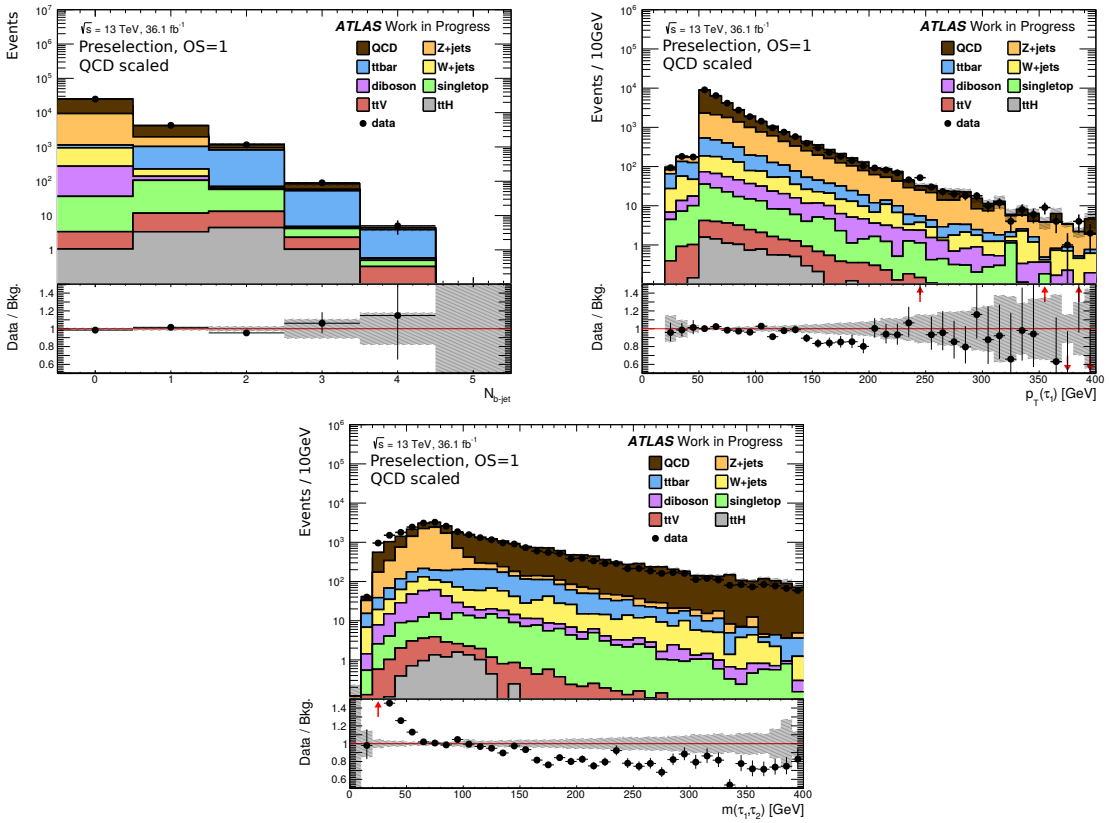

Figure 6.6: Distributions of $N_{b\text{-jet}}$ (top left), $p_{\mathrm{T}}(\tau_1)$ (top right) and $m(\tau_1, \tau_2)$ (bottom) with an estimate for QCD from the same-sign method in the had-had channel, with QCD-normalization being applied. No other normalization factors are applied.

also possible to include a pair for validation regions V_A and V_B in between to test the extrapolation before using it to estimate the QCD content of region D. All regions should be pair-wise orthogonal in order to avoid any bias on the extrapolation.

Figure 6.7 sketches the layout of these three pairs of regions. Regions A and B have an upper limit on $E_{\mathrm{T}}^{\mathrm{miss}}$ at 70 GeV, while for V_A and V_B a window cut on $E_{\mathrm{T}}^{\mathrm{miss}}$ between 70 GeV and 120 GeV is applied. The last pair C and D then has a lower bound at 120 GeV. All region pairs are then separated at $m(\tau_1, \tau_2) = 70\,\mathrm{GeV}$ and thus pairwise orthogonal. On top of the preselection requirements all regions also have to fulfill $m_{\mathrm{T2}}(\tau_1, \tau_2) < 30\,\mathrm{GeV}$ and $p_{\mathrm{T}}(\tau_1) > 70\,\mathrm{GeV}$. Together with the b-jet requirement for B, V_B and D, region D then (almost[13]) corresponds to the union of the $t\bar{t}$-real and -fake control regions. The extrapolated QCD estimate for this region should then give an appropriate estimate for the multi-jet contribution in CRs.

[13]No opposite sign (OS) requirement is applied for the two selected taus in the ABCD scheme. Since the $t\bar{t}$-Real CR requires $OS = 1$, region D does not exactly resemble the unions of the two $t\bar{t}$ control regions.

$\boldsymbol{E}_{\mathbf{T}}^{\mathbf{miss}}$**[GeV]**	**Total MC**	**QCD**
$0.0 - 20.0$	1534.2 ± 49.38	6045.05 ± 95.57
$20.0 - 40.0$	2913.08 ± 86.74	7596.25 ± 107.46
$40.0 - 60.0$	2408.6 ± 62.9	3289.19 ± 72.51
$60.0 - 80.0$	1582.69 ± 51.31	987.55 ± 44.39
$80.0 - 100.0$	1011.37 ± 25.79	274.51 ± 29.42
$100.0 - 120.0$	658.1 ± 19.27	110.49 ± 15.79
$120.0 - 140.0$	400.26 ± 13.06	9.63 ± 11.17
$140.0 - 160.0$	251.84 ± 12.92	11.81 ± 8.38
> 160.0	1577.12 ± 29.07	76.16 ± 29.31

Table 6.5: Bin-wise breakdown of the $E_{\mathrm{T}}^{\mathrm{miss}}$ distribution shown in figure 6.5 (right). Here total MC labels the sum of all yields of the simulated backgrounds, i. e. multi-jet contributions are excluded.

To enhance the contribution of multi-jet events in region A, V_A and C the b-tag requirement is dropped. Furthermore, loose taus are also included in the selection. This requires switching to the loose ditau trigger [14], which is analogue to the medium ditau trigger, but with the lower threshold on the online tau identification quality. It is assumed that the trigger is fully efficient, if the plateau cuts of its medium counterpart are applied. Since the online quality criterion is lowered, the trigger needs to be employed with a prescale n, meaning that the trigger will only write out every n-th event to cope with the higher trigger rate. For the combined data taking periods of Run II this in total corresponds to an integrated luminosity of $9.0\,\mathrm{fb}^{-1}$ collected by the loose ditau trigger. In order to match the integrated luminosity collected with the default $E_{\mathrm{T}}^{\mathrm{miss}}$ $-$OR$-$ditau (medium) trigger of $36.1\,\mathrm{fb}^{-1}$, which is being used in region B, V_B and D, the observed data in region A, V_A and C has to be reweighted. Consequently, data events that passed the loose ditau trigger, but not the $E_{\mathrm{T}}^{\mathrm{miss}}$ trigger, are scaled up by a factor of $\mu_{\mathrm{data}} = 4.0$.

This now defines the setup of the ABCD method. The transfer factor is calculated as

$$TF = \frac{N_{\mathrm{QCD}}(B)}{N_{\mathrm{QCD}}(A)}\,, \tag{6.3}$$

where N_{QCD} is defined as the number of observed data events minus total MC background. This transfer factor is used to estimate the number of multi-jet events in regions V_B and D:

[14] `HLT_tau35_loose1_tracktwo_tau25_loose1_tracktwo`

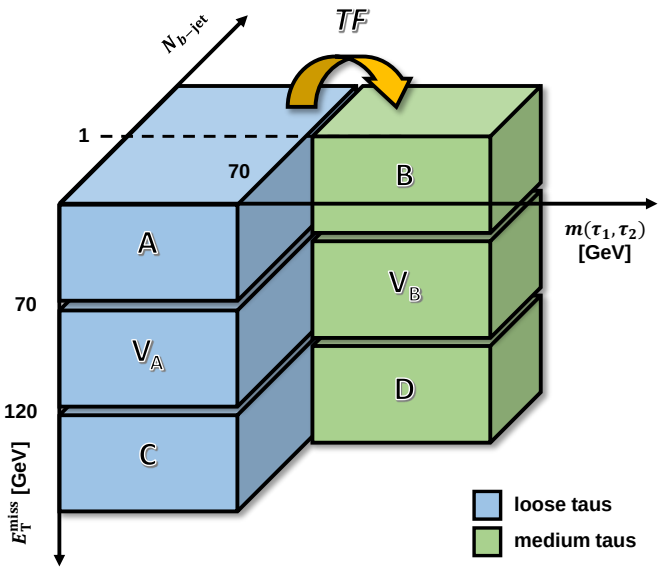

Figure 6.7: Layout of the regions used for the QCD background estimate via the ABCD method. All regions are orthogonal to one another with respect to $E_{\mathrm{T}}^{\mathrm{miss}}$ and $m(\tau_1, \tau_2)$.

$$N_{\mathrm{QCD}}(V_B) = TF \cdot N_{\mathrm{QCD}}(V_A) \tag{6.4}$$
$$N_{\mathrm{QCD}}(D) = TF \cdot N_{\mathrm{QCD}}(C) \tag{6.5}$$

Before the results are discussed it should be noted that it is important to consider correlations between the variables used to construct the ABCD scheme. If, in such a case, the transfer factor shows a large dependence on $E_{\mathrm{T}}^{\mathrm{miss}}$, it is not possible to get a reliable QCD estimate for region D, as the ratio of multi-jet events in D and C would differ from that in B and A.

One possibility is to create multiple pairs of regions $(A_1, B_1), (A_2, B_2), \ldots, (A_n, B_n)$ — all of them orthogonal and binned with respect to $E_{\mathrm{T}}^{\mathrm{miss}}$ — and then calculate a transfer factor for each A-B-pair. Several binning setups along with variations of the other cuts used to define the ABCD scheme have been investigated. It is then in principle possible to derive a $E_{\mathrm{T}}^{\mathrm{miss}}$-dependent transfer factor, for example via a linear fit to the individual transfer factors. However, mainly due to the low statistic in the tail of the $E_{\mathrm{T}}^{\mathrm{miss}}$ distribution the fit is insufficiently constrained if one uses equal bin sizes. If, on the other hand, the various $E_{\mathrm{T}}^{\mathrm{miss}}$ bins are adjusted in order to circumvent this issue, the fit becomes highly dependent on the actual binning. Testing the $E_{\mathrm{T}}^{\mathrm{miss}}$-dependent transfer factor becomes even more challenging, as a pair of validation regions will come at the cost of data points used in the fit. In the end for none of these setups did the fit give convincing results that could also be validated in dedicated regions.

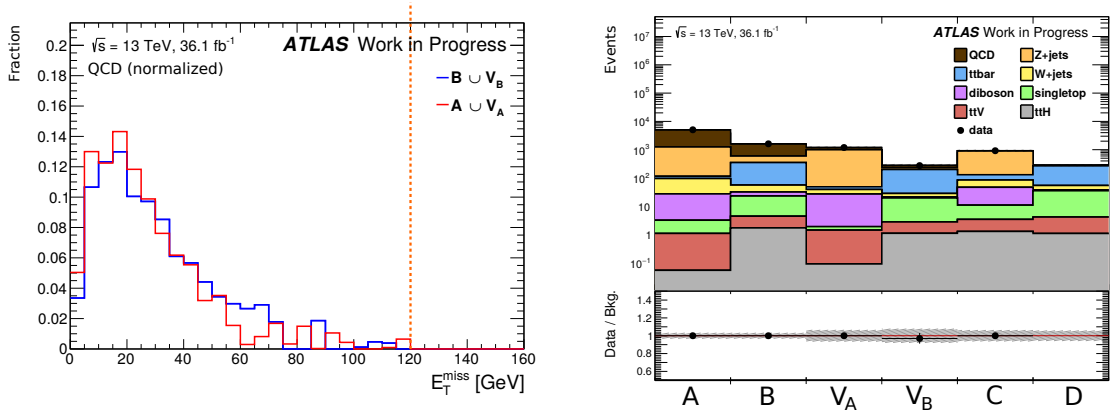

Figure 6.8: Left: Normalized $E_{\mathrm{T}}^{\mathrm{miss}}$ distribution for the QCD background ($N_{\mathrm{QCD}} \coloneqq N_{\mathrm{Data}} - N_{\mathrm{MC}}$) in the selection defined by $A \cup V_A$ (red) and $B \cup V_B$ (blue). Right: Breakdown of background yields and observed data for each region in the ABCD scheme. Note that for A, B, V_A and C the data-to-background ratio is always one by construction. In the validation region V_B the QCD estimate together with the MC background describe the observed data well.

For the ABCD scheme described here no significant correlation with $E_{\mathrm{T}}^{\mathrm{miss}}$ is observed: The left plot in figure 6.8 shows the $E_{\mathrm{T}}^{\mathrm{miss}}$ distribution for multi-jet events in the selection defined by $A \cup V_A$ (red) and $B \cup V_B$ (blue). Each distribution is normalized to one and the region with $E_{\mathrm{T}}^{\mathrm{miss}} > 120\,\mathrm{GeV}$ is blinded.

The resulting transfer factor is calculated as

$$TF = 0.27 \pm 0.02. \tag{6.6}$$

Figure 6.8 (right) shows the expected background yields and observed data, except for region D, which remains blinded. The reason for that is to first establish a reliable QCD estimate for the control regions before comparing their background predictions with data. Note that the data-to-background ratio, shown in the lower part of the plot, is equal to one for A, B, V_A and C by construction. In the validation region V_B, good agreement of data with the total background estimate from MC plus the estimated yield from multi-jet events is observed, giving confidence that the extrapolation works well.

The corresponding event yields are listed in table 6.6. There the weak point of this ABCD method becomes obvious: The number of multi-jet events extracted from the data-to-MC difference in region C has a large statistical uncertainty, amounting to roughly five times its nominal value. This leads to quite a large uncertainty of the same order on the final QCD background estimate for region D. Nevertheless with $(0.95 \pm 4.90)\,\%$ its relative contribution to the total background (MC + QCD) is still small. Furthermore, the result agrees well with the estimate from the same-sign method

derived in section 6.3.1.

This alternative approach thus shows that the multi-jet contribution plays a negligible role for the combined $t\bar{t}$ control regions. Hence the contribution from QCD interactions is considered negligible not only for the controls regions but also for the validation and signal regions. In particular it is not included in the fitting procedure described in the following section 6.4.

Region	Total MC		QCD		Observed
V_A	1245.46 ± 38.62	$(24.85 \pm 1.52)\,\%$	3766.54 ± 146.76	$(75.15 \pm 5.21)\,\%$	5012
V_B	594.65 ± 19.03	$(36.89 \pm 2.29)\,\%$	1017.35 ± 44.43	$(63.11 \pm 4.65)\,\%$	1612
C	906.07 ± 22.97	$(98.92 \pm 8.55)\,\%$	9.93 ± 50.71	$(1.08 \pm 5.62)\,\%$	916
D	280.91 ± 8.43	$(99.05 \pm 8.62)\,\%$	2.68 ± 13.07	$(0.95 \pm 4.90)\,\%$	–

Table 6.6: Breakdown of yields in region V_A, V_B, C and D. The values enclosed with brackets represent the corresponding fraction of the total background, which is defined as the sum of all backgrounds described by MC and the QCD estimate.

6.4 Simultaneous Background Fit

For the calculation of the normalization factors the HistFitter framework [103] is used. The following section aims to give a brief summary of the fitting procedure and to describe its implementation into the framework. The results are discussed in section 6.4.2.

6.4.1 Outline of the Fitting Setup

The background-only fit, in which the contribution from the signal process is assumed to be negligible, follows the statistical method of maximum-likelihood estimation. For this the parameters of the probability density functions (PDF) describing the backgrounds ought to be normalized are estimated by identifying those parameter values that maximize the likelihood of finding the observed event counts in the control regions with the given statistical models/PDFs. If the control regions are designed to be orthogonal, as it is the case in this analysis, then each covers a different region of the phase space making them statistically independent from one another. This allows for the PDFs to be simultaneously fitted to the observed data, adjusting the parameters collectively at the same time. The parameter of the PDFs describing one background are thus constrained by those describing the others.

Here the two free parameters are the normalization factors $\mu_{t\bar{t}\text{-Real}}$ and $\mu_{t\bar{t}\text{-Fake}}$ of the $t\bar{t}$-Real and $t\bar{t}$-Fake background, respectively. As the control, validation and signal regions are pair-wise orthogonal, the result of the fit is independent of the observed

number of events in the VRs and SR. The parameters of the PDFs are shared across all regions and the background event yields in the VRs and SR are predicted using the fit results calculated in the CRs. Consequently, one can then compare the observed and predicted number of events without a bias.

For the samples used so far no systematic uncertainties are available. This is being compensated by decorating all background samples with a flat systematic uncertainty of 40% in addition to the statistical error. By doing so the systematic uncertainties assigned to the backgrounds are assumed to be uncorrelated to one another. This estimate is compatible with the systematic uncertainties of $\sim 38.7\%$ observed for the had-had signal region in Run I [50] and should be viewed as a first rough estimate until all systematic variations have been processed.

6.4.2 Fit Results

For the $t\bar{t}$-Real control region 121 data events are observed, while 135.02 ± 6.65 are predicted by MC simulation (see table 6.3). This leads to a normalization factor, calculated by HistFitter, of

$$\mu_{t\bar{t}\text{-Real}} = 0.80 \pm 0.17. \tag{6.7}$$

Similarly for CR-$t\bar{t}$-Fake the number of observed data events is with 134 also close to the predicted yield of 133.02 ± 4.92 events, again yielding with

$$\mu_{t\bar{t}\text{-Fake}} = 1.21 \pm 0.40 \tag{6.8}$$

a normalization factor close to one. The larger uncertainty compared to that on $\mu_{t\bar{t}\text{-Real}}$ arises from the significantly lower purity of the $t\bar{t}$-Fake CR of only $\sim 35\%$. On the other hand, the constraint on $\mu_{t\bar{t}\text{-Real}}$ in the fit is much stronger due to relatively high purity of $\sim 68\%$ in the corresponding CR.

Figure 6.9 compares data to MC in the $t\bar{t}$ control and validation regions after the fit. A good agreement with the observed data can be found for the normalized background estimate in the validation regions. The corresponding yields are summarized in table 6.7.

Process	**CR-$t\bar{t}$-Real**		**CR-$t\bar{t}$-Fake**		**VR-$t\bar{t}$-Real**		**VR-$t\bar{t}$-Fake**	
$t\bar{t}$-Real	73.28 ± 7.53	(60.58 %)	34.92 ± 3.70	(26.08 %)	11.54 ± 1.77	(43.55 %)	7.98 ± 1.55	(24.84 %)
$t\bar{t}$-Fake	26.20 ± 4.46	(21.66 %)	56.36 ± 7.22	(42.09 %)	10.78 ± 2.47	(40.69 %)	15.63 ± 4.29	(48.66 %)
Single top	12.36 ± 1.27	(10.22 %)	18.29 ± 1.40	(13.65 %)	1.55 ± 0.43	(5.84 %)	4.35 ± 0.74	(13.55 %)
$W+$jets	3.15 ± 1.89	(2.61 %)	11.93 ± 1.78	(8.91 %)	1.70 ± 0.87	(6.43 %)	2.44 ± 1.02	(7.59 %)
$Z+$jets	3.14 ± 0.74	(2.59 %)	9.01 ± 1.37	(6.73 %)	0.27 ± 0.09	(1.03 %)	0.98 ± 0.30	(3.06 %)
Diboson	1.38 ± 0.25	(1.14 %)	1.32 ± 0.27	(0.98 %)	0.29 ± 0.08	(1.11 %)	0.32 ± 0.06	(1.01 %)
$t\bar{t}+V$	1.18 ± 0.09	(0.97 %)	1.43 ± 0.10	(1.07 %)	0.33 ± 0.05	(1.23 %)	0.35 ± 0.05	(1.09 %)
$t\bar{t}+H$	0.26 ± 0.08	(0.21 %)	0.66 ± 0.13	(0.5 %)	0.03 ± 0.07	(0.12 %)	0.06 ± 0.07	(0.2 %)
Total bkg.	120.95 ± 9.08	(100.0 %)	133.92 ± 8.54	(100.0 %)	26.49 ± 3.19	(100.0 %)	32.13 ± 4.74	(100.0 %)
Observed	121		134		22		25	

Table 6.7: Breakdown of the events yields (**post-fit**) with statistical uncertainties in the $t\bar{t}$ control and validation regions. The values enclosed with brackets represent the fraction of the total background.

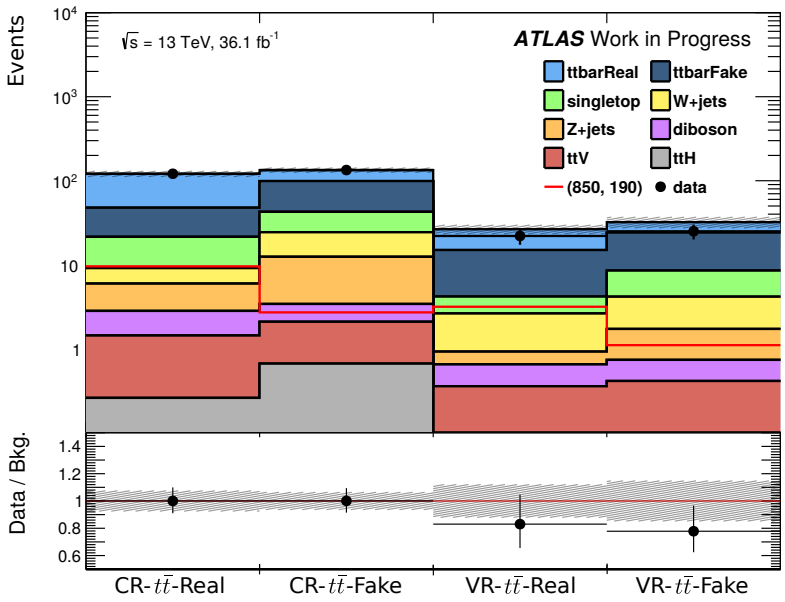

Figure 6.9: Post-fit data-to-MC comparison for CR-$t\bar{t}$-Real, CR-$t\bar{t}$-Fake, VR-$t\bar{t}$-Real and VR-$t\bar{t}$-Fake, respectively. For the control region the ratio of data to the normalized background estimate are extremely close to 1 by construction.

7 Expected Discovery Significance and Exclusion Limits

With the background estimate now established the question arises how much sensitivity can be expected to be achieved over the ($m_{\tilde{t}}$,$m_{\tilde{\tau}}$) parameter space. For a scenario where no significant excess in data is observed in the signal region, expected limits can be set to exclude parameters with a certain confidence. Table 7.1 lists the various background contributions to the signal region, scaled to an integrated luminosity of $36.1\,\mathrm{fb}^{-1}$. The $t\bar{t}$-Real and -Fake contributions have been scaled with the corresponding normalization factors derived in section 6.4 and all backgrounds are decorated with a flat relative systematic uncertainty of 40 %, as no samples with systematic uncertainties are available so far.

Process	**Yield**	**Fraction**
$t\bar{t}$-Fake	0.61 ± 0.37	32.0 %
$t\bar{t}$-Real	0.28 ± 0.19	14.8 %
Diboson	0.28 ± 0.13	14.8 %
$t\bar{t} + V$	0.27 ± 0.11	14.3 %
$Z +$ jets	0.14 ± 0.08	7.5 %
$W +$ jets	0.13 ± 0.12	6.8 %
Single top	0.10 ± 0.06	5.0 %
$t\bar{t} + H$	0.09 ± 0.08	4.9 %
Total bkg.	1.90 ± 0.48	100.0 %

Table 7.1: Breakdown of the expected SR yields for the background scaled to $36.1\,\mathrm{fb}^{-1}$. The $t\bar{t}$-Real and -Fake contributions have been scaled by their corresponding normalization factor. The uncertainties include both the statistical one and the flat relative systematic uncertainty of 40 %.

Figure 7.1 shows the expected sensitivity for the various simulated signal models. The significance in units of Gaussian standard deviations is calculated as described in section 5.6. One observes that not only for medium stau masses but also for light staus a good performance is achieved, with the potential discovery threshold of 5σ ranging up to stop masses of around 850 GeV ($\pm 10\%$). Exactly this sector of the parameter space with relatively low stau masses, for which the analysis was optimized, provides

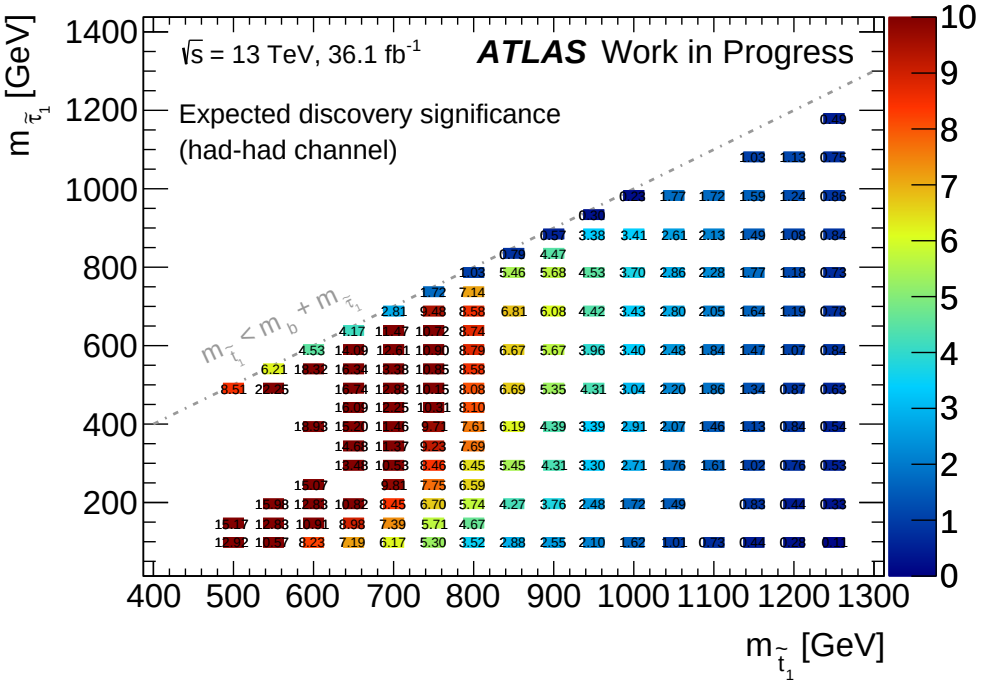

Figure 7.1: Expected discovery significance in units of Gaussian standard deviations for all simulated signal models scaled to an integrated luminosity of $36.1\,\mathrm{fb}^{-1}$

a considerable gain in sensitivity for the complete stop-to-stau analysis.

If no significant excess in data is observed in the signal region, exclusion limits with respect to a certain confidence level (CL) can be given. For every simulated signal point of the parameter space exclusion limits are calculated using the hypothesis testing utility of the HistFitter framework. Here the basic idea is to evaluate whether the observed number of events is compatible with the signal+background hypothesis, i. e. a signal is present. This compatibility is quantified by the CL_s value as described in [104]:

$$CL_s = \frac{p_{s+b}}{1 - p_b} \tag{7.1}$$

The p-values p_{s+b} and p_b represent the probability of getting the observed result or more extreme ones given that the null hypothesis, so either the signal+background ($s+b$) or background-only (b) hypothesis, is true. If the p-value is small the corresponding null hypothesis has thus a high probability of being wrong. While p_{s+b} alone would seem like a good quantity to describe the consistency of the signal+background hypothesis, it might lead to a false rejection of the signal+background hypothesis in the case of low sensitivity, i. e. when the signal+background prediction is only slightly larger than

the background prediction. In this case p_{s+b} would take small values if the observed number of data corresponds to an under-fluctuation. Nevertheless so would $1 - p_b$ and thus the use of the CL_s value instead of p_{s+b} can prevent an accidental rejection of the signal+background hypothesis. Like for the background a flat 40 % systematic uncertainty is assumed for the signal as well and — because the SR is blinded — the observed number of events is defined as the total background prediction.

Figure 7.2 depicts the contour, which encloses all signal points that can be excluded with $CL = 1 - CL_s \geq 95\%$. Again a good performance is observed in the low stau mass sector. The had-had channel alone is expected to be able to exclude top squarks of up to $\sim 1\,\text{TeV}$, should no large excess be observed in the SR after unblinding.

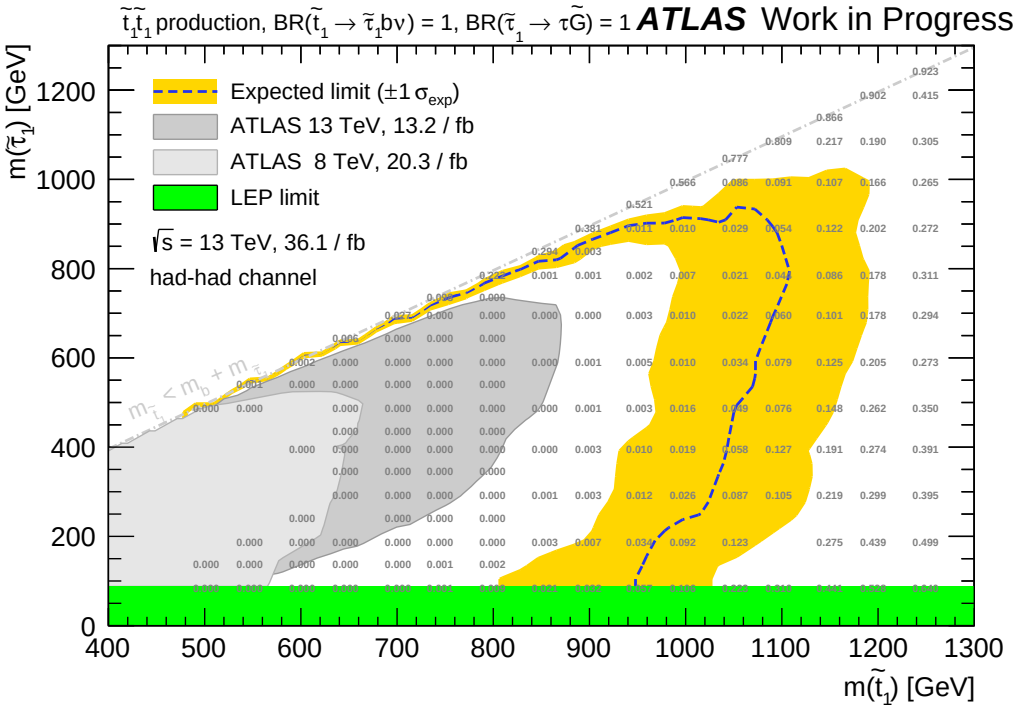

Figure 7.2: Expected exclusion limits at 95% CL (dashed blue line) together with its $\pm 1\sigma$ error band, calculated by HistFitter, in the ($m_{\tilde{t}}$,$m_{\tilde{\tau}}$)-plane. The green and the light and dark gray areas mark the exclusion limits observed by the LEP experiment [24] and by ATLAS in Run I [50] and Run II [25] (only lep-had channel; $13.2\,\text{fb}^{-1}$), respectively. The gray numbers represent the CL_s values of the corresponding simulated signal points. Between the simulated signal points this value is determined via interpolation. The plot is generated for an integrated luminosity of $36.1\,\text{fb}^{-1}$

8 Conclusion

The elegant way supersymmetry can resolve so many deficiencies of the Standard Model make it one of the most promising theoretical predictions of physics. Its natural solution to the fine-tuning problem offers a strong argument for finding new supersymmetric particles at the energy scale probed by the LHC.

In this thesis a cut based search for top squark pair production has been developed targeting final states with two hadronically decaying taus. For this $36.1\,\mathrm{fb}^{-1}$ of pp collision data, recorded with the ATLAS detector in 2015 and 2016, has been analyzed. The best trigger strategy has been studied and a corresponding signal region has been designed to strike an optimal balance between sensitivity and sufficient MC background statistics. The analysis uses events that fired either the $E_{\mathrm{T}}^{\mathrm{miss}}$ or the ditau drigger. Dedicated control regions have been defined for the major contributing background processes, $t\bar{t}$-Real and $t\bar{t}$-Fake, to derive normalization factors in a simultaneous background-only fit to data. The normalized background prediction has been found to yield a good agreement with data also in the dedicated validation regions. Using two independent methods the contribution from multi-jet events was shown to be negligible for the fitting procedure as well as for the signal and validation regions.

One major goal for the had-had channel is to extend the sensitivity of the stop-to-stau search to the light stau sector of the signal parameter space. A first estimate for the exclusion potential — assuming that no signal is observed — showed that previously set limits are expected to be pushed further up to stop masses of about 1 TeV, also in the light stau regime. Due to time constraints the full set of systematic variations has not yet been included. With this last hurdle hopefully taken soon the analysis of had-had channel is close to unblinding the signal region. The final results are aimed to be presented in combination with the findings from the other channels.

Appendix: List of MC Samples

Diboson samples:

mc15_13TeV.361069.Sherpa_CT10_llvvjj_ss_EW4.merge.DAOD_SUSY3.e3836_s2726_r7772_r7676_p2949
mc15_13TeV.361070.Sherpa_CT10_llvvjj_ss_EW6.merge.DAOD_SUSY3.e3836_s2608_r7772_r7676_p2949
mc15_13TeV.361071.Sherpa_CT10_lllvjj_EW6.merge.DAOD_SUSY3.e3836_s2726_r7772_r7676_p2949
mc15_13TeV.361072.Sherpa_CT10_lllljj_EW6.merge.DAOD_SUSY3.e3836_s2608_s2183_r7772_r7676_p2949
mc15_13TeV.361073.Sherpa_CT10_gllll.merge.DAOD_SUSY3.e3836_s2608_s2183_r7772_r7676_p2949
mc15_13TeV.361077.Sherpa_CT10_ggllvv.merge.DAOD_SUSY3.e4641_s2726_r7772_r7676_p2949
mc15_13TeV.363355.Sherpa_221_NNPDF30NNLO_ZqqZvv.merge.DAOD_SUSY3.e5525_s2726_r7772_r7676_p2949
mc15_13TeV.363356.Sherpa_221_NNPDF30NNLO_ZqqZll.merge.DAOD_SUSY3.e5525_s2726_r7772_r7676_p2949
mc15_13TeV.363357.Sherpa_221_NNPDF30NNLO_WqqZvv.merge.DAOD_SUSY3.e5525_s2726_r7772_r7676_p2949
mc15_13TeV.363358.Sherpa_221_NNPDF30NNLO_WqqZll.merge.DAOD_SUSY3.e5525_s2726_r7772_r7676_p2949
mc15_13TeV.363359.Sherpa_221_NNPDF30NNLO_WpqqWmlv.merge.DAOD_SUSY3.e5583_s2726_r7772_r7676_p2949
mc15_13TeV.363360.Sherpa_221_NNPDF30NNLO_WplvWmqq.merge.DAOD_SUSY3.e5805_s2726_r7772_r7676_p2949
mc15_13TeV.363489.Sherpa_221_NNPDF30NNLO_WlvZqq.merge.DAOD_SUSY3.e5525_s2726_r7772_r7676_p2949
mc15_13TeV.363490.Sherpa_221_NNPDF30NNLO_llll.merge.DAOD_SUSY3.e5332_s2726_r7772_r7676_p2949
mc15_13TeV.363491.Sherpa_221_NNPDF30NNLO_lllv.merge.DAOD_SUSY3.e5332_s2726_r7772_r7676_p2949
mc15_13TeV.363492.Sherpa_221_NNPDF30NNLO_llvv.merge.DAOD_SUSY3.e5332_s2726_r7772_r7676_p2949
mc15_13TeV.363493.Sherpa_221_NNPDF30NNLO_lvvv.merge.DAOD_SUSY3.e5332_s2726_r7772_r7676_p2949
mc15_13TeV.363494.Sherpa_221_NNPDF30NNLO_vvvv.merge.DAOD_SUSY3.e5332_s2726_r7772_r7676_p2949

Single top samples:

mc15_13TeV.407018.PowhegPythiaEvtGen_P2012CT10_Wt_inclusive_top_HT500.merge.DAOD_SUSY3.e4024_s2608_r7725_r7676_p2949
mc15_13TeV.407019.PowhegPythiaEvtGen_P2012CT10_Wt_inclusive_top_MET200.merge.DAOD_SUSY3.e4024_s2608_r7725_r7676_p2949
mc15_13TeV.407020.PowhegPythiaEvtGen_P2012CT10_Wt_inclusive_tbar_HT500.merge.DAOD_SUSY3.e4024_s2608_r7725_r7676_p2949
mc15_13TeV.407021.PowhegPythiaEvtGen_P2012CT10_Wt_inclusive_tbar_MET200.merge.DAOD_SUSY3.e4024_s2608_r7725_r7676_p2949
mc15_13TeV.410011.PowhegPythiaEvtGen_P2012_singletop_tchan_lept_top.merge.DAOD_SUSY3.e3824_s2608_s2183_r7725_r7676_p2949
mc15_13TeV.410012.PowhegPythiaEvtGen_P2012_singletop_tchan_lept_antitop.merge.DAOD_SUSY3.e3824_s2608_s2183_r7725_r7676_p2949
mc15_13TeV.410013.PowhegPythiaEvtGen_P2012_Wt_inclusive_top.merge.DAOD_SUSY3.e3753_s2608_s2183_r7725_r7676_p2949
mc15_13TeV.410014.PowhegPythiaEvtGen_P2012_Wt_inclusive_antitop.merge.DAOD_SUSY3.e3753_s2608_s2183_r7725_r7676_p2949
mc15_13TeV.410025.PowhegPythiaEvtGen_P2012_SingleTopSchan_noAllHad_top.merge.DAOD_SUSY3.e3998_s2608_s2183_r7725_r7676_p2949
mc15_13TeV.410026.PowhegPythiaEvtGen_P2012_SingleTopSchan_noAllHad_antitop.merge.DAOD_SUSY3.e3998_s2608_s2183_r7725_r7676_p2949

$t\bar{t}$ samples:

mc15_13TeV.407009.PowhegPythiaEvtGen_P2012CT10_ttbarHT6c_1k_hdamp172p5_nonAH.merge.DAOD_SUSY3.e4023_s2608_r7725_r7676_p2949
mc15_13TeV.407010.PowhegPythiaEvtGen_P2012CT10_ttbarHT1k_1k5_hdamp172p5_nonAH.merge.DAOD_SUSY3.e4023_s2608_r7725_r7676_p2949
mc15_13TeV.407010.PowhegPythiaEvtGen_P2012CT10_ttbarHT1k_1k5_hdamp172p5_nonAH.merge.DAOD_SUSY3.e4023_s2726_r7725_r7676_p2949
mc15_13TeV.407011.PowhegPythiaEvtGen_P2012CT10_ttbarHT1k5_hdamp172p5_nonAH.merge.DAOD_SUSY3.e4023_s2608_r7725_r7676_p2949
mc15_13TeV.407011.PowhegPythiaEvtGen_P2012CT10_ttbarHT1k5_hdamp172p5_nonAH.merge.DAOD_SUSY3.e4023_s2726_r7725_r7676_p2949
mc15_13TeV.407012.PowhegPythiaEvtGen_P2012CT10_ttbarMET200_hdamp172p5_nonAH.merge.DAOD_SUSY3.e4023_s2608_r7725_r7676_p2949
mc15_13TeV.407322.PowhegPythiaEvtGen_P2012CT10_ttbarMET300_hdamp172p5_nonAH.merge.DAOD_SUSY3.e5680_s2726_r7772_r7676_p2949
mc15_13TeV.407323.PowhegPythiaEvtGen_P2012CT10_ttbarMET400_hdamp172p5_nonAH.merge.DAOD_SUSY3.e5680_s2726_r7772_r7676_p2949
mc15_13TeV.410000.PowhegPythiaEvtGen_P2012_ttbar_hdamp172p5_nonallhad.merge.DAOD_SUSY3.e3698_s2608_s2183_r7725_r7676_p2949
mc15_13TeV.410007.PowhegPythiaEvtGen_P2012_ttbar_hdamp172p5_allhad.merge.DAOD_SUSY3.e4135_s2608_s2183_r7725_r7676_p2949

$t\bar{t} + H$ samples:

mc15_13TeV.341177.aMcAtNloHerwigppEvtGen_UEEE5_CTEQ6L1_CT10ME_ttH125_dil.merge.DAOD_SUSY3.e4277_s2608_s2183_r7772_r7676_p2949
mc15_13TeV.341270.aMcAtNloHerwigppEvtGen_UEEE5_CTEQ6L1_CT10ME_ttH125_semilep.merge.DAOD_SUSY3.e4277_s2608_s2183_r7772_r7676_p2949
mc15_13TeV.341271.aMcAtNloHerwigppEvtGen_UEEE5_CTEQ6L1_CT10ME_ttH125_allhad.merge.DAOD_SUSY3.e4277_s2608_s2183_r7772_r7676_p2949

$t\bar{t} + V$ samples:

mc15_13TeV.410066.MadGraphPythia8EvtGen_A14NNPDF23LO_ttW_Np0.merge.DAOD_SUSY3.e4111_s2608_s2183_r7725_r7676_p2949
mc15_13TeV.410067.MadGraphPythia8EvtGen_A14NNPDF23LO_ttW_Np1.merge.DAOD_SUSY3.e4111_s2608_s2183_r7725_r7676_p2949
mc15_13TeV.410068.MadGraphPythia8EvtGen_A14NNPDF23LO_ttW_Np2.merge.DAOD_SUSY3.e4111_s2608_s2183_r7725_r7676_p2949
mc15_13TeV.410073.MadGraphPythia8EvtGen_A14NNPDF23LO_ttZnnqq_Np0.merge.DAOD_SUSY3.e4631_s2726_r7725_r7676_p2949
mc15_13TeV.410074.MadGraphPythia8EvtGen_A14NNPDF23LO_ttZnnqq_Np1.merge.DAOD_SUSY3.e4631_s2726_r7725_r7676_p2949
mc15_13TeV.410075.MadGraphPythia8EvtGen_A14NNPDF23LO_ttZnnqq_Np2.merge.DAOD_SUSY3.e4631_s2726_r7725_r7676_p2949
mc15_13TeV.410081.MadGraphPythia8EvtGen_A14NNPDF23_ttbarWW.merge.DAOD_SUSY3.e4111_s2608_s2183_r7725_r7676_p2949
mc15_13TeV.410111.MadGraphPythia8EvtGen_A14NNPDF23LO_ttee_Np0.merge.DAOD_SUSY3.e4632_s2726_r7725_r7676_p2949
mc15_13TeV.410112.MadGraphPythia8EvtGen_A14NNPDF23LO_ttee_Np1.merge.DAOD_SUSY3.e4632_s2726_r7725_r7676_p2949
mc15_13TeV.410113.MadGraphPythia8EvtGen_A14NNPDF23LO_ttmumu_Np0.merge.DAOD_SUSY3.e4632_s2726_r7725_r7676_p2949
mc15_13TeV.410114.MadGraphPythia8EvtGen_A14NNPDF23LO_ttmumu_Np1.merge.DAOD_SUSY3.e4632_s2726_r7725_r7676_p2949
mc15_13TeV.410115.MadGraphPythia8EvtGen_A14NNPDF23LO_tttautau_Np0.merge.DAOD_SUSY3.e4632_s2726_r7725_r7676_p2949

mc15_13TeV.410116.MadGraphPythia8EvtGen_A14NNPDF23LO_tttautau_Np1.merge.DAOD_SUSY3.e4632_s2726_r7725_r7676_p2949

$W+$ jets samples:

mc15_13TeV.364156.Sherpa_221_NNPDF30NNLO_Wmunu_MAXHTPTV0_70_CVetoBVeto.merge.DAOD_SUSY3.e5340_s2726_r7772_r7676_p2949
mc15_13TeV.364157.Sherpa_221_NNPDF30NNLO_Wmunu_MAXHTPTV0_70_CFilterBVeto.merge.DAOD_SUSY3.e5340_s2726_r7772_r7676_p2949
mc15_13TeV.364158.Sherpa_221_NNPDF30NNLO_Wmunu_MAXHTPTV0_70_BFilter.merge.DAOD_SUSY3.e5340_s2726_r7772_r7676_p2949
mc15_13TeV.364159.Sherpa_221_NNPDF30NNLO_Wmunu_MAXHTPTV70_140_CVetoBVeto.merge.DAOD_SUSY3.e5340_s2726_r7772_r7676_p2949
mc15_13TeV.364160.Sherpa_221_NNPDF30NNLO_Wmunu_MAXHTPTV70_140_CFilterBVeto.merge.DAOD_SUSY3.e5340_s2726_r7772_r7676_p2949
mc15_13TeV.364161.Sherpa_221_NNPDF30NNLO_Wmunu_MAXHTPTV70_140_BFilter.merge.DAOD_SUSY3.e5340_s2726_r7772_r7676_p2949
mc15_13TeV.364162.Sherpa_221_NNPDF30NNLO_Wmunu_MAXHTPTV140_280_CVetoBVeto.merge.DAOD_SUSY3.e5340_s2726_r7772_r7676_p2949
mc15_13TeV.364163.Sherpa_221_NNPDF30NNLO_Wmunu_MAXHTPTV140_280_CFilterBVeto.merge.DAOD_SUSY3.e5340_s2726_r7772_r7676_p2949
mc15_13TeV.364164.Sherpa_221_NNPDF30NNLO_Wmunu_MAXHTPTV140_280_BFilter.merge.DAOD_SUSY3.e5340_s2726_r7772_r7676_p2949
mc15_13TeV.364165.Sherpa_221_NNPDF30NNLO_Wmunu_MAXHTPTV280_500_CVetoBVeto.merge.DAOD_SUSY3.e5340_s2726_r7772_r7676_p2949
mc15_13TeV.364166.Sherpa_221_NNPDF30NNLO_Wmunu_MAXHTPTV280_500_CFilterBVeto.merge.DAOD_SUSY3.e5340_s2726_r7772_r7676_p2949
mc15_13TeV.364167.Sherpa_221_NNPDF30NNLO_Wmunu_MAXHTPTV280_500_BFilter.merge.DAOD_SUSY3.e5340_s2726_r7772_r7676_p2949
mc15_13TeV.364168.Sherpa_221_NNPDF30NNLO_Wmunu_MAXHTPTV500_1000.merge.DAOD_SUSY3.e5340_s2726_r7772_r7676_p2949
mc15_13TeV.364169.Sherpa_221_NNPDF30NNLO_Wmunu_MAXHTPTV1000_E_CMS.merge.DAOD_SUSY3.e5340_s2726_r7772_r7676_p2949
mc15_13TeV.364170.Sherpa_221_NNPDF30NNLO_Wenu_MAXHTPTV0_70_CVetoBVeto.merge.DAOD_SUSY3.e5340_s2726_r7772_r7676_p2949
mc15_13TeV.364171.Sherpa_221_NNPDF30NNLO_Wenu_MAXHTPTV0_70_CFilterBVeto.merge.DAOD_SUSY3.e5340_s2726_r7772_r7676_p2949
mc15_13TeV.364172.Sherpa_221_NNPDF30NNLO_Wenu_MAXHTPTV0_70_BFilter.merge.DAOD_SUSY3.e5340_s2726_r7772_r7676_p2949
mc15_13TeV.364173.Sherpa_221_NNPDF30NNLO_Wenu_MAXHTPTV70_140_CVetoBVeto.merge.DAOD_SUSY3.e5340_s2726_r7772_r7676_p2949
mc15_13TeV.364174.Sherpa_221_NNPDF30NNLO_Wenu_MAXHTPTV70_140_CFilterBVeto.merge.DAOD_SUSY3.e5340_s2726_r7772_r7676_p2949
mc15_13TeV.364175.Sherpa_221_NNPDF30NNLO_Wenu_MAXHTPTV70_140_BFilter.merge.DAOD_SUSY3.e5340_s2726_r7772_r7676_p2949
mc15_13TeV.364176.Sherpa_221_NNPDF30NNLO_Wenu_MAXHTPTV140_280_CVetoBVeto.merge.DAOD_SUSY3.e5340_s2726_r7772_r7676_p2949
mc15_13TeV.364177.Sherpa_221_NNPDF30NNLO_Wenu_MAXHTPTV140_280_CFilterBVeto.merge.DAOD_SUSY3.e5340_s2726_r7772_r7676_p2949
mc15_13TeV.364178.Sherpa_221_NNPDF30NNLO_Wenu_MAXHTPTV140_280_BFilter.merge.DAOD_SUSY3.e5340_s2726_r7772_r7676_p2949
mc15_13TeV.364179.Sherpa_221_NNPDF30NNLO_Wenu_MAXHTPTV280_500_CVetoBVeto.merge.DAOD_SUSY3.e5340_s2726_r7772_r7676_p2949
mc15_13TeV.364180.Sherpa_221_NNPDF30NNLO_Wenu_MAXHTPTV280_500_CFilterBVeto.merge.DAOD_SUSY3.e5340_s2726_r7772_r7676_p2949
mc15_13TeV.364181.Sherpa_221_NNPDF30NNLO_Wenu_MAXHTPTV280_500_BFilter.merge.DAOD_SUSY3.e5340_s2726_r7772_r7676_p2949
mc15_13TeV.364182.Sherpa_221_NNPDF30NNLO_Wenu_MAXHTPTV500_1000.merge.DAOD_SUSY3.e5340_s2726_r7772_r7676_p2949
mc15_13TeV.364183.Sherpa_221_NNPDF30NNLO_Wenu_MAXHTPTV1000_E_CMS.merge.DAOD_SUSY3.e5340_s2726_r7772_r7676_p2949
mc15_13TeV.364184.Sherpa_221_NNPDF30NNLO_Wtaunu_MAXHTPTV0_70_CVetoBVeto.merge.DAOD_SUSY3.e5340_s2726_r7772_r7676_p2949
mc15_13TeV.364185.Sherpa_221_NNPDF30NNLO_Wtaunu_MAXHTPTV0_70_CFilterBVeto.merge.DAOD_SUSY3.e5340_s2726_r7772_r7676_p2949
mc15_13TeV.364186.Sherpa_221_NNPDF30NNLO_Wtaunu_MAXHTPTV0_70_BFilter.merge.DAOD_SUSY3.e5340_s2726_r7772_r7676_p2949
mc15_13TeV.364187.Sherpa_221_NNPDF30NNLO_Wtaunu_MAXHTPTV70_140_CVetoBVeto.merge.DAOD_SUSY3.e5340_s2726_r7772_r7676_p2949
mc15_13TeV.364188.Sherpa_221_NNPDF30NNLO_Wtaunu_MAXHTPTV70_140_CFilterBVeto.merge.DAOD_SUSY3.e5340_s2726_r7772_r7676_p2949
mc15_13TeV.364189.Sherpa_221_NNPDF30NNLO_Wtaunu_MAXHTPTV70_140_BFilter.merge.DAOD_SUSY3.e5340_s2726_r7772_r7676_p2949
mc15_13TeV.364190.Sherpa_221_NNPDF30NNLO_Wtaunu_MAXHTPTV140_280_CVetoBVeto.merge.DAOD_SUSY3.e5340_s2726_r7772_r7676_p2949
mc15_13TeV.364191.Sherpa_221_NNPDF30NNLO_Wtaunu_MAXHTPTV140_280_CFilterBVeto.merge.DAOD_SUSY3.e5340_s2726_r7772_r7676_p2949
mc15_13TeV.364192.Sherpa_221_NNPDF30NNLO_Wtaunu_MAXHTPTV140_280_BFilter.merge.DAOD_SUSY3.e5340_s2726_r7772_r7676_p2949
mc15_13TeV.364193.Sherpa_221_NNPDF30NNLO_Wtaunu_MAXHTPTV280_500_CVetoBVeto.merge.DAOD_SUSY3.e5340_s2726_r7772_r7676_p2949
mc15_13TeV.364194.Sherpa_221_NNPDF30NNLO_Wtaunu_MAXHTPTV280_500_CFilterBVeto.merge.DAOD_SUSY3.e5340_s2726_r7772_r7676_p2949
mc15_13TeV.364195.Sherpa_221_NNPDF30NNLO_Wtaunu_MAXHTPTV280_500_BFilter.merge.DAOD_SUSY3.e5340_s2726_r7772_r7676_p2949
mc15_13TeV.364196.Sherpa_221_NNPDF30NNLO_Wtaunu_MAXHTPTV500_1000.merge.DAOD_SUSY3.e5340_s2726_r7772_r7676_p2949
mc15_13TeV.364197.Sherpa_221_NNPDF30NNLO_Wtaunu_MAXHTPTV1000_E_CMS.merge.DAOD_SUSY3.e5340_s2726_r7772_r7676_p2949

$Z+$ jets samples:

mc15_13TeV.364100.Sherpa_221_NNPDF30NNLO_Zmumu_MAXHTPTV0_70_CVetoBVeto.merge.DAOD_SUSY3.e5271_s2726_r7772_r7676_p2949
mc15_13TeV.364101.Sherpa_221_NNPDF30NNLO_Zmumu_MAXHTPTV0_70_CFilterBVeto.merge.DAOD_SUSY3.e5271_s2726_r7772_r7676_p2949
mc15_13TeV.364102.Sherpa_221_NNPDF30NNLO_Zmumu_MAXHTPTV0_70_BFilter.merge.DAOD_SUSY3.e5271_s2726_r7772_r7676_p2949
mc15_13TeV.364103.Sherpa_221_NNPDF30NNLO_Zmumu_MAXHTPTV70_140_CVetoBVeto.merge.DAOD_SUSY3.e5271_s2726_r7772_r7676_p2949
mc15_13TeV.364104.Sherpa_221_NNPDF30NNLO_Zmumu_MAXHTPTV70_140_CFilterBVeto.merge.DAOD_SUSY3.e5271_s2726_r7772_r7676_p2949
mc15_13TeV.364105.Sherpa_221_NNPDF30NNLO_Zmumu_MAXHTPTV70_140_BFilter.merge.DAOD_SUSY3.e5271_s2726_r7772_r7676_p2949
mc15_13TeV.364106.Sherpa_221_NNPDF30NNLO_Zmumu_MAXHTPTV140_280_CVetoBVeto.merge.DAOD_SUSY3.e5271_s2726_r7772_r7676_p2949
mc15_13TeV.364107.Sherpa_221_NNPDF30NNLO_Zmumu_MAXHTPTV140_280_CFilterBVeto.merge.DAOD_SUSY3.e5271_s2726_r7772_r7676_p2949
mc15_13TeV.364108.Sherpa_221_NNPDF30NNLO_Zmumu_MAXHTPTV140_280_BFilter.merge.DAOD_SUSY3.e5271_s2726_r7772_r7676_p2949
mc15_13TeV.364109.Sherpa_221_NNPDF30NNLO_Zmumu_MAXHTPTV280_500_CVetoBVeto.merge.DAOD_SUSY3.e5271_s2726_r7772_r7676_p2949
mc15_13TeV.364110.Sherpa_221_NNPDF30NNLO_Zmumu_MAXHTPTV280_500_CFilterBVeto.merge.DAOD_SUSY3.e5271_s2726_r7772_r7676_p2949
mc15_13TeV.364111.Sherpa_221_NNPDF30NNLO_Zmumu_MAXHTPTV280_500_BFilter.merge.DAOD_SUSY3.e5271_s2726_r7772_r7676_p2949
mc15_13TeV.364112.Sherpa_221_NNPDF30NNLO_Zmumu_MAXHTPTV500_1000.merge.DAOD_SUSY3.e5271_s2726_r7772_r7676_p2949
mc15_13TeV.364113.Sherpa_221_NNPDF30NNLO_Zmumu_MAXHTPTV1000_E_CMS.merge.DAOD_SUSY3.e5271_s2726_r7772_r7676_p2949
mc15_13TeV.364114.Sherpa_221_NNPDF30NNLO_Zee_MAXHTPTV0_70_CVetoBVeto.merge.DAOD_SUSY3.e5299_s2726_r7772_r7676_p2949
mc15_13TeV.364115.Sherpa_221_NNPDF30NNLO_Zee_MAXHTPTV0_70_CFilterBVeto.merge.DAOD_SUSY3.e5299_s2726_r7772_r7676_p2949
mc15_13TeV.364116.Sherpa_221_NNPDF30NNLO_Zee_MAXHTPTV0_70_BFilter.merge.DAOD_SUSY3.e5299_s2726_r7772_r7676_p2949
mc15_13TeV.364117.Sherpa_221_NNPDF30NNLO_Zee_MAXHTPTV70_140_CVetoBVeto.merge.DAOD_SUSY3.e5299_s2726_r7772_r7676_p2949
mc15_13TeV.364118.Sherpa_221_NNPDF30NNLO_Zee_MAXHTPTV70_140_CFilterBVeto.merge.DAOD_SUSY3.e5299_s2726_r7772_r7676_p2949
mc15_13TeV.364119.Sherpa_221_NNPDF30NNLO_Zee_MAXHTPTV70_140_BFilter.merge.DAOD_SUSY3.e5299_s2726_r7772_r7676_p2949
mc15_13TeV.364120.Sherpa_221_NNPDF30NNLO_Zee_MAXHTPTV140_280_CVetoBVeto.merge.DAOD_SUSY3.e5299_s2726_r7772_r7676_p2949
mc15_13TeV.364121.Sherpa_221_NNPDF30NNLO_Zee_MAXHTPTV140_280_CFilterBVeto.merge.DAOD_SUSY3.e5299_s2726_r7772_r7676_p2949
mc15_13TeV.364122.Sherpa_221_NNPDF30NNLO_Zee_MAXHTPTV140_280_BFilter.merge.DAOD_SUSY3.e5299_s2726_r7772_r7676_p2949
mc15_13TeV.364123.Sherpa_221_NNPDF30NNLO_Zee_MAXHTPTV280_500_CVetoBVeto.merge.DAOD_SUSY3.e5299_s2726_r7772_r7676_p2949
mc15_13TeV.364124.Sherpa_221_NNPDF30NNLO_Zee_MAXHTPTV280_500_CFilterBVeto.merge.DAOD_SUSY3.e5299_s2726_r7772_r7676_p2949
mc15_13TeV.364125.Sherpa_221_NNPDF30NNLO_Zee_MAXHTPTV280_500_BFilter.merge.DAOD_SUSY3.e5299_s2726_r7772_r7676_p2949
mc15_13TeV.364126.Sherpa_221_NNPDF30NNLO_Zee_MAXHTPTV500_1000.merge.DAOD_SUSY3.e5299_s2726_r7772_r7676_p2949
mc15_13TeV.364127.Sherpa_221_NNPDF30NNLO_Zee_MAXHTPTV1000_E_CMS.merge.DAOD_SUSY3.e5299_s2726_r7772_r7676_p2949
mc15_13TeV.364128.Sherpa_221_NNPDF30NNLO_Ztautau_MAXHTPTV0_70_CVetoBVeto.merge.DAOD_SUSY3.e5307_s2726_r7772_r7676_p2949
mc15_13TeV.364129.Sherpa_221_NNPDF30NNLO_Ztautau_MAXHTPTV0_70_CFilterBVeto.merge.DAOD_SUSY3.e5307_s2726_r7772_r7676_p2949
mc15_13TeV.364130.Sherpa_221_NNPDF30NNLO_Ztautau_MAXHTPTV0_70_BFilter.merge.DAOD_SUSY3.e5307_s2726_r7772_r7676_p2949
mc15_13TeV.364131.Sherpa_221_NNPDF30NNLO_Ztautau_MAXHTPTV70_140_CVetoBVeto.merge.DAOD_SUSY3.e5307_s2726_r7772_r7676_p2949
mc15_13TeV.364132.Sherpa_221_NNPDF30NNLO_Ztautau_MAXHTPTV70_140_CFilterBVeto.merge.DAOD_SUSY3.e5307_s2726_r7772_r7676_p2949
mc15_13TeV.364133.Sherpa_221_NNPDF30NNLO_Ztautau_MAXHTPTV70_140_BFilter.merge.DAOD_SUSY3.e5307_s2726_r7772_r7676_p2949
mc15_13TeV.364134.Sherpa_221_NNPDF30NNLO_Ztautau_MAXHTPTV140_280_CVetoBVeto.merge.DAOD_SUSY3.e5307_s2726_r7772_r7676_p2949
mc15_13TeV.364135.Sherpa_221_NNPDF30NNLO_Ztautau_MAXHTPTV140_280_CFilterBVeto.merge.DAOD_SUSY3.e5307_s2726_r7772_r7676_p2949
mc15_13TeV.364136.Sherpa_221_NNPDF30NNLO_Ztautau_MAXHTPTV140_280_BFilter.merge.DAOD_SUSY3.e5307_s2726_r7772_r7676_p2949

mc15_13TeV.364137.Sherpa_221_NNPDF30NNLO_Ztautau_MAXHTPTV280_500_CVetoBVeto.merge.DAOD_SUSY3.e5307_s2726_r7772_r7676_p2949
mc15_13TeV.364138.Sherpa_221_NNPDF30NNLO_Ztautau_MAXHTPTV280_500_CFilterBVeto.merge.DAOD_SUSY3.e5313_s2726_r7772_r7676_p2949
mc15_13TeV.364139.Sherpa_221_NNPDF30NNLO_Ztautau_MAXHTPTV280_500_BFilter.merge.DAOD_SUSY3.e5313_s2726_r7772_r7676_p2949
mc15_13TeV.364140.Sherpa_221_NNPDF30NNLO_Ztautau_MAXHTPTV500_1000.merge.DAOD_SUSY3.e5307_s2726_r7772_r7676_p2949
mc15_13TeV.364141.Sherpa_221_NNPDF30NNLO_Ztautau_MAXHTPTV1000_E_CMS.merge.DAOD_SUSY3.e5307_s2726_r7772_r7676_p2949
mc15_13TeV.364142.Sherpa_221_NNPDF30NNLO_Znunu_MAXHTPTV0_70_CVetoBVeto.merge.DAOD_SUSY3.e5308_s2726_r7772_r7676_p2949
mc15_13TeV.364143.Sherpa_221_NNPDF30NNLO_Znunu_MAXHTPTV0_70_CFilterBVeto.merge.DAOD_SUSY3.e5308_s2726_r7772_r7676_p2949
mc15_13TeV.364144.Sherpa_221_NNPDF30NNLO_Znunu_MAXHTPTV0_70_BFilter.merge.DAOD_SUSY3.e5308_s2726_r7772_r7676_p2949
mc15_13TeV.364145.Sherpa_221_NNPDF30NNLO_Znunu_MAXHTPTV70_140_CVetoBVeto.merge.DAOD_SUSY3.e5308_s2726_r7772_r7676_p2949
mc15_13TeV.364146.Sherpa_221_NNPDF30NNLO_Znunu_MAXHTPTV70_140_CFilterBVeto.merge.DAOD_SUSY3.e5308_s2726_r7772_r7676_p2949
mc15_13TeV.364147.Sherpa_221_NNPDF30NNLO_Znunu_MAXHTPTV70_140_BFilter.merge.DAOD_SUSY3.e5308_s2726_r7772_r7676_p2949
mc15_13TeV.364148.Sherpa_221_NNPDF30NNLO_Znunu_MAXHTPTV140_280_CVetoBVeto.merge.DAOD_SUSY3.e5308_s2726_r7772_r7676_p2949
mc15_13TeV.364149.Sherpa_221_NNPDF30NNLO_Znunu_MAXHTPTV140_280_CFilterBVeto.merge.DAOD_SUSY3.e5308_s2726_r7772_r7676_p2949
mc15_13TeV.364150.Sherpa_221_NNPDF30NNLO_Znunu_MAXHTPTV140_280_BFilter.merge.DAOD_SUSY3.e5308_s2726_r7772_r7676_p2949
mc15_13TeV.364151.Sherpa_221_NNPDF30NNLO_Znunu_MAXHTPTV280_500_CVetoBVeto.merge.DAOD_SUSY3.e5308_s2726_r7772_r7676_p2949
mc15_13TeV.364152.Sherpa_221_NNPDF30NNLO_Znunu_MAXHTPTV280_500_CFilterBVeto.merge.DAOD_SUSY3.e5308_s2726_r7772_r7676_p2949
mc15_13TeV.364153.Sherpa_221_NNPDF30NNLO_Znunu_MAXHTPTV280_500_BFilter.merge.DAOD_SUSY3.e5308_s2726_r7772_r7676_p2949
mc15_13TeV.364154.Sherpa_221_NNPDF30NNLO_Znunu_MAXHTPTV500_1000.merge.DAOD_SUSY3.e5308_s2726_r7772_r7676_p2949
mc15_13TeV.364155.Sherpa_221_NNPDF30NNLO_Znunu_MAXHTPTV1000_E_CMS.merge.DAOD_SUSY3.e5308_s2726_r7772_r7676_p2949
mc15_13TeV.364198.Sherpa_221_NN30NNLO_Zmm_Mll10_40_MAXHTPTV0_70_BVeto.merge.DAOD_SUSY3.e5421_s2726_r7772_r7676_p2949
mc15_13TeV.364199.Sherpa_221_NN30NNLO_Zmm_Mll10_40_MAXHTPTV0_70_BFilter.merge.DAOD_SUSY3.e5421_s2726_r7772_r7676_p2949
mc15_13TeV.364200.Sherpa_221_NN30NNLO_Zmm_Mll10_40_MAXHTPTV70_280_BVeto.merge.DAOD_SUSY3.e5421_s2726_r7772_r7676_p2949
mc15_13TeV.364201.Sherpa_221_NN30NNLO_Zmm_Mll10_40_MAXHTPTV70_280_BFilter.merge.DAOD_SUSY3.e5421_s2726_r7772_r7676_p2949
mc15_13TeV.364202.Sherpa_221_NN30NNLO_Zmm_Mll10_40_MAXHTPTV280_E_CMS_BVeto.merge.DAOD_SUSY3.e5421_s2726_r7772_r7676_p2949
mc15_13TeV.364203.Sherpa_221_NN30NNLO_Zmm_Mll10_40_MAXHTPTV280_E_CMS_BFilter.merge.DAOD_SUSY3.e5421_s2726_r7772_r7676_p2949
mc15_13TeV.364204.Sherpa_221_NN30NNLO_Zee_Mll10_40_MAXHTPTV0_70_BVeto.merge.DAOD_SUSY3.e5421_s2726_r7772_r7676_p2949
mc15_13TeV.364205.Sherpa_221_NN30NNLO_Zee_Mll10_40_MAXHTPTV0_70_BFilter.merge.DAOD_SUSY3.e5421_s2726_r7772_r7676_p2949
mc15_13TeV.364206.Sherpa_221_NN30NNLO_Zee_Mll10_40_MAXHTPTV70_280_BVeto.merge.DAOD_SUSY3.e5421_s2726_r7772_r7676_p2949
mc15_13TeV.364207.Sherpa_221_NN30NNLO_Zee_Mll10_40_MAXHTPTV70_280_BFilter.merge.DAOD_SUSY3.e5421_s2726_r7772_r7676_p2949
mc15_13TeV.364208.Sherpa_221_NN30NNLO_Zee_Mll10_40_MAXHTPTV280_E_CMS_BVeto.merge.DAOD_SUSY3.e5421_s2726_r7772_r7676_p2949
mc15_13TeV.364209.Sherpa_221_NN30NNLO_Zee_Mll10_40_MAXHTPTV280_E_CMS_BFilter.merge.DAOD_SUSY3.e5421_s2726_r7772_r7676_p2949
mc15_13TeV.364210.Sherpa_221_NN30NNLO_Ztt_Mll10_40_MAXHTPTV0_70_BVeto.merge.DAOD_SUSY3.e5421_s2726_r7772_r7676_p2949
mc15_13TeV.364211.Sherpa_221_NN30NNLO_Ztt_Mll10_40_MAXHTPTV0_70_BFilter.merge.DAOD_SUSY3.e5421_s2726_r7772_r7676_p2949
mc15_13TeV.364212.Sherpa_221_NN30NNLO_Ztt_Mll10_40_MAXHTPTV70_280_BVeto.merge.DAOD_SUSY3.e5421_s2726_r7772_r7676_p2949
mc15_13TeV.364213.Sherpa_221_NN30NNLO_Ztt_Mll10_40_MAXHTPTV70_280_BFilter.merge.DAOD_SUSY3.e5421_s2726_r7772_r7676_p2949
mc15_13TeV.364214.Sherpa_221_NN30NNLO_Ztt_Mll10_40_MAXHTPTV280_E_CMS_BVeto.merge.DAOD_SUSY3.e5421_s2726_r7772_r7676_p2949
mc15_13TeV.364215.Sherpa_221_NN30NNLO_Ztt_Mll10_40_MAXHTPTV280_E_CMS_BFilter.merge.DAOD_SUSY3.e5421_s2726_r7772_r7676_p2949

Signal samples:

mc15_13TeV.387654.MGPy8EG_A14N23LO_TT_stau_500_090.merge.DAOD_SUSY3.e4485_a766_a821_r7676_p2949
mc15_13TeV.387655.MGPy8EG_A14N23LO_TT_stau_500_140.merge.DAOD_SUSY3.e4485_a766_a821_r7676_p2949
mc15_13TeV.387659.MGPy8EG_A14N23LO_TT_stau_500_490.merge.DAOD_SUSY3.e4485_a766_a821_r7676_p2949
mc15_13TeV.387660.MGPy8EG_A14N23LO_TT_stau_550_090.merge.DAOD_SUSY3.e4485_a766_a821_r7676_p2949
mc15_13TeV.387661.MGPy8EG_A14N23LO_TT_stau_550_140.merge.DAOD_SUSY3.e4485_a766_a821_r7676_p2949
mc15_13TeV.387662.MGPy8EG_A14N23LO_TT_stau_550_190.merge.DAOD_SUSY3.e4485_a766_a821_r7676_p2949
mc15_13TeV.387668.MGPy8EG_A14N23LO_TT_stau_550_490.merge.DAOD_SUSY3.e4485_a766_a821_r7676_p2949
mc15_13TeV.387669.MGPy8EG_A14N23LO_TT_stau_550_540.merge.DAOD_SUSY3.e4608_a766_a821_r7676_p2949
mc15_13TeV.387670.MGPy8EG_A14N23LO_TT_stau_600_090.merge.DAOD_SUSY3.e4485_a766_a821_r7676_p2949
mc15_13TeV.387671.MGPy8EG_A14N23LO_TT_stau_600_140.merge.DAOD_SUSY3.e4485_a766_a821_r7676_p2949
mc15_13TeV.387672.MGPy8EG_A14N23LO_TT_stau_600_190.merge.DAOD_SUSY3.e4485_a766_a821_r7676_p2949
mc15_13TeV.387673.MGPy8EG_A14N23LO_TT_stau_600_240.merge.DAOD_SUSY3.e4485_a766_a821_r7676_p2949
mc15_13TeV.387676.MGPy8EG_A14N23LO_TT_stau_600_390.merge.DAOD_SUSY3.e4485_a766_a821_r7676_p2949
mc15_13TeV.387679.MGPy8EG_A14N23LO_TT_stau_600_540.merge.DAOD_SUSY3.e4485_a766_a821_r7676_p2949
mc15_13TeV.387680.MGPy8EG_A14N23LO_TT_stau_600_590.merge.DAOD_SUSY3.e4608_a766_a821_r7676_p2949
mc15_13TeV.387681.MGPy8EG_A14N23LO_TT_stau_650_090.merge.DAOD_SUSY3.e4485_a766_a821_r7676_p2949
mc15_13TeV.387682.MGPy8EG_A14N23LO_TT_stau_650_140.merge.DAOD_SUSY3.e4485_a766_a821_r7676_p2949
mc15_13TeV.387683.MGPy8EG_A14N23LO_TT_stau_650_190.merge.DAOD_SUSY3.e4485_a766_a821_r7676_p2949
mc15_13TeV.387684.MGPy8EG_A14N23LO_TT_stau_650_240.merge.DAOD_SUSY3.e4485_a766_a821_r7676_p2949
mc15_13TeV.387685.MGPy8EG_A14N23LO_TT_stau_650_290.merge.DAOD_SUSY3.e4485_a766_a821_r7676_p2949
mc15_13TeV.387686.MGPy8EG_A14N23LO_TT_stau_650_340.merge.DAOD_SUSY3.e4485_a766_a821_r7676_p2949
mc15_13TeV.387687.MGPy8EG_A14N23LO_TT_stau_650_390.merge.DAOD_SUSY3.e4485_a766_a821_r7676_p2949
mc15_13TeV.387688.MGPy8EG_A14N23LO_TT_stau_650_440.merge.DAOD_SUSY3.e4485_a766_a821_r7676_p2949
mc15_13TeV.387689.MGPy8EG_A14N23LO_TT_stau_650_490.merge.DAOD_SUSY3.e4485_a766_a821_r7676_p2949
mc15_13TeV.387690.MGPy8EG_A14N23LO_TT_stau_650_540.merge.DAOD_SUSY3.e4485_a766_a821_r7676_p2949
mc15_13TeV.387691.MGPy8EG_A14N23LO_TT_stau_650_590.merge.DAOD_SUSY3.e4485_a766_a821_r7676_p2949
mc15_13TeV.387692.MGPy8EG_A14N23LO_TT_stau_650_640.merge.DAOD_SUSY3.e4485_a766_a821_r7676_p2949
mc15_13TeV.387693.MGPy8EG_A14N23LO_TT_stau_700_090.merge.DAOD_SUSY3.e4485_a766_a821_r7676_p2949
mc15_13TeV.387694.MGPy8EG_A14N23LO_TT_stau_700_140.merge.DAOD_SUSY3.e4485_a766_a821_r7676_p2949
mc15_13TeV.387695.MGPy8EG_A14N23LO_TT_stau_700_190.merge.DAOD_SUSY3.e4485_a766_a821_r7676_p2949
mc15_13TeV.387695.MGPy8EG_A14N23LO_TT_stau_700_190.merge.DAOD_SUSY3.e4485_s2726_r7772_r7676_p2949
mc15_13TeV.387696.MGPy8EG_A14N23LO_TT_stau_700_240.merge.DAOD_SUSY3.e4485_a766_a821_r7676_p2949
mc15_13TeV.387697.MGPy8EG_A14N23LO_TT_stau_700_290.merge.DAOD_SUSY3.e4485_a766_a821_r7676_p2949
mc15_13TeV.387698.MGPy8EG_A14N23LO_TT_stau_700_340.merge.DAOD_SUSY3.e4485_a766_a821_r7676_p2949
mc15_13TeV.387699.MGPy8EG_A14N23LO_TT_stau_700_390.merge.DAOD_SUSY3.e4485_a766_a821_r7676_p2949
mc15_13TeV.387700.MGPy8EG_A14N23LO_TT_stau_700_440.merge.DAOD_SUSY3.e4485_a766_a821_r7676_p2949
mc15_13TeV.387701.MGPy8EG_A14N23LO_TT_stau_700_490.merge.DAOD_SUSY3.e4485_a766_a821_r7676_p2949
mc15_13TeV.387702.MGPy8EG_A14N23LO_TT_stau_700_540.merge.DAOD_SUSY3.e4485_a766_a821_r7676_p2949
mc15_13TeV.387702.MGPy8EG_A14N23LO_TT_stau_700_540.merge.DAOD_SUSY3.e4485_s2726_r7772_r7676_p2949
mc15_13TeV.387703.MGPy8EG_A14N23LO_TT_stau_700_590.merge.DAOD_SUSY3.e4485_a766_a821_r7676_p2949
mc15_13TeV.387704.MGPy8EG_A14N23LO_TT_stau_700_640.merge.DAOD_SUSY3.e4485_a766_a821_r7676_p2949
mc15_13TeV.387705.MGPy8EG_A14N23LO_TT_stau_700_690.merge.DAOD_SUSY3.e4485_a766_a821_r7676_p2949
mc15_13TeV.387706.MGPy8EG_A14N23LO_TT_stau_750_090.merge.DAOD_SUSY3.e4485_a766_a821_r7676_p2949
mc15_13TeV.387707.MGPy8EG_A14N23LO_TT_stau_750_140.merge.DAOD_SUSY3.e4485_a766_a821_r7676_p2949
mc15_13TeV.387708.MGPy8EG_A14N23LO_TT_stau_750_190.merge.DAOD_SUSY3.e4485_a766_a821_r7676_p2949
mc15_13TeV.387709.MGPy8EG_A14N23LO_TT_stau_750_240.merge.DAOD_SUSY3.e4485_a766_a821_r7676_p2949
mc15_13TeV.387710.MGPy8EG_A14N23LO_TT_stau_750_290.merge.DAOD_SUSY3.e4485_a766_a821_r7676_p2949

mc15_13TeV.387711.MGPy8EG_A14N23LO_TT_stau_750_340.merge.DAOD_SUSY3.e4485_a766_a821_r7676_p2949
mc15_13TeV.387712.MGPy8EG_A14N23LO_TT_stau_750_390.merge.DAOD_SUSY3.e4485_a766_a821_r7676_p2949
mc15_13TeV.387713.MGPy8EG_A14N23LO_TT_stau_750_440.merge.DAOD_SUSY3.e4485_a766_a821_r7676_p2949
mc15_13TeV.387714.MGPy8EG_A14N23LO_TT_stau_750_490.merge.DAOD_SUSY3.e4485_a766_a821_r7676_p2949
mc15_13TeV.387715.MGPy8EG_A14N23LO_TT_stau_750_540.merge.DAOD_SUSY3.e4485_a766_a821_r7676_p2949
mc15_13TeV.387716.MGPy8EG_A14N23LO_TT_stau_750_590.merge.DAOD_SUSY3.e4485_a766_a821_r7676_p2949
mc15_13TeV.387717.MGPy8EG_A14N23LO_TT_stau_750_640.merge.DAOD_SUSY3.e4485_a766_a821_r7676_p2949
mc15_13TeV.387718.MGPy8EG_A14N23LO_TT_stau_750_690.merge.DAOD_SUSY3.e4485_a766_a821_r7676_p2949
mc15_13TeV.387719.MGPy8EG_A14N23LO_TT_stau_750_740.merge.DAOD_SUSY3.e4485_a766_a821_r7676_p2949
mc15_13TeV.387720.MGPy8EG_A14N23LO_TT_stau_800_090.merge.DAOD_SUSY3.e4485_a766_a821_r7676_p2949
mc15_13TeV.387721.MGPy8EG_A14N23LO_TT_stau_800_140.merge.DAOD_SUSY3.e4485_a766_a821_r7676_p2949
mc15_13TeV.387722.MGPy8EG_A14N23LO_TT_stau_800_190.merge.DAOD_SUSY3.e4485_a766_a821_r7676_p2949
mc15_13TeV.387723.MGPy8EG_A14N23LO_TT_stau_800_240.merge.DAOD_SUSY3.e4485_a766_a821_r7676_p2949
mc15_13TeV.387724.MGPy8EG_A14N23LO_TT_stau_800_290.merge.DAOD_SUSY3.e4485_a766_a821_r7676_p2949
mc15_13TeV.387725.MGPy8EG_A14N23LO_TT_stau_800_340.merge.DAOD_SUSY3.e4485_a766_a821_r7676_p2949
mc15_13TeV.387726.MGPy8EG_A14N23LO_TT_stau_800_390.merge.DAOD_SUSY3.e4485_a766_a821_r7676_p2949
mc15_13TeV.387727.MGPy8EG_A14N23LO_TT_stau_800_440.merge.DAOD_SUSY3.e4485_a766_a821_r7676_p2949
mc15_13TeV.387728.MGPy8EG_A14N23LO_TT_stau_800_490.merge.DAOD_SUSY3.e4485_a766_a821_r7676_p2949
mc15_13TeV.387729.MGPy8EG_A14N23LO_TT_stau_800_540.merge.DAOD_SUSY3.e4485_a766_a821_r7676_p2949
mc15_13TeV.387730.MGPy8EG_A14N23LO_TT_stau_800_590.merge.DAOD_SUSY3.e4485_a766_a821_r7676_p2949
mc15_13TeV.387731.MGPy8EG_A14N23LO_TT_stau_800_640.merge.DAOD_SUSY3.e4485_a766_a821_r7676_p2949
mc15_13TeV.387732.MGPy8EG_A14N23LO_TT_stau_800_690.merge.DAOD_SUSY3.e4485_a766_a821_r7676_p2949
mc15_13TeV.387733.MGPy8EG_A14N23LO_TT_stau_800_740.merge.DAOD_SUSY3.e4485_a766_a821_r7676_p2949
mc15_13TeV.387734.MGPy8EG_A14N23LO_TT_stau_800_790.merge.DAOD_SUSY3.e4485_a766_a821_r7676_p2949
mc15_13TeV.387735.MGPy8EG_A14N23LO_TT_stau_850_090.merge.DAOD_SUSY3.e4959_a766_a821_r7676_p2949
mc15_13TeV.387736.MGPy8EG_A14N23LO_TT_stau_850_190.merge.DAOD_SUSY3.e4959_a766_a821_r7676_p2949
mc15_13TeV.387737.MGPy8EG_A14N23LO_TT_stau_850_290.merge.DAOD_SUSY3.e4959_a766_a821_r7676_p2949
mc15_13TeV.387738.MGPy8EG_A14N23LO_TT_stau_850_390.merge.DAOD_SUSY3.e4959_a766_a821_r7676_p2949
mc15_13TeV.387739.MGPy8EG_A14N23LO_TT_stau_850_490.merge.DAOD_SUSY3.e4959_a766_a821_r7676_p2949
mc15_13TeV.387740.MGPy8EG_A14N23LO_TT_stau_850_590.merge.DAOD_SUSY3.e4959_a766_a821_r7676_p2949
mc15_13TeV.387741.MGPy8EG_A14N23LO_TT_stau_850_690.merge.DAOD_SUSY3.e4959_a766_a821_r7676_p2949
mc15_13TeV.387742.MGPy8EG_A14N23LO_TT_stau_850_790.merge.DAOD_SUSY3.e4959_a766_a821_r7676_p2949
mc15_13TeV.387743.MGPy8EG_A14N23LO_TT_stau_850_840.merge.DAOD_SUSY3.e4959_a766_a821_r7676_p2949
mc15_13TeV.387744.MGPy8EG_A14N23LO_TT_stau_900_090.merge.DAOD_SUSY3.e4959_a766_a821_r7676_p2949
mc15_13TeV.387745.MGPy8EG_A14N23LO_TT_stau_900_190.merge.DAOD_SUSY3.e4959_a766_a821_r7676_p2949
mc15_13TeV.387746.MGPy8EG_A14N23LO_TT_stau_900_290.merge.DAOD_SUSY3.e4959_a766_a821_r7676_p2949
mc15_13TeV.387747.MGPy8EG_A14N23LO_TT_stau_900_390.merge.DAOD_SUSY3.e4959_a766_a821_r7676_p2949
mc15_13TeV.387748.MGPy8EG_A14N23LO_TT_stau_900_490.merge.DAOD_SUSY3.e4959_a766_a821_r7676_p2949
mc15_13TeV.387749.MGPy8EG_A14N23LO_TT_stau_900_590.merge.DAOD_SUSY3.e4959_a766_a821_r7676_p2949
mc15_13TeV.388000.MGPy8EG_A14N23LO_TT_stau_900_690.merge.DAOD_SUSY3.e4959_a766_a821_r7676_p2949
mc15_13TeV.388001.MGPy8EG_A14N23LO_TT_stau_900_790.merge.DAOD_SUSY3.e4959_a766_a821_r7676_p2949
mc15_13TeV.388002.MGPy8EG_A14N23LO_TT_stau_900_840.merge.DAOD_SUSY3.e4959_a766_a821_r7676_p2949
mc15_13TeV.388003.MGPy8EG_A14N23LO_TT_stau_900_890.merge.DAOD_SUSY3.e4959_a766_a821_r7676_p2949
mc15_13TeV.388004.MGPy8EG_A14N23LO_TT_stau_950_090.merge.DAOD_SUSY3.e4959_a766_a821_r7676_p2949
mc15_13TeV.388005.MGPy8EG_A14N23LO_TT_stau_950_190.merge.DAOD_SUSY3.e4959_a766_a821_r7676_p2949
mc15_13TeV.388006.MGPy8EG_A14N23LO_TT_stau_950_290.merge.DAOD_SUSY3.e4959_a766_a821_r7676_p2949
mc15_13TeV.388007.MGPy8EG_A14N23LO_TT_stau_950_390.merge.DAOD_SUSY3.e4959_a766_a821_r7676_p2949
mc15_13TeV.388008.MGPy8EG_A14N23LO_TT_stau_950_490.merge.DAOD_SUSY3.e4959_a766_a821_r7676_p2949
mc15_13TeV.388009.MGPy8EG_A14N23LO_TT_stau_950_590.merge.DAOD_SUSY3.e4959_a766_a821_r7676_p2949
mc15_13TeV.388010.MGPy8EG_A14N23LO_TT_stau_950_690.merge.DAOD_SUSY3.e4959_a766_a821_r7676_p2949
mc15_13TeV.388011.MGPy8EG_A14N23LO_TT_stau_950_790.merge.DAOD_SUSY3.e4959_a766_a821_r7676_p2949
mc15_13TeV.388012.MGPy8EG_A14N23LO_TT_stau_950_890.merge.DAOD_SUSY3.e4959_a766_a821_r7676_p2949
mc15_13TeV.388013.MGPy8EG_A14N23LO_TT_stau_950_940.merge.DAOD_SUSY3.e4959_a766_a821_r7676_p2949
mc15_13TeV.388014.MGPy8EG_A14N23LO_TT_stau_1000_090.merge.DAOD_SUSY3.e5260_a766_a821_r7676_p2949
mc15_13TeV.388015.MGPy8EG_A14N23LO_TT_stau_1000_190.merge.DAOD_SUSY3.e5260_a766_a821_r7676_p2949
mc15_13TeV.388016.MGPy8EG_A14N23LO_TT_stau_1000_290.merge.DAOD_SUSY3.e5260_a766_a821_r7676_p2949
mc15_13TeV.388017.MGPy8EG_A14N23LO_TT_stau_1000_390.merge.DAOD_SUSY3.e5260_a766_a821_r7676_p2949
mc15_13TeV.388018.MGPy8EG_A14N23LO_TT_stau_1000_490.merge.DAOD_SUSY3.e5260_a766_a821_r7676_p2949
mc15_13TeV.388019.MGPy8EG_A14N23LO_TT_stau_1000_590.merge.DAOD_SUSY3.e5260_a766_a821_r7676_p2949
mc15_13TeV.388020.MGPy8EG_A14N23LO_TT_stau_1000_690.merge.DAOD_SUSY3.e5260_a766_a821_r7676_p2949
mc15_13TeV.388021.MGPy8EG_A14N23LO_TT_stau_1000_790.merge.DAOD_SUSY3.e5260_a766_a821_r7676_p2949
mc15_13TeV.388022.MGPy8EG_A14N23LO_TT_stau_1000_890.merge.DAOD_SUSY3.e5260_a766_a821_r7676_p2949
mc15_13TeV.388023.MGPy8EG_A14N23LO_TT_stau_1000_990.merge.DAOD_SUSY3.e5260_a766_a821_r7676_p2949
mc15_13TeV.388024.MGPy8EG_A14N23LO_TT_stau_1050_090.merge.DAOD_SUSY3.e5260_a766_a821_r7676_p2949
mc15_13TeV.388025.MGPy8EG_A14N23LO_TT_stau_1050_190.merge.DAOD_SUSY3.e5260_a766_a821_r7676_p2949
mc15_13TeV.388026.MGPy8EG_A14N23LO_TT_stau_1050_290.merge.DAOD_SUSY3.e5260_a766_a821_r7676_p2949
mc15_13TeV.388027.MGPy8EG_A14N23LO_TT_stau_1050_390.merge.DAOD_SUSY3.e5260_a766_a821_r7676_p2949
mc15_13TeV.388028.MGPy8EG_A14N23LO_TT_stau_1050_490.merge.DAOD_SUSY3.e5260_a766_a821_r7676_p2949
mc15_13TeV.388029.MGPy8EG_A14N23LO_TT_stau_1050_590.merge.DAOD_SUSY3.e5260_a766_a821_r7676_p2949
mc15_13TeV.388030.MGPy8EG_A14N23LO_TT_stau_1050_690.merge.DAOD_SUSY3.e5260_a766_a821_r7676_p2949
mc15_13TeV.388031.MGPy8EG_A14N23LO_TT_stau_1050_790.merge.DAOD_SUSY3.e5260_a766_a821_r7676_p2949
mc15_13TeV.388032.MGPy8EG_A14N23LO_TT_stau_1050_890.merge.DAOD_SUSY3.e5260_a766_a821_r7676_p2949
mc15_13TeV.388033.MGPy8EG_A14N23LO_TT_stau_1050_990.merge.DAOD_SUSY3.e5260_a766_a821_r7676_p2949
mc15_13TeV.388034.MGPy8EG_A14N23LO_TT_stau_1050_1040.merge.DAOD_SUSY3.e5260_a766_a821_r7676_p2949
mc15_13TeV.388035.MGPy8EG_A14N23LO_TT_stau_1100_090.merge.DAOD_SUSY3.e5673_a766_a821_r7676_p2949
mc15_13TeV.388037.MGPy8EG_A14N23LO_TT_stau_1100_290.merge.DAOD_SUSY3.e5673_a766_a821_r7676_p2949
mc15_13TeV.388038.MGPy8EG_A14N23LO_TT_stau_1100_390.merge.DAOD_SUSY3.e5673_a766_a821_r7676_p2949
mc15_13TeV.388039.MGPy8EG_A14N23LO_TT_stau_1100_490.merge.DAOD_SUSY3.e5673_a766_a821_r7676_p2949
mc15_13TeV.388040.MGPy8EG_A14N23LO_TT_stau_1100_590.merge.DAOD_SUSY3.e5673_a766_a821_r7676_p2949
mc15_13TeV.388041.MGPy8EG_A14N23LO_TT_stau_1100_690.merge.DAOD_SUSY3.e5673_a766_a821_r7676_p2949
mc15_13TeV.388042.MGPy8EG_A14N23LO_TT_stau_1100_790.merge.DAOD_SUSY3.e5673_a766_a821_r7676_p2949
mc15_13TeV.388043.MGPy8EG_A14N23LO_TT_stau_1100_890.merge.DAOD_SUSY3.e5673_a766_a821_r7676_p2949
mc15_13TeV.388044.MGPy8EG_A14N23LO_TT_stau_1100_990.merge.DAOD_SUSY3.e5673_a766_a821_r7676_p2949
mc15_13TeV.388045.MGPy8EG_A14N23LO_TT_stau_1100_1090.merge.DAOD_SUSY3.e5673_a766_a821_r7676_p2949
mc15_13TeV.388046.MGPy8EG_A14N23LO_TT_stau_1150_090.merge.DAOD_SUSY3.e5673_a766_a821_r7676_p2949
mc15_13TeV.388047.MGPy8EG_A14N23LO_TT_stau_1150_190.merge.DAOD_SUSY3.e5673_a766_a821_r7676_p2949
mc15_13TeV.388048.MGPy8EG_A14N23LO_TT_stau_1150_290.merge.DAOD_SUSY3.e5673_a766_a821_r7676_p2949
mc15_13TeV.388049.MGPy8EG_A14N23LO_TT_stau_1150_390.merge.DAOD_SUSY3.e5673_a766_a821_r7676_p2949
mc15_13TeV.391153.MGPy8EG_A14N23LO_TT_stau_1150_490.merge.DAOD_SUSY3.e5673_a766_a821_r7676_p2949

mc15_13TeV.391154.MGPy8EG_A14N23LO_TT_stau_1150_590.merge.DAOD_SUSY3.e5673_a766_a821_r7676_p2949
mc15_13TeV.391155.MGPy8EG_A14N23LO_TT_stau_1150_690.merge.DAOD_SUSY3.e5719_a766_a821_r7676_p2949
mc15_13TeV.391156.MGPy8EG_A14N23LO_TT_stau_1150_790.merge.DAOD_SUSY3.e5719_a766_a821_r7676_p2949
mc15_13TeV.391157.MGPy8EG_A14N23LO_TT_stau_1150_890.merge.DAOD_SUSY3.e5719_a766_a821_r7676_p2949
mc15_13TeV.391158.MGPy8EG_A14N23LO_TT_stau_1150_990.merge.DAOD_SUSY3.e5719_a766_a821_r7676_p2949
mc15_13TeV.391159.MGPy8EG_A14N23LO_TT_stau_1150_1090.merge.DAOD_SUSY3.e5719_a766_a821_r7676_p2949
mc15_13TeV.391160.MGPy8EG_A14N23LO_TT_stau_1150_1140.merge.DAOD_SUSY3.e5673_a766_a821_r7676_p2949
mc15_13TeV.391161.MGPy8EG_A14N23LO_TT_stau_1200_090.merge.DAOD_SUSY3.e5673_a766_a821_r7676_p2949
mc15_13TeV.391162.MGPy8EG_A14N23LO_TT_stau_1200_190.merge.DAOD_SUSY3.e5673_a766_a821_r7676_p2949
mc15_13TeV.391163.MGPy8EG_A14N23LO_TT_stau_1200_290.merge.DAOD_SUSY3.e5719_a766_a821_r7676_p2949
mc15_13TeV.391164.MGPy8EG_A14N23LO_TT_stau_1200_390.merge.DAOD_SUSY3.e5673_a766_a821_r7676_p2949
mc15_13TeV.391165.MGPy8EG_A14N23LO_TT_stau_1200_490.merge.DAOD_SUSY3.e5673_a766_a821_r7676_p2949
mc15_13TeV.391166.MGPy8EG_A14N23LO_TT_stau_1200_590.merge.DAOD_SUSY3.e5673_a766_a821_r7676_p2949
mc15_13TeV.391167.MGPy8EG_A14N23LO_TT_stau_1200_690.merge.DAOD_SUSY3.e5673_a766_a821_r7676_p2949
mc15_13TeV.391168.MGPy8EG_A14N23LO_TT_stau_1200_790.merge.DAOD_SUSY3.e5719_a766_a821_r7676_p2949
mc15_13TeV.391169.MGPy8EG_A14N23LO_TT_stau_1200_890.merge.DAOD_SUSY3.e5719_a766_a821_r7676_p2949
mc15_13TeV.391170.MGPy8EG_A14N23LO_TT_stau_1200_990.merge.DAOD_SUSY3.e5719_a766_a821_r7676_p2949
mc15_13TeV.391171.MGPy8EG_A14N23LO_TT_stau_1200_1090.merge.DAOD_SUSY3.e5719_a766_a821_r7676_p2949
mc15_13TeV.391172.MGPy8EG_A14N23LO_TT_stau_1200_1190.merge.DAOD_SUSY3.e5719_a766_a821_r7676_p2949
mc15_13TeV.391173.MGPy8EG_A14N23LO_TT_stau_1250_090.merge.DAOD_SUSY3.e5673_a766_a821_r7676_p2949
mc15_13TeV.391174.MGPy8EG_A14N23LO_TT_stau_1250_190.merge.DAOD_SUSY3.e5719_a766_a821_r7676_p2949
mc15_13TeV.391175.MGPy8EG_A14N23LO_TT_stau_1250_290.merge.DAOD_SUSY3.e5673_a766_a821_r7676_p2949
mc15_13TeV.391176.MGPy8EG_A14N23LO_TT_stau_1250_390.merge.DAOD_SUSY3.e5719_a766_a821_r7676_p2949
mc15_13TeV.391177.MGPy8EG_A14N23LO_TT_stau_1250_490.merge.DAOD_SUSY3.e5719_a766_a821_r7676_p2949
mc15_13TeV.391178.MGPy8EG_A14N23LO_TT_stau_1250_590.merge.DAOD_SUSY3.e5719_a766_a821_r7676_p2949
mc15_13TeV.391179.MGPy8EG_A14N23LO_TT_stau_1250_690.merge.DAOD_SUSY3.e5673_a766_a821_r7676_p2949
mc15_13TeV.391180.MGPy8EG_A14N23LO_TT_stau_1250_790.merge.DAOD_SUSY3.e5673_a766_a821_r7676_p2949
mc15_13TeV.391181.MGPy8EG_A14N23LO_TT_stau_1250_890.merge.DAOD_SUSY3.e5719_a766_a821_r7676_p2949
mc15_13TeV.391182.MGPy8EG_A14N23LO_TT_stau_1250_990.merge.DAOD_SUSY3.e5673_a766_a821_r7676_p2949
mc15_13TeV.391183.MGPy8EG_A14N23LO_TT_stau_1250_1090.merge.DAOD_SUSY3.e5719_a766_a821_r7676_p2949
mc15_13TeV.391184.MGPy8EG_A14N23LO_TT_stau_1250_1190.merge.DAOD_SUSY3.e5719_a766_a821_r7676_p2949
mc15_13TeV.391185.MGPy8EG_A14N23LO_TT_stau_1250_1240.merge.DAOD_SUSY3.e5719_a766_a821_r7676_p2949

Unskimmed $t\bar{t}$ samples (for trigger studies)**:**

mc15_13TeV.410000.PowhegPythiaEvtGen_P2012_ttbar_hdamp172p5_nonallhad.merge.DAOD_SUSY3.e3698_s2608_s2183_r7725_r7676_p2952

Unskimmed signal samples (for trigger studies)**:**

mc15_13TeV.387702.MGPy8EG_A14N23LO_TT_stau_700_540.merge.DAOD_SUSY3.e4485_a766_a821_r7676_p2797
mc15_13TeV.387702.MGPy8EG_A14N23LO_TT_stau_700_540.merge.DAOD_SUSY3.e4485_s2726_r7772_r7676_p2797
mc15_13TeV.387722.MGPy8EG_A14N23LO_TT_stau_800_190.merge.DAOD_SUSY3.e4485_a766_a821_r7676_p2797
mc15_13TeV.387695.MGPy8EG_A14N23LO_TT_stau_700_190.merge.DAOD_SUSY3.e4485_a766_a821_r7676_p2797
mc15_13TeV.387695.MGPy8EG_A14N23LO_TT_stau_700_190.merge.DAOD_SUSY3.e4485_s2726_r7772_r7676_p2797
mc15_13TeV.387654.MGPy8EG_A14N23LO_TT_stau_500_090.merge.DAOD_SUSY3.e4485_a766_a821_r7676_p2797
mc15_13TeV.387655.MGPy8EG_A14N23LO_TT_stau_500_140.merge.DAOD_SUSY3.e4485_a766_a821_r7676_p2797
mc15_13TeV.387659.MGPy8EG_A14N23LO_TT_stau_500_490.merge.DAOD_SUSY3.e4485_a766_a821_r7676_p2797
mc15_13TeV.387660.MGPy8EG_A14N23LO_TT_stau_550_090.merge.DAOD_SUSY3.e4485_a766_a821_r7676_p2797
mc15_13TeV.387661.MGPy8EG_A14N23LO_TT_stau_550_140.merge.DAOD_SUSY3.e4485_a766_a821_r7676_p2797
mc15_13TeV.387662.MGPy8EG_A14N23LO_TT_stau_550_190.merge.DAOD_SUSY3.e4485_a766_a821_r7676_p2797
mc15_13TeV.387668.MGPy8EG_A14N23LO_TT_stau_550_490.merge.DAOD_SUSY3.e4485_a766_a821_r7676_p2797
mc15_13TeV.387670.MGPy8EG_A14N23LO_TT_stau_600_090.merge.DAOD_SUSY3.e4485_a766_a821_r7676_p2797
mc15_13TeV.387671.MGPy8EG_A14N23LO_TT_stau_600_140.merge.DAOD_SUSY3.e4485_a766_a821_r7676_p2797
mc15_13TeV.387672.MGPy8EG_A14N23LO_TT_stau_600_190.merge.DAOD_SUSY3.e4485_a766_a821_r7676_p2797
mc15_13TeV.387673.MGPy8EG_A14N23LO_TT_stau_600_240.merge.DAOD_SUSY3.e4485_a766_a821_r7676_p2797
mc15_13TeV.387676.MGPy8EG_A14N23LO_TT_stau_600_390.merge.DAOD_SUSY3.e4485_a766_a821_r7676_p2797
mc15_13TeV.387679.MGPy8EG_A14N23LO_TT_stau_600_540.merge.DAOD_SUSY3.e4485_a766_a821_r7676_p2797
mc15_13TeV.387680.MGPy8EG_A14N23LO_TT_stau_600_590.merge.DAOD_SUSY3.e4485_a766_a821_r7676_p2797
mc15_13TeV.387681.MGPy8EG_A14N23LO_TT_stau_650_090.merge.DAOD_SUSY3.e4485_a766_a821_r7676_p2797
mc15_13TeV.387682.MGPy8EG_A14N23LO_TT_stau_650_140.merge.DAOD_SUSY3.e4485_a766_a821_r7676_p2797
mc15_13TeV.387683.MGPy8EG_A14N23LO_TT_stau_650_190.merge.DAOD_SUSY3.e4485_a766_a821_r7676_p2797
mc15_13TeV.387684.MGPy8EG_A14N23LO_TT_stau_650_240.merge.DAOD_SUSY3.e4485_a766_a821_r7676_p2797
mc15_13TeV.387685.MGPy8EG_A14N23LO_TT_stau_650_290.merge.DAOD_SUSY3.e4485_a766_a821_r7676_p2797
mc15_13TeV.387686.MGPy8EG_A14N23LO_TT_stau_650_340.merge.DAOD_SUSY3.e4485_a766_a821_r7676_p2797
mc15_13TeV.387687.MGPy8EG_A14N23LO_TT_stau_650_390.merge.DAOD_SUSY3.e4485_a766_a821_r7676_p2797
mc15_13TeV.387688.MGPy8EG_A14N23LO_TT_stau_650_440.merge.DAOD_SUSY3.e4485_a766_a821_r7676_p2797
mc15_13TeV.387689.MGPy8EG_A14N23LO_TT_stau_650_490.merge.DAOD_SUSY3.e4485_a766_a821_r7676_p2797
mc15_13TeV.387690.MGPy8EG_A14N23LO_TT_stau_650_540.merge.DAOD_SUSY3.e4485_a766_a821_r7676_p2797
mc15_13TeV.387691.MGPy8EG_A14N23LO_TT_stau_650_590.merge.DAOD_SUSY3.e4485_a766_a821_r7676_p2797
mc15_13TeV.387692.MGPy8EG_A14N23LO_TT_stau_650_640.merge.DAOD_SUSY3.e4485_a766_a821_r7676_p2797
mc15_13TeV.387693.MGPy8EG_A14N23LO_TT_stau_700_090.merge.DAOD_SUSY3.e4485_a766_a821_r7676_p2797
mc15_13TeV.387694.MGPy8EG_A14N23LO_TT_stau_700_140.merge.DAOD_SUSY3.e4485_a766_a821_r7676_p2797
mc15_13TeV.387696.MGPy8EG_A14N23LO_TT_stau_700_240.merge.DAOD_SUSY3.e4485_a766_a821_r7676_p2797
mc15_13TeV.387697.MGPy8EG_A14N23LO_TT_stau_700_290.merge.DAOD_SUSY3.e4485_a766_a821_r7676_p2797
mc15_13TeV.387698.MGPy8EG_A14N23LO_TT_stau_700_340.merge.DAOD_SUSY3.e4485_a766_a821_r7676_p2797
mc15_13TeV.387699.MGPy8EG_A14N23LO_TT_stau_700_390.merge.DAOD_SUSY3.e4485_a766_a821_r7676_p2797
mc15_13TeV.387700.MGPy8EG_A14N23LO_TT_stau_700_440.merge.DAOD_SUSY3.e4485_a766_a821_r7676_p2797
mc15_13TeV.387701.MGPy8EG_A14N23LO_TT_stau_700_490.merge.DAOD_SUSY3.e4485_a766_a821_r7676_p2797
mc15_13TeV.387703.MGPy8EG_A14N23LO_TT_stau_700_590.merge.DAOD_SUSY3.e4485_a766_a821_r7676_p2797
mc15_13TeV.387704.MGPy8EG_A14N23LO_TT_stau_700_640.merge.DAOD_SUSY3.e4485_a766_a821_r7676_p2797
mc15_13TeV.387705.MGPy8EG_A14N23LO_TT_stau_700_690.merge.DAOD_SUSY3.e4485_a766_a821_r7676_p2797
mc15_13TeV.387706.MGPy8EG_A14N23LO_TT_stau_750_090.merge.DAOD_SUSY3.e4485_a766_a821_r7676_p2797
mc15_13TeV.387707.MGPy8EG_A14N23LO_TT_stau_750_140.merge.DAOD_SUSY3.e4485_a766_a821_r7676_p2797
mc15_13TeV.387708.MGPy8EG_A14N23LO_TT_stau_750_190.merge.DAOD_SUSY3.e4485_a766_a821_r7676_p2797
mc15_13TeV.387709.MGPy8EG_A14N23LO_TT_stau_750_240.merge.DAOD_SUSY3.e4485_a766_a821_r7676_p2797
mc15_13TeV.387710.MGPy8EG_A14N23LO_TT_stau_750_290.merge.DAOD_SUSY3.e4485_a766_a821_r7676_p2797

mc15_13TeV.387711.MGPy8EG_A14N23LO_TT_stau_750_340.merge.DAOD_SUSY3.e4485_a766_a821_r7676_p2797
mc15_13TeV.387712.MGPy8EG_A14N23LO_TT_stau_750_390.merge.DAOD_SUSY3.e4485_a766_a821_r7676_p2797
mc15_13TeV.387713.MGPy8EG_A14N23LO_TT_stau_750_440.merge.DAOD_SUSY3.e4485_a766_a821_r7676_p2797
mc15_13TeV.387714.MGPy8EG_A14N23LO_TT_stau_750_490.merge.DAOD_SUSY3.e4485_a766_a821_r7676_p2797
mc15_13TeV.387715.MGPy8EG_A14N23LO_TT_stau_750_540.merge.DAOD_SUSY3.e4485_a766_a821_r7676_p2797
mc15_13TeV.387716.MGPy8EG_A14N23LO_TT_stau_750_590.merge.DAOD_SUSY3.e4485_a766_a821_r7676_p2797
mc15_13TeV.387717.MGPy8EG_A14N23LO_TT_stau_750_640.merge.DAOD_SUSY3.e4485_a766_a821_r7676_p2797
mc15_13TeV.387718.MGPy8EG_A14N23LO_TT_stau_750_690.merge.DAOD_SUSY3.e4485_a766_a821_r7676_p2797
mc15_13TeV.387719.MGPy8EG_A14N23LO_TT_stau_750_740.merge.DAOD_SUSY3.e4485_a766_a821_r7676_p2797
mc15_13TeV.387720.MGPy8EG_A14N23LO_TT_stau_800_090.merge.DAOD_SUSY3.e4485_a766_a821_r7676_p2797
mc15_13TeV.387721.MGPy8EG_A14N23LO_TT_stau_800_140.merge.DAOD_SUSY3.e4485_a766_a821_r7676_p2797
mc15_13TeV.387723.MGPy8EG_A14N23LO_TT_stau_800_240.merge.DAOD_SUSY3.e4485_a766_a821_r7676_p2797
mc15_13TeV.387724.MGPy8EG_A14N23LO_TT_stau_800_290.merge.DAOD_SUSY3.e4485_a766_a821_r7676_p2797
mc15_13TeV.387725.MGPy8EG_A14N23LO_TT_stau_800_340.merge.DAOD_SUSY3.e4485_a766_a821_r7676_p2797
mc15_13TeV.387726.MGPy8EG_A14N23LO_TT_stau_800_390.merge.DAOD_SUSY3.e4485_a766_a821_r7676_p2797
mc15_13TeV.387727.MGPy8EG_A14N23LO_TT_stau_800_440.merge.DAOD_SUSY3.e4485_a766_a821_r7676_p2797
mc15_13TeV.387728.MGPy8EG_A14N23LO_TT_stau_800_490.merge.DAOD_SUSY3.e4485_a766_a821_r7676_p2797
mc15_13TeV.387729.MGPy8EG_A14N23LO_TT_stau_800_540.merge.DAOD_SUSY3.e4485_a766_a821_r7676_p2797
mc15_13TeV.387730.MGPy8EG_A14N23LO_TT_stau_800_590.merge.DAOD_SUSY3.e4485_a766_a821_r7676_p2797
mc15_13TeV.387731.MGPy8EG_A14N23LO_TT_stau_800_640.merge.DAOD_SUSY3.e4485_a766_a821_r7676_p2797
mc15_13TeV.387732.MGPy8EG_A14N23LO_TT_stau_800_690.merge.DAOD_SUSY3.e4485_a766_a821_r7676_p2797
mc15_13TeV.387733.MGPy8EG_A14N23LO_TT_stau_800_740.merge.DAOD_SUSY3.e4485_a766_a821_r7676_p2797
mc15_13TeV.387734.MGPy8EG_A14N23LO_TT_stau_800_790.merge.DAOD_SUSY3.e4485_a766_a821_r7676_p2797

Bibliography

[1] S. P. Martin, "A supersymmetry primer," arXiv:hep-ph/9709356.

[2] **ATLAS** Collaboration, ATLAS, "Observation of a new particle in the search for the standard model higgs boson with the atlas detector at the LHC," arXiv:1207.7214.

[3] F. Zwicky, "Die Rotverschiebung von extragalaktischen Nebeln," *Helv. Phys. Acta* **6** (1933) 110–127. [Gen. Rel. Grav.41,207(2009)].

[4] R. Massey, T. Kitching, and J. Richard, "The dark matter of gravitational lensing," arXiv:1001.1739.

[5] D. Scott, "The standard cosmological model," arXiv:astro-ph/0510731.

[6] Nobelprize.org, The official website of the Nobel Prize, "Popular information," 2013. https://www.nobelprize.org/nobel_prizes/physics/laureates/2004/phypub4highen.jpg. last visited on 2017-04-24.

[7] M. Bustamante, L. Cieri, and J. Ellis, "Beyond the standard model for montaneros," arXiv:0911.4409.

[8] P. Binétruy, *Supersymmetry: theory, experiment and cosmology*. Oxford University Press, New York, USA, 1st ed., 2006.

[9] H. Baer and X. Tata, *Weak Scale Supersymmetry: From Superfields to Scattering Events*. Cambridge University Press, New York, USA, 1st ed., 2006.

[10] J. Conlon, "Introduction to supersymmetry (lecture notes)." https://www-thphys.physics.ox.ac.uk/people/JosephConlon/LectureNotes/SUSYLectures.pdf. last visited on 2017-04-25.

[11] P. van Nieuwenhuizen, "Supergravity," *Physics Reports* **68** no. 4, (1981) 189 – 398. http://www.sciencedirect.com/science/article/pii/0370157381901575.

[12] R. Haag, J. T. Lopuszański, and M. Sohnius, "All possible generators of supersymmetries of the s-matrix," *Nuclear Physics B* **88** no. 2, (1975) 257 – 274. http://www.sciencedirect.com/science/article/pii/0550321375902795.

[13] S. Coleman and J. Mandula, "All possible symmetries of the s matrix," *Phys. Rev.* **159** no. 5, (July, 1967) 1251–1256.

[14] I. J. R. Aitchison, "Supersymmetry and the mssm: An elementary introduction," `arXiv:hep-ph/0505105`.

[15] Nausheen R. Shah, "Minimal Supersymmetric Standard Model (lecture notes)." `http://theory.uchicago.edu/~sethi/Teaching/P487-S2003/MSSMnausheen.pdf`, Jun, 2003. last visited on 2017-04-28.

[16] **Particle Data Group** Collaboration, C. Patrignani *et al.*, "Review of Particle Physics," *Chin. Phys.* **C40** no. 10, (2016) 100001.

[17] **Super-Kamiokande Collaboration** Collaboration, H. Nishino *et al.*, "Search for proton decay via $p \to e^+\pi^0$ and $p \to \mu^+\pi^0$ in a large water cherenkov detector," *Phys. Rev. Lett.* **102** (Apr, 2009) 141801. `https://link.aps.org/doi/10.1103/PhysRevLett.102.141801`.

[18] T. M. Undagoitia, F. von Feilitzsch, M. Goeger-Neff, C. Grieb, K. A. Hochmuth, L. Oberauer, W. Potzel, and M. Wurm, "Search for the proton decay $p \to k$ + antineutrino in the large liquid scintillator low energy neutrino astronomy detector lena," `arXiv:hep-ph/0511230`.

[19] G. Jungman, M. Kamionkowski, and K. Griest, "Supersymmetric dark matter," *Physics Reports* **267** (1996) 195–373.

[20] K. Intriligator and N. Seiberg, "Lectures on supersymmetry breaking," `arXiv:hep-ph/0702069`.

[21] P. Meade, N. Seiberg, and D. Shih, "General gauge mediation," `arXiv:0801.3278`.

[22] K. Krasnov, "Spontaneous symmetry breaking and gravity," `arXiv:1112.5097`.

[23] M. Asano, H. D. Kim, R. Kitano, and Y. Shimizu, "Natural supersymmetry at the lhc," *Journal of High Energy Physics* **2010** no. 12, (2010) 1–17.

[24] The LEP SUSY Working Group and ALEPH, DELPHI, L3, OPAL experiments, "Combined LEP selectron/smuon/stau results, 183-208 GeV." `http://lepsusy.web.cern.ch/lepsusy/www/sleptons_summer04/slep_final.html`, Mar, 2016. last visited on 2017-04-28.

[25] **ATLAS** Collaboration, "Search for top-squark pair production in final states with two tau leptons, jets, and missing transverse momentum in $\sqrt{s} = 13$ TeV pp-collisions with the ATLAS detector," Tech. Rep. ATLAS-CONF-2016-048, CERN, Geneva, Aug, 2016. `https://cds.cern.ch/record/2206130`.

[26] **ATLAS** Collaboration, ATLAS, "Atlas run 1 searches for direct pair production of third-generation squarks at the large hadron collider," arXiv:1506.08616.

[27] **CMS** Collaboration, "Search for top-squark pair production in the single-lepton final state in pp collisions at sqrt(s) = 8 tev," arXiv:1308.1586.

[28] **CMS** Collaboration, "Search for supersymmetry using razor variables in events with b-tagged jets in pp collisions at sqrt(s) = 8 tev," arXiv:1502.00300.

[29] **CMS** Collaboration, "Searches for supersymmetry using the mt2 variable in hadronic events produced in pp collisions at 8 tev," arXiv:1502.04358.

[30] **CMS** Collaboration, "Searches for third-generation squark production in fully hadronic final states in proton-proton collisions at sqrt(s) = 8 tev," arXiv:1503.08037.

[31] **CMS** Collaboration, "Search for direct pair production of scalar top quarks in the single- and dilepton channels in proton-proton collisions at sqrt(s) = 8 tev," arXiv:1602.03169.

[32] L. Evans and P. Bryant, "Lhc machine," *Journal of Instrumentation* **3** no. 08, (2008) S08001. http://stacks.iop.org/1748-0221/3/i=08/a=S08001.

[33] "LHC Guide," Mar, 2017. http://cds.cern.ch/record/2255762/.

[34] "The CERN accelerator complex," Jul, 2016. https://cds.cern.ch/record/2197559.

[35] "ATLAS Public Results: LuminosityPublicResultsRun2 ." https://twiki.cern.ch/twiki/bin/view/AtlasPublic/LuminosityPublicResultsRun2. last visited on 2017-04-07.

[36] **ATLAS** Collaboration, G. Aad *et al.*, "The ATLAS Experiment at the CERN Large Hadron Collider," *JINST* **3** (2008) S08003.

[37] "Computer generated image of the whole ATLAS detector," Mar, 2008. https://cds.cern.ch/record/1095924.

[38] **ATLAS** Collaboration, *ATLAS central solenoid: Technical Design Report*. Technical Design Report ATLAS. CERN, Geneva, 1997. https://cds.cern.ch/record/331067. Electronic version not available.

[39] **ATLAS** Collaboration, J. P. Badiou, J. Beltramelli, J. M. Baze, and J. Belorgey, *ATLAS barrel toroid: Technical Design Report*. Technical Design Report ATLAS. CERN, Geneva, 1997. https://cds.cern.ch/record/331065. Electronic version not available.

[40] **ATLAS** Collaboration, *ATLAS inner detector: Technical Design Report, 1*. Technical Design Report ATLAS. CERN, Geneva, 1997. http://cds.cern.ch/record/331063.

[41] F. Pastore, "ATLAS Run-2 status and performance," Tech. Rep. ATL-GEN-PROC-2015-001, CERN, Geneva, Sep, 2015. https://cds.cern.ch/record/2048973.

[42] S. D'Auria, "The ATLAS semiconductor tracker: operations and performance," Tech. Rep. ATL-INDET-PROC-2012-027, CERN, Geneva, Nov, 2012. https://cds.cern.ch/record/1494558.

[43] A. Vogel, "ATLAS Transition Radiation Tracker (TRT): Straw Tube Gaseous Detectors at High Rates," Tech. Rep. ATL-INDET-PROC-2013-005, CERN, Geneva, Apr, 2013. https://cds.cern.ch/record/1537991.

[44] **ATLAS** Collaboration, *ATLAS liquid-argon calorimeter: Technical Design Report*. Technical Design Report ATLAS. CERN, Geneva, 1996. https://cds.cern.ch/record/331061.

[45] **ATLAS** Collaboration, *ATLAS tile calorimeter: Technical Design Report*. Technical Design Report ATLAS. CERN, Geneva, 1996. https://cds.cern.ch/record/331062.

[46] **ATLAS** Collaboration, *ATLAS muon spectrometer: Technical Design Report*. Technical Design Report ATLAS. CERN, Geneva, 1997. https://cds.cern.ch/record/331068.

[47] **ATLAS** Collaboration, M. Livan, "Monitored drift tubes in ATLAS," Tech. Rep. ATL-M-PN-129, CERN, Geneva, Sep, 1996. https://cds.cern.ch/record/319197.

[48] D. Boscherini, "Performance and operation of the ATLAS Resistive Plate Chamber system in LHC Run-1," Tech. Rep. ATL-MUON-PROC-2014-005. 12, CERN, Geneva, Sep, 2014. https://cds.cern.ch/record/1753173.

[49] S. M. Shaw and ATLAS, "The Run-2 ATLAS Trigger System,". https://cds.cern.ch/record/2127944.

[50] **ATLAS** Collaboration, G. Aad *et al.*, "Search for direct top squark pair production in final states with two tau leptons in pp collisions at $\sqrt{s} = 8$ TeV with the ATLAS detector," *Eur. Phys. J.* **C76** no. 2, (2016) 81, arXiv:1509.04976 [hep-ex].

[51] S. Agostinelli *et al.*, "Geant4a simulation toolkit," *Nuclear Instruments and Methods in Physics Research Section A: Accelerators, Spectrometers, Detectors and Associated Equipment* **506** no. 3, (2003) 250 – 303. http://www.sciencedirect.com/science/article/pii/S0168900203013688.

[52] "ATLAS Internal Documentation: CentralMC15ProductionList." `https://twiki.cern.ch/twiki/bin/view/AtlasProtected/CentralMC15ProductionList`. last visited on 2017-04-18.

[53] J. Alwall, M. Herquet, F. Maltoni, O. Mattelaer, and T. Stelzer, "MadGraph 5: Going Beyond," *JHEP* **06** (2011) 128, `arXiv:1106.0522 [hep-ph]`.

[54] J. Alwall, R. Frederix, S. Frixione, V. Hirschi, F. Maltoni, *et al.*, "The automated computation of tree-level and next-to-leading order differential cross sections, and their matching to parton shower simulations," *JHEP* **07** (2014) 079, `arXiv:1405.0301 [hep-ph]`.

[55] Sjöstrand, Torbjorn and Mrenna, Stephen and Skands, Peter Z., "A Brief Introduction to PYTHIA 8.1," *Comput. Phys. Commun.* **178** (2008) 852, `arXiv:0710.3820 [hep-ph]`.

[56] D. J. Lange, "The EvtGen particle decay simulation package," *Nucl. Instrum. Meth.* **A462** (2001) 152–155.

[57] "Simulation of top quark production for the ATLAS experiment at sqrt(s) = 13 TeV," Tech. Rep. ATL-PHYS-PUB-2016-004, CERN, Geneva, Jan, 2016. `https://cds.cern.ch/record/2120417`.

[58] P. Nason, "A New method for combining NLO QCD with shower Monte Carlo algorithms," *JHEP* **11** (2004) 040, `arXiv:hep-ph/0409146`.

[59] S. Frixione, P. Nason, and C. Oleari, "Matching NLO QCD computations with Parton Shower simulations: the POWHEG method," *JHEP* **11** (2007) 070, `arXiv:0709.2092 [hep-ph]`.

[60] S. Alioli, P. Nason, C. Oleari, and E. Re, "A general framework for implementing NLO calculations in shower Monte Carlo programs: the POWHEG BOX," *JHEP* **06** (2010) 043, `arXiv:1002.2581 [hep-ph]`.

[61] Sjöstrand, Torbjorn and Mrenna, Stephen and Skands, Peter Z., "PYTHIA 6.4 Physics and Manual," *JHEP* **05** (2006) 026, `arXiv:hep-ph/0603175`.

[62] "Monte Carlo Generators for the Production of a W or Z/γ^* Boson in Association with Jets at ATLAS in Run 2," Tech. Rep. ATL-PHYS-PUB-2016-003, CERN, Geneva, Jan, 2016. `https://cds.cern.ch/record/2120133`.

[63] Gleisberg, T. and Höche, Stefan. and Krauss, F. and Schönherr, M. and Schumann, S. and others, "Event generation with SHERPA 1.1," *JHEP* **02** (2009) 007, `arXiv:0811.4622 [hep-ph]`.

[64] Höche, Stefan and Krauss, Frank and Schumann, Steffen and Siegert, Frank, "QCD matrix elements and truncated showers," *JHEP* **05** (2009) 053, arXiv:0903.1219 [hep-ph].

[65] Gleisberg, Tanju and Höche, Stefan, "Comix, a new matrix element generator," *JHEP* **12** (2008) 039, arXiv:0808.3674 [hep-ph].

[66] S. Schumann and F. Krauss, "A Parton shower algorithm based on Catani-Seymour dipole factorisation," *JHEP* **03** (2008) 038, arXiv:0709.1027 [hep-ph].

[67] "Multi-Boson Simulation for 13 TeV ATLAS Analyses," Tech. Rep. ATL-PHYS-PUB-2016-002, CERN, Geneva, Jan, 2016. https://cds.cern.ch/record/2119986.

[68] "Modelling of the $t\bar{t}H$ and $t\bar{t}V$ ($V = W, Z$) processes for $\sqrt{s} = 13$ TeV ATLAS analyses," Tech. Rep. ATL-PHYS-PUB-2016-005, CERN, Geneva, Jan, 2016. https://cds.cern.ch/record/2120826.

[69] S. Frixione and B. R. Webber, "Matching NLO QCD computations and parton shower simulations," *JHEP* **06** (2002) 029, arXiv:hep-ph/0204244.

[70] S. Frixione, P. Nason, and B. R. Webber, "Matching NLO QCD and parton showers in heavy flavour production," *JHEP* **08** (2003) 007, arXiv:hep-ph/0305252.

[71] S. Frixione, F. Stoeckli, P. Torrielli, and B. R. Webber, "NLO QCD corrections in Herwig++ with MC@NLO," *JHEP* **01** (2011) 053, arXiv:1010.0568 [hep-ph].

[72] M. Bahr *et al.*, "Herwig++ Physics and Manual," *Eur. Phys. J. C* **58** (2008) 639, arXiv:0803.0883 [hep-ph].

[73] J. Bellm *et al.*, "Herwig 7.0/Herwig++ 3.0 release note," *Eur. Phys. J. C* **76** no. 4, (2016) 196, arXiv:1512.01178 [hep-ph].

[74] M. Cacciari, G. P. Salam, and G. Soyez, "The anti-k_T jet clustering algorithm," *JHEP* **04** (2008) 063, arXiv:0802.1189 [hep-ph].

[75] **ATLAS** Collaboration, "Jet Calibration and Systematic Uncertainties for Jets Reconstructed in the ATLAS Detector at $\sqrt{s} = 13\,\text{TeV}$," Tech. Rep. ATL-PHYS-PUB-2015-015, CERN, Geneva, Jul, 2015. https://cds.cern.ch/record/2037613.

[76] **ATLAS** Collaboration, "Tagging and suppression of pileup jets with the ATLAS detector," Tech. Rep. ATLAS-CONF-2014-018, CERN, Geneva, May, 2014. https://cds.cern.ch/record/1700870.

[77] "ATLAS Internal Documentation: JVT Calibration." https://twiki.cern.ch/twiki/bin/view/AtlasProtected/JVTCalibration. last visited on 2017-04-11.

[78] **ATLAS** Collaboration, "Optimisation of the ATLAS b-tagging performance for the 2016 LHC Run," Tech. Rep. ATL-PHYS-PUB-2016-012, CERN, Geneva, Jun, 2016. https://cds.cern.ch/record/2160731.

[79] **ATLAS** Collaboration, G. Aad *et al.*, "Performance of b-Jet Identification in the ATLAS Experiment," *JINST* **11** no. 04, (2015) P04008, arXiv:1512.01094 [hep-ex].

[80] **ATLAS** Collaboration, "Expected performance of the ATLAS b-tagging algorithms in Run-2," Tech. Rep. ATL-PHYS-PUB-2015-022, CERN, Geneva, Jul, 2015. https://cds.cern.ch/record/2037697.

[81] **ATLAS** Collaboration, ATLAS, "Reconstruction, Energy Calibration, and Identification of Hadronically Decaying Tau Leptons in the ATLAS Experiment for Run-2 of the LHC," Tech. Rep. ATL-PHYS-PUB-2015-045, CERN, Geneva, Nov, 2015. https://cds.cern.ch/record/2064383.

[82] **ATLAS** Collaboration, "Reconstruction, Energy Calibration, and Identification of Hadronically Decaying Tau Leptons in the ATLAS Experiment for Run-2 of the LHC," Tech. Rep. ATL-COM-PHYS-2015-927, CERN, Geneva, Aug, 2015. https://cds.cern.ch/record/2044557.

[83] **ATLAS** Collaboration, "Using Boosted Decision Trees for Hadronic Tau Identification," Tech. Rep. ATL-PHYS-INT-2011-004, CERN, Geneva, Jan, 2011. https://cds.cern.ch/record/1319380.

[84] **ATLAS** Collaboration, "Reconstruction, Energy Calibration, and Identification of Hadronically Decaying Tau Leptons in the ATLAS Experiment for Run-2 of the LHC," Tech. Rep. ATL-PHYS-PUB-2015-045, CERN, Geneva, Nov, 2015. https://atlas.web.cern.ch/Atlas/GROUPS/PHYSICS/PUBNOTES/ATL-PHYS-PUB-2015-045/.

[85] **ATLAS** Collaboration, "Performance of missing transverse momentum reconstruction for the ATLAS detector in the first proton-proton collisions at at $\sqrt{s} = 13\,\text{TeV}$," Tech. Rep. ATL-PHYS-PUB-2015-027, CERN, Geneva, Jul, 2015. https://cds.cern.ch/record/2037904.

[86] **ATLAS** Collaboration, "Expected performance of missing transverse momentum reconstruction for the ATLAS detector at $\sqrt{s} = 13\,\text{TeV}$," Tech. Rep. ATL-PHYS-PUB-2015-023, CERN, Geneva, Jul, 2015. https://cds.cern.ch/record/2037700.

[87] "ATLAS Internal Documentation: Missing Transverse Momentum Reconstruction in Run II." `https://twiki.cern.ch/twiki/bin/viewauth/AtlasProtected/MissingETReconstruction`. last visited on 2017-04-11.

[88] "ATLAS Internal Documentation: SUSY Object Definitions (Rel 20)." `https://twiki.cern.ch/twiki/bin/viewauth/AtlasProtected/SusyObjectDefinitionsr2013TeV?rev=30`. last visited on 2017-04-11.

[89] **ATLAS** Collaboration, "Recommendations of the Physics Objects and Analysis Harmonisation Study Groups 2014," Tech. Rep. ATL-COM-PHYS-2014-451, CERN, Geneva, May, 2014. `https://cds.cern.ch/record/1700874`.

[90] "ATLAS Internal Documentation: DataPreparationCheckListForPhysicsAnalysis." `https://twiki.cern.ch/twiki/bin/viewauth/Atlas/DataPreparationCheckListForPhysicsAnalysis`. last visited on 2017-04-11.

[91] **ATLAS** Collaboration, "Selection of jets produced in 13TeV proton-proton collisions with the ATLAS detector," Tech. Rep. ATLAS-CONF-2015-029, CERN, Geneva, Jul, 2015. `https://cds.cern.ch/record/2037702`.

[92] **ATLAS** Collaboration, "Selection of jets produced in 13TeV proton-proton collisions with the ATLAS detector," Tech. Rep. ATL-COM-SOFT-2015-119, CERN, Geneva, May, 2015. `https://cds.cern.ch/record/2014726`.

[93] C. Patrignani and P. D. Group, "Review of particle physics," *Chinese Physics C* **40** no. 10, (2016) 100001. `http://stacks.iop.org/1674-1137/40/i=10/a=100001`.

[94] B. Abbott, M. Abolins, B. S. Acharya, and et. al, "A measurement of the w boson mass," `arXiv:hep-ex/9712029`.

[95] C. G. Lester and D. J. Summers, "Measuring masses of semi-invisibly decaying particles pair produced at hadron colliders," `arXiv:hep-ph/9906349`.

[96] A. Barr, C. Lester, and P. Stephens, "m(T2): The Truth behind the glamour," *J. Phys.* **G29** (2003) 2343–2363, `arXiv:hep-ph/0304226`.

[97] C. G. Lester and B. Nachman, "Bisection-based asymmetric mt2 computation: a higher precision calculator than existing symmetric methods," `arXiv:1411.4312`.

[98] "ATLAS Internal Documentation: Lowest un-prescaled triggers per data-taking period." `https://twiki.cern.ch/twiki/bin/viewauth/Atlas/LowestUnprescaled`. last visited on 2017-04-07.

[99] C. Bernius *et al.*, "Combined triggers efficiency studies for Run 2," Tech. Rep. ATL-COM-DAQ-2015-066, CERN, Geneva, May, 2015. https://cds.cern.ch/record/2015236.

[100] M. Steimle, "Measurement of the trigger efficiencies in the atlas detector for searches for supersymmetry in events with tau leptons in the final state." http://www.etp.physik.uni-muenchen.de/publications/theses/download/master_msteimle.pdf, May., 2016. Master Thesis.

[101] "ATLAS Public Results: Public Jet Trigger Plots for Collision Data." https://twiki.cern.ch/twiki/bin/view/AtlasPublic/JetTriggerPublicResults. last visited on 2017-04-07.

[102] R. D. Cousins, J. T. Linnemann, and J. Tucker, "Evaluation of three methods for calculating statistical significance when incorporating a systematic uncertainty into a test of the background-only hypothesis for a poisson process," arXiv:physics/0702156 [hep-ex].

[103] M. Baaka, G. Besjes, D. Cote, A. Koutsman, J. Lorenz, and D. Short, "HistFitter software framework for statistical data analysis," arXiv:1410.1280v1.

[104] A. L. Read, "Presentation of search results: the cl_s technique," *Journal of Physics G: Nuclear and Particle Physics* **28** no. 10, (Sep, 2002) 2693. http://stacks.iop.org/0954-3899/28/i=10/a=313.

Selbständigkeitserklärung

Ich versichere hiermit, die vorliegende Arbeit mit dem Titel

Search for Scalar Top Quarks in Final States with Two Hadronically Decaying Tau Leptons

(Suche nach skalaren Top-Quarks in Endzuständen mit zwei hadronisch zerfallenden Tau-Leptonen)

selbständig verfasst zu haben und keine anderen als die angegebenen Quellen und Hilfsmittel verwendet zu haben.

München, 12. Mai 2017, Ferdinand Krieter